Dynamics of Metal Catalysts Under Reactive Conditions Studied by ESEM

vorgelegt von
Master of Science
Jing Cao
geb. in Shanxi (China)

Von der Fakultät II – Mathematik und Naturwissenschaften
der Technischen Universität Berlin
Zur Erlangung des akademischen Grades
Doktor der Naturwissenschaften
-Dr. rer. nat.-
genehmigte Dissertation

Promotionsausschuss:
Vorsitzender: Prof. Dr. Thorsten Ressler
Gutachter: Prof. Dr. Robert Schlögl
Gutachter: Prof. Dr. Michael Lehmann
Gutachter: Prof. Dr. Ronald Imbihl

Tag der wissenschaftlichen Aussprache: 20. Dezember 2018

Berlin 2019

“It always seems impossible until it’s done.”

(Nelson Mandela)

Acknowledgements

My PhD experience has been extremely rewarding yet challenging at times and the completion of the research as well as the writing of this thesis would not have been possible without the support and guidance of numerous people.

First and foremost, I would like to express my appreciation to my supervisor Prof. Dr. Robert Schlögl, Director of the Department of Inorganic Chemistry at the Fritz-Haber-Institute of Max-Planck-Society, for his support, guidance, inspiration and insightful suggestions throughout my PhD. As a supervisor, his vast scientific knowledge and probing nature encouraged and helped me to overcome numerous difficulties and achieve my goals. He taught me to, “never say impossible till you tried all of your best” - this mantra inspired me in both, science and life. I want to thank him for giving me the opportunity to work at the Max-Planck Institute. It has been a great honour to be his student.

I would also like to express my gratitude to Prof. Dr. Ronald Imbihl at Leibniz University Hannover, Prof. Dr. Michael Lehmann and Prof. Dr. Thorsten Ressler at the Technical University of Berlin for agreeing at short notice to invest their valuable time to review my thesis as well as to Prof. Dr. Thorsten Ressler from the Technical University of Berlin, who generously agreed to chair the examination board for my thesis defence.

Furthermore, I would like to express my gratitude to Dr. Mark Greiner, group leader at Max Planck Institute for Chemical Energy Conversion, for investing so much time and effort into the development of my thesis. It has been a great luck to have met him and worked with him. He taught me about the beauty of scientific pursuit.

I am greatly indebted and thankful to my group leader Dr. Thomas Lunkenbein, who promptly helped me with thesis modification after my former supervisor moved to Zürich. When under time pressure, he not only sacrificed his vacation time, but also worked through sickness to finish thesis corrections. Without his help, it would not have been possible to finish the writing for this thesis on time.

I would like to sincerely thank my former group leader Dr. Marc Willinger for his invaluable support and guidance, inspiration and suggestions in my quest for knowledge. He gave me all the freedom to pursue my research and follow my

interest. Without his able guidance, it would have not been able to visualize the amazing “micro-world”.

I also want to express my gratitude to Prof. Klaus Hermann for his great scientific, mental and linguistic support throughout my thesis writing. His patient and timely strong support helped me in overcoming many difficulties.

I am greatly indebted and thankful to Gisela Weinberg who is the first person who showed me how to use environmental scanning electron microscopy. I also would like to thank Wiebke Frandsen, Adnan Hammun and Danail Ivanov for their tremendous technical support for my experiments.

I deeply appreciate the help from all my colleagues, especially Dr. Christoph Pratsch, Dr. Frank Girgsdies, Dr. Gerado Algara-Siller, Dr Xing Huang for experimental data analysis. I am greatly thankful to Dr. Liudmyla Masliuk and Dr. Milivoj Plodinec, who took care of me like a sister and brother. They are, what you call in Chinese, my “Shi Jie” and “Shi Xiong”.

I also want to express my gratitude for the financial support by the China Scholarship Council (CSC).

Last but not least, I would like to thank my dear family and Shuaishuai Li, Yiting Wu for their unconditional support as well as the fabulous distractions they provided whenever needed.

Abstract

Solid surfaces are extremely important in heterogeneous catalysis. They represent the boundary between lid catalyst and surrounding gaseous or liquid environment, and heavily influence chemisorption, surface diffusion, reaction and desorption processes involved in the catalytic cycle. All of these key steps critically depend on the surface composition, structure and morphology. In many cases, catalyst surfaces are dynamic, whereby the structure and composition of the surface can change with time under reaction conditions. Surface structural dynamics reflect the chemical interactions between reactants and catalysts. When catalysts are exposed to mixtures of oxidizing and reducing agents, counteracting effects of the reactants can result in fluctuations in the catalyst's chemical state. In the present work, simple model reactions involving hydrogen and oxygen were used to study surface morphological dynamics. These phenomena were studied on copper, platinum, and nickel catalysts.

The morphological dynamics were studied using a modified environmental scanning electron microscope (ESEM) by which snapshots of dynamic processes on the surface can be recorded and visualized in near real time, while composition of gas phase is simultaneously monitored using a quadrupole mass spectrometer. Near-ambient pressure X-ray photoemission spectroscopy (NAP-XPS) was utilized to identify the chemical composition of the surface phases formed in the relevant conditions.

In the case of copper, three different surface phases were identified, including metallic copper, oxygen terminated copper and cuprous oxides islands. These phases co-exist on the surface and reversibly transition among the three phases under hydrogen rich conditions (4% oxygen) at 700 °C. While copper has a high oxygen activity and low hydrogen activity, the case of platinum demonstrates such dynamics also exist for a metal that has a low oxygen activity and high hydrogen activity. However, the morphological dynamics observed for platinum are distinctly different. The surface becomes very rough in oxygen rich conditions (85% oxygen) and exhibits highest morphological dynamics at 50% oxygen. No oxide is observed, and the surface dynamics are likely a result of transitions between different surface terminations. Depending on the surface phase present, the interaction with

adsorbates changes and acts as a feedback mechanism to change the morphological dynamics. The morphological dynamics are found to correlate with the catalytic activity, where the maximum in H_2 consumption is correlated to the maximum rate of morphological change. This observation highlights the relevance of morphological dynamics to catalytic processes.

In the case of nickel, the hydrogen and oxygen activities are intermediate to those of copper and platinum. In hydrogen oxidation conditions, the surface exhibits global morphological oscillations at 11% oxygen concentration synchronizing with those of the gas composition, where the surface changes between metallic and oxide states at different temperatures.

As morphological changes reflect phase changes, direct visualization of the surface morphological variations provides insights into chemical dynamics of the surfaces. For instance, these findings provide insight into how dynamic phase co-existence is influenced by the reactants present, how the reactivity of the phases to the respective reactants influences the presence and dynamics of phase transitions, and how the resulting surfaces can influence catalytic activity. Further instrumental developments will enable more complex reactions to be studied in this way to achieve a comprehensive understanding of dynamics in catalysis.

Zusammenfassung

Festkörperoberflächen sind von großer Wichtigkeit für die heterogene Katalyse. Sie stellen die Grenzfläche zwischen dem Katalysatorvolumen und der gasförmigen oder flüssigen Umgebung dar und bestimmen daher in hohem Maße die Chemisorption, Oberflächendiffusion, Reaktions- bzw. Desorptionsprozesse, die am katalytische Zyklus beteiligt sind. Hier spielt insbesondere die Oberflächenzusammensetzung mit ihrer Struktur und Morphologie eine entscheidende Rolle. Katalysatoroberflächen zeigen immer eine Dynamik, bei der sich ihre Zusammensetzung und Struktur unter Reaktionsbedingungen mit der Zeit verändert. Dabei ist die Strukturdynamik durch die chemische Wechselwirkung zwischen den Reaktanten und der Oberfläche bestimmt. Wenn ein Katalysator einer Mischung aus oxidierenden und reduzierenden Substanzen ausgesetzt werden, können gegenläufige Effekte der Reaktanten zu Fluktuationen im chemischen Zustand des Katalysators führen. In der vorliegenden Arbeit wurden einfache Modellreaktionen mit Sauerstoff und Wasserstoff benutzt, um die oberflächenmorphologische Dynamik an Kupfer-, Platin- und Nickelkatalysatoren zu untersuchen.

Die Untersuchung strukturdynamischer Eigenschaften erfolgte mit Hilfe eines modifizierten *In situ*-Scanningelektronenmikroskops (environmental scanning electron microscope, ESEM), das es erlaubt, Schnappschüsse dynamischer Prozesse an der Oberfläche in Realzeit durchzuführen und aufzuzeichnen. Dabei erfolgt die Überwachung der Gaszusammensetzung über dem Katalysator simultan mit Hilfe eines Quadrupolmassenspektrometers. Zusätzlich lässt sich die chemische Zusammensetzung der Katalysatoroberfläche während der Reaktion mit Hilfe von Normaldruck-Röntgenphotoelektronenspektroskopie (near-ambient pressure X-ray photoemission spectroscopy, NAP-XPS) messen.

Die Messungen an Kupferkatalysatoren liefern drei unterschiedliche Oberflächenphasen, metallisches Kupfer, sauerstoffterminiertes Kupfer und Cu_2O-Inseln. Diese Phasen existieren gemeinsam an der Oberfläche und können unter wasserstoffreichen Bedingungen (mit 4% Sauerstoff) bei 700 °C reversibel ineinander übergehen, wobei Kupfer eine hohe Sauerstoff- und niedrige Wasserstoffaktivität zeigt. Dynamisches Verhalten findet man auch bei Platin, das eine niedrige Sauerstoff- und hohe Wasserstoffaktivität aufweist. Allerdings ist die

beobachtete Dynamik in der Morphologie bei Platinkatalysatoren deutlich anders. Unter sauerstoffreichen Bedingungen (85%) rauht sich die Oberfläche stark an und zeigt die höchste Oberflächendynamik bei 50% Sauerstoffkonzentration. Oxidbildung wird nicht beobachtet und die Dynamikmessungen deuten nur auf Übergänge zwischen unterschiedlichen Oberflächenterminierungen hin. Abhängig von der vorliegenden Oberflächenphase ändert sich die Wechselwirkung mit Adsorbaten und liefert einen Rückkopplungsmechanismus, der die morphologische Dynamik beeinflusst. Die Messungen zeigen weiter, dass die Dynamik mit der katalytischen Aktivität korreliert, wobei der größte H_2-Verbrauch mit der größten morphologischen Änderungsrate verbunden ist. Diese Beobachtungen unterstreichen die Wichtigkeit der morphologischen Dynamik für katalytische Prozesse.

Die Messungen an Nickelkatalysatoren zeigen Wasserstoff- und Sauerstoffaktivitäten, die zwischen denen für Kupfer und Platin liegen. Unter Wasserstoffoxidationsbedingungen zeigt die Nickeloberfläche globale morpholigische Oszillationen bei 11% Sauerstoffkonzentration, die mit der Gaszusammensetzung synchronisiert sind, wobei temperaturabhängig Übergänge zwischen metallischem und Oxidzustand erfolgen.

Da morphologische Änderungen mit Phasenänderungen zusammenhängen, liefert eine direkte Sichtbarmachung von oberflächenmorphologischen Änderungen auch Aussagen über die Dynamik an Katalysatoroberflächen. Zum Beispiel können solche Messungen zeigen, wie die dynamische Koexistenz verschiedener Phasen durch Reaktanten beeinflusst wird, wie die Existenz und Dynamik von Phasenübergängen durch die Reaktivität der Phasen bestimmt wird, und wie die entsprechenden Oberflächen die katalytische Aktivität beeinflussen. Weiterführende experimentelle Entwicklungen werden die Untersuchung komplexerer Reaktionen ermöglichen, die schließlich zu einem umfassenden Verständnis der Dynamik in der Katalyse führen können.

Contents

1 Introduction

1.1 Role of metal catalysts and challenges

Catalysts can alter the rates of chemical reactions and control the selectivity towards desired products by changing the energy barriers of reaction pathways. While a catalyst changes reaction rates, it does not change the position of the thermodynamic equilibrium.[1-2] Heterogeneous catalysis encompasses systems in which the catalyst and reactants are in different physical phases. Typically, heterogeneous catalysts are inorganic solids, such as metals, oxides, sulphides, or metal salts, while reactants are in liquid or gas phase. In many industrially relevant catalytic reactions, heterogeneous catalysts based on supported metal and metal oxides are commonly used.[3] The metals used for catalysis are essentially from the group VIII and I-B of the periodic table, including those that are hexagonal close-packed (hcp: Co, Ru, Os, Re), body-centred cubic (bcc: Fe and W) and face-centred cubic (fcc: Cu, Ni, Rh, Ag, Pd, Pt, Au, Ir). In this thesis, fcc metals including Cu, Pt and Ni and relevant oxides will be discussed.

In the catalytic process, reactant molecules from a fluid or gas phase, adsorb to the solid's surface, enhancing the reactant's concentration on the surface and favouring its' reaction. In general, the reaction steps include reactant adsorption, intermediate formation, product formation and desorption from the catalyst.[1] In all of these steps, the catalyst surface is heavily involved, and the catalytic activity greatly depends on the surface composition, structure and morphology under working conditions. Catalyst surface structures are distinctly different from the bulk crystal structure due to the unsaturated coordination, and the resulting formation energies of surface defects and their electronic properties. Therefore, detailed catalyst surface analysis is very important for understanding the function of heterogeneous catalysts.

A key step for understanding how the heterogeneous catalyst surface works is to determine the chemical structure of the 'active site'.[4] These active sites are usually found to be high-energy, metastable configurations – such as step edges,[5] stacking faults,[6] vacancy defects,[7] lattice–strained sites,[8] and surfaces of amorphous materials.[9] In most cases, catalysts are exposed to reducing or oxidizing environments. While a solid's surface can promote reaction between adsorbed

molecules, at the same time, adsorbed molecules can chemically change the catalyst's surface. In fact, the interaction between a mixture of reductants, oxidants and a catalyst surface is a dynamic process rather than a static one. It has been firstly proposed by K. Tamaru, “without studying the dynamic behaviour of catalyst surfaces, including adsorbed species, under the reaction conditions no real nature of catalysis can be elucidated. Catalyst should not be kept in a black-box”.[10] However, understanding the complexity that arises from these dynamic chemical transitions is not trivial.

1.2 Phase transition

The phenomena observed at phase transitions can give the most informative insights into the importance of the meta-stable nature of catalysts. Phase transition refers to a reaction system, in which the parameters, e.g. temperature or pressure, results in the formation of two phases of a material with identical free energies. When catalytic reactions occur in such conditions, a small local perturbation such as a change in chemical potential can induce the surface switch from one phase to the other with minimal energetic cost.[11-16]

In particular, heterogeneous catalysts represent systems far from thermodynamic equilibrium. For some non-equilibrated systems critical kinetic phenomena, instabilities[17-19], oscillations[18-19] and chaos[19] can take place. The driving force of this phenomena is the decrease of the Gibbs-free-energy for the overall chemical reaction. Mathematically, this means that a bifurcation happens at the critical point. If the change in the reaction rate is stepwise at the critical point, the kinetic phase transition belongs to the first-order type; if the change is softer, the transition is continuous, and corresponds to second order phase transition.[20] 1) In brief, first-order phase transitions are characterised by a “discontinuous” change in entropy at a fixed temperature (Figure 1.1A). The change in the entropy corresponds to the latent heat,

$$L = T \Delta S \qquad (1\text{-}1)$$

T is the temperature and ΔS denotes the entropy change at the transition point.[21] During phase transitions, a system either absorbs or release a fixed amount of energy per volume.[22] In the process, the temperature of the system stays constant during the addition of heat and the system is in a ‘mixed-phase regime’ in which

some parts of the systems have already completed the transition but others don't. Thus, two phases can co-exist. For example, if a block of ice is heated at constant rate, its temperature increases steadily till it reaches 0 °C, where the temperature stays with ice and water co-exist till the ice is completely melt. 2) Second order phase transitions involve a "continuous" entropy change (Figure 1.1B), which means there is no referred latent heat (equation (1-1)). One example of a second order phase transition is the paramagnetic to ferromagnetic phase transition. In this thesis, we will mainly discuss the first-order kinetic phase transition connected with bi-stability and resulting in chemical waves.

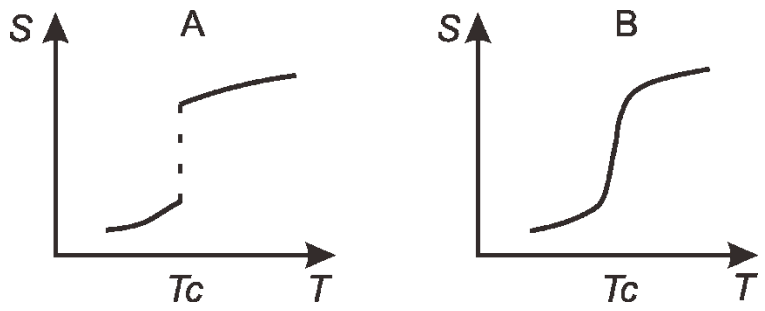

Figure 1.1 A) shows the first order phase transition with dashed line indicating the discontinuous jump at transition temperature Tc; B) is the second order of the phase transition with solid line indicating the continuous entropy at the transition at the transition temperature.

In addition, the interplay of chemical kinetics and diffusion can result in formation of chemical waves, including a transient transition from a metastable state kinetic "phase" to a stable state, or more generally, may cause the homogeneous state of the system to become unstable, which leads to the spontaneous formation of time-dependent or stationary spatial patterns.[23] During such transitions, the reaction can exhibit a stepwise transformation from high to low reaction rate, or vice versa. Repetitive transitions can also occur and result to the formation of spatiotemporal patterns and catalytic oscillatory behaviour of the systems. For instance, the oscillation behaviour on heterogeneous catalysts was first reported in 1970 on Pt for carbon monoxide oxidation.[24-25] Later, Ertl and co-workers observed spatiotemporal patterns formation by application of surface sensitive techniques, i.e. low energy electron diffraction (LEED), Photoemission electron microscope (PEEM), seen Figure 1.2 and details related to the bi-stable phases have been intensively studied.[23, 26-28] Two meta-stable states (CO_{ad} and O_{ad} covered surface) are

coexistent and migrate dynamically on the surface. It also has been found that palladium states oscillate between metal and oxide phases in CO oxidation, which is correlated to the oscillation of products (Figure 1.3).[29]

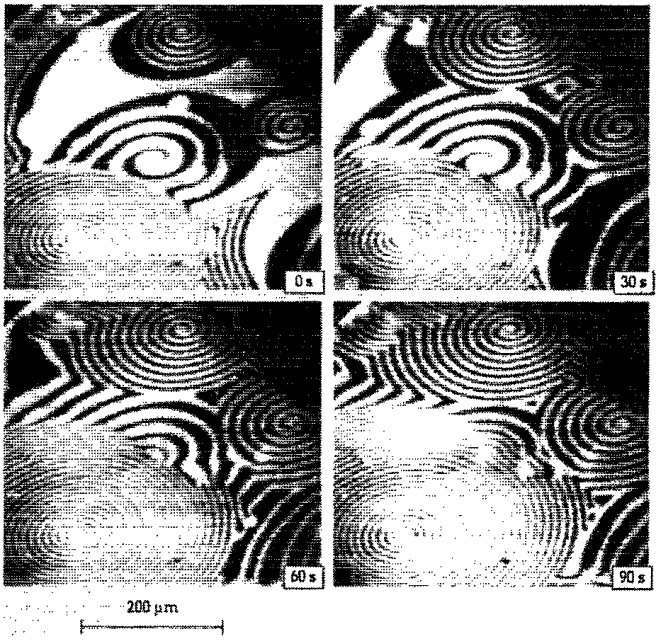

Figure 1.2 PEEM images on Pt(110) shows a temporal evolution of a population of spirals with strongly differing rotation periods and wavelengths in mixture of CO and O_2(T = 448 K, P_{O2} = 4×10^{-4} mbar, P_{CO} = 4.3×10^{-5} mbar).[23]

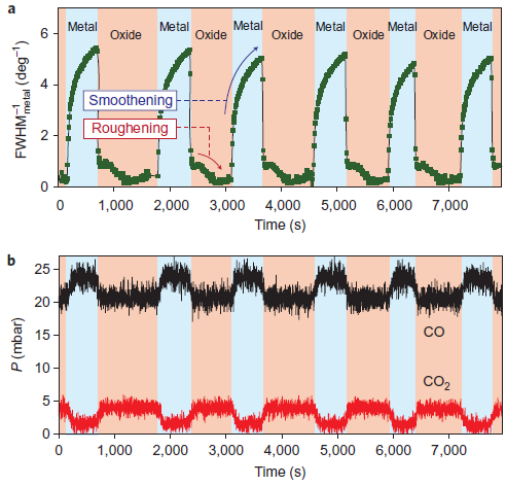

Figure 1.3 Spontaneous oscillations in the CO oxidation rate on Pd(001) as measured by surface X-ray diffraction (SXRD) and mass spectrometry. Measurements were performed at a temperature of 447 K in a constant flow of mixture of CO/O_2/Ar gas with an oxygen pressure of 500 mbar, an argon pressure of 675 mbar and a CO pressure of 25 mbar flowing at 50 ml/min.[29]

1.3 The catalytic surface

The shape and size of a catalytic surface also has a large influence on its properties. Facets with distinctive crystallographic features posse different atomic terminations, and associated surface energies and electronic structures. These properties result in different catalytic activities for different crystal faces.[30] For instance, catalysts exhibiting different facets, such as octahedral tin dioxide nanocrystals with high-index facets of (221),[31] gold nanoparticles with 24 high-index facets[32] and Cu_2O with 50 facets with presence of 24 high-index (311)[30, 33] have been synthesized by facet-controlled synthetic strategies in the attempt to optimize the catalytic activity.

The catalyst's shape and morphology can change dynamically under reaction conditions, in response to the various gases present in the reaction atmosphere. For instance, it has been observed that the shape of Pt nanoparticles' exhibits dynamic and reversible faceting transitions which corresponds to the periodic oscillation of the CO conversion on a bi-stable surface, as reproduced in Figure 1.4. These findings demonstrate that surface structures, chemical compositions and morphologies can change dynamically in a reaction and these changes are related to the catalytic performance.[34] Understanding the relationships between surface dynamics and activity is essential for a rational design of improved catalysts.

As discussed above, catalytically active meta-stable ensembles, in many cases, can be only formed *in situ* due to their high-energy, thermodynamically instability and dependence on kinetics. Their existence generally relies on a delicate interaction with the reactants. Thus, once a reactant is removed for an *ex situ* examination, there is no guarantee that the meta-stable structure remains. However, the scale and complexity of such meta-stable structures make it difficult to identify and characterize them. *In situ* techniques including microscopy and spectroscopy methods, such as *in situ* X-ray diffraction (XRD), X-ray photoelectron spectroscopy (XPS), scanning transmission microscopy (STM), atomic force microscopy (AFM), photoemission electron microscopy (PEEM), have made great progress in recent year to improve our capabilities of characterizing structures that only from due to the interaction with a reactive gas-phase. These methods are now commonly applied to investigate how a catalyst behaves *in situ*, and what kinds of active sites transiently exists on the surface under reaction conditions[35-37].

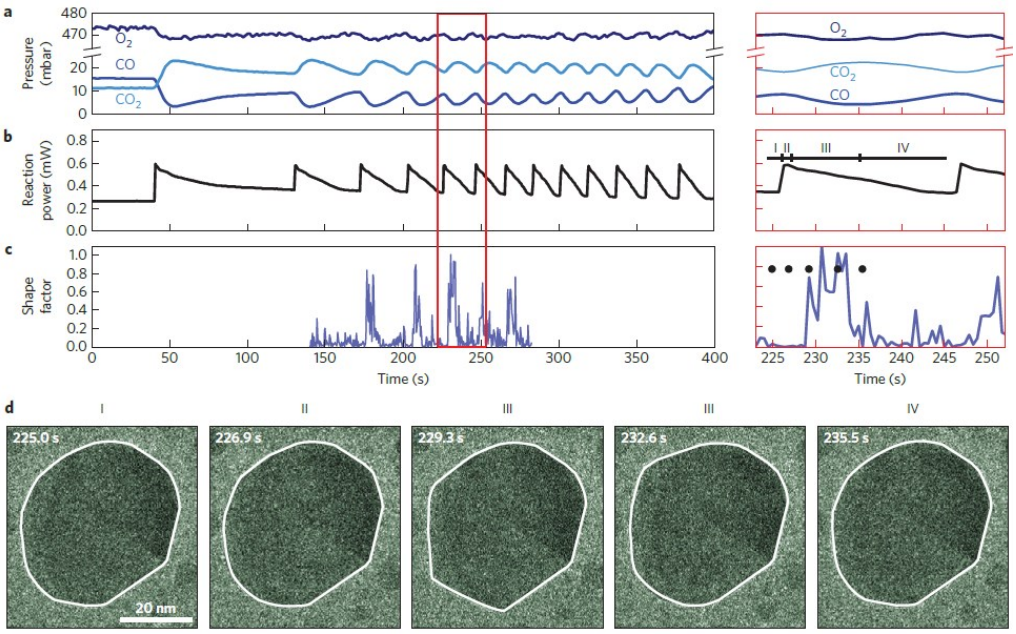

Figure 1.4 Correlation of oscillatory CO oxidation reaction data with the projected morphology of a Pt nanoparticle. The gas entering the reaction zone is 1.0 bar of CO:O_2:He at 3:42:55 and nano-reactor temperature is 659 K. ***a-c****, Mass spectrometry of the CO, O_2 and CO_2 pressure (****a****), reaction power (****b****) and the shape factor (****c****) for the Pt nanoparticle in* ***d*** *as a function of time.* ***d****, Time-resolved TEM images of a Pt nanoparticle at the gas exit of the reaction zone*[34]*.*

1.4 *In situ* technique development

In situ X-ray diffraction is a relatively fast and accurate tool for identifying structures, phases, and sizes of crystals. While continuously changing the incident angle of the X-ray beam, a diffraction pattern is recorded.[38] Since the diffraction pattern is the fingerprint of a crystalline phase, the peak position, intensity, shape and width of the reflection reveals details of the sample's crystal structure.[39] *In situ* XRD measurements allow for continuous monitoring of changes to the crystal structure that are induced by gas adsorption and desorption.[40-41] However, this kind of technique is limited to the crystallographic bulk materials, and thus is not suitable for the investigation of amorphous materials. These measurements also provide only limited morphological information.

Another *in situ* technique that has grown greatly in the last decade is X-ray photoemission spectroscopy (XPS). XPS is a highly surface sensitive technique (few monolayers to nanometers information depth). Analysing the respective characteristic kinetic energies of photoelectrons enables the identification of

elements located at the surface, as well as the elements' oxidation states.[42] In order to partially bridge the pressure gap between catalysis under real working conditions and spectroscopic investigations in ultra-high vacuum (UHV) conditions, a near-ambient-pressure XPS (NAP-XPS) setup has been recently developed.[43-44] The setup allows one to perform the measurements at pressures in the low millibar range by applying a combination of a differential pumping and electrostatic lenses.[45] In some specialized systems, where a micro-focused X-ray source is available, one can even scan the focused X-ray beam across the sample surface to obtain spatially resolved *in situ* XPS.[46]

The developed setups facilitate the characterization of surface structures under reaction conditions. Combined with mass spectrometers and gas chromatographs, the catalyst performance and the chemical state of the surface can be simultaneously investigated.[46] However, most NAP-XPS set-ups yield spectra that reflect the average state of the surface, due to the limited spatial resolution of low incident photo flux lab based X-ray sources. Synchrotron radiation is generally needed to obtain spatially resolved NAP-XPS data. Even with the high flux of synchrotrons, spatially resolved signal intensities are low, requiring long integration times for sufficient signal-to-noise ratios. This long acquisition time limits the ability to thoroughly characterize dynamic phenomena.

In situ microscopy can provide information on the particle size, composition, phase, and morphology variation of materials during chemical reactions with a resolution in the range of tens to hundreds of nanometres. Scanning tunnelling microscope (STM) can probe particles, domain sizes and morphologies with 0.1 nm lateral resolution and 0.01 nm height resolution by scanning a very sharp metal wire tip over a surface. *In situ* STM has been realized via the use of a high pressure STM cell housed within an UHV chamber.[47-51] However, it cannot be used on the insulating materials, limiting its application. *In situ* atomic force microscope (AFM) can be used for both conductive and insulating materials by using a cantilever with a very sharp tip to scan over a sample surface. However, there are several disadvantages: The imaging time of conventional AFM is slow compared to fast catalytic dynamics. This temporal resolution limits the application of the catalyst investigations. Although an improved AFM is able to reduce the imaging time to a second or even less in air as well as fluids, it sacrifices the resolution.[52-54] Furthermore the process of interest must occur

on a fixed substrate, which can either influence or is incompatible with the process of interest.

PEEM is an electron microscopic imaging technique. A surface is illuminated by ultraviolet (UV) radiation. The UV light generates photoelectrons whose intensity greatly depends on the chemical composition and the topography of the surface. This method provides the possibility for surface imaging in the mesoscopic region ranging from several nm to μm. The PEEM image reflects the surface distribution of the work function. PEEM equipped with an imaging energy analyser is capable of measuring the electronic density states as a function of the position of the sample, in real time and space.[28, 55-56] However, using these techniques it is difficult to obtain information on the distribution of elements and the chemical state of the surface.

In situ TEM can be separated to two branches – environmental transmission electron microscopy (ETEM) and systems based on microelectromechanical systems (MEMS). The ETEM can provide atomic resolution as it uses a very low flow of gas along the sample area, which allows to reduce atmosphere-beam interaction. However, it requires that reactions are carried out at extremely low pressures as the gas passes directly through the microscope. MEMS devices allow to carry out the reaction under pressures of up to several bar. This is achieved by placing the catalyst in a small chamber between two beam-transparent windows, which insulate the sample environment from the surrounding vacuum. However, in this case the beam interaction with the window itself, and with the reaction media can limit the resolution. *In situ* TEM requires specific sample preparation and the use of specific microchip windows which provide the heating of the sample. This requirement limits the method to nano-sized particles. *In situ* TEM investigations are conducted using acceleration voltages of several hundred keV. This can lead to significant beam influence on the target sample and the reaction media.

In summary, *in situ* XRD and XPS can provide information on the average catalyst structure and composition, while *in situ* STM, AFM and TEM can provide local atomistic details under reaction conditions. There is in some sense a ‘scale gap’ between the *in situ* methods. Environmental scanning electron microscope (ESEM) helps to bridge this gap by providing information from the nm to μm range. Compared to *in situ* PEEM, it can analyse samples at much higher chemical

potentials. Thus some part of the ‘pressure gap’ is bridged by ESEM. Another important aspect is, due to the lower kinetic energy of the electron beam, the beam influence on the investigated catalyst is less severe than in TEM.

1.5 Environmental scanning electron microscopy

1.5.1 Working principle of the scanning electron microscope

The scanning electron microscope is a type of electron microscope that images the sample surface by a focused beam of electrons in a raster scan pattern. As the electrons interact with the sample, various signals containing secondary electrons (SE), backscattered electrons (BSE), characteristic X-rays, cathode luminescence, absorbed current on the specimen, and transmitted electrons can be formed, as illustrated in Figure 1.5. Secondary electrons are mainly used in the SEM to image the morphology of the sample surface. Some SEM instruments are equipped with backscatter electron and energy dispersive X-ray spectroscopy (EDS) detectors for elemental analysis.[57]

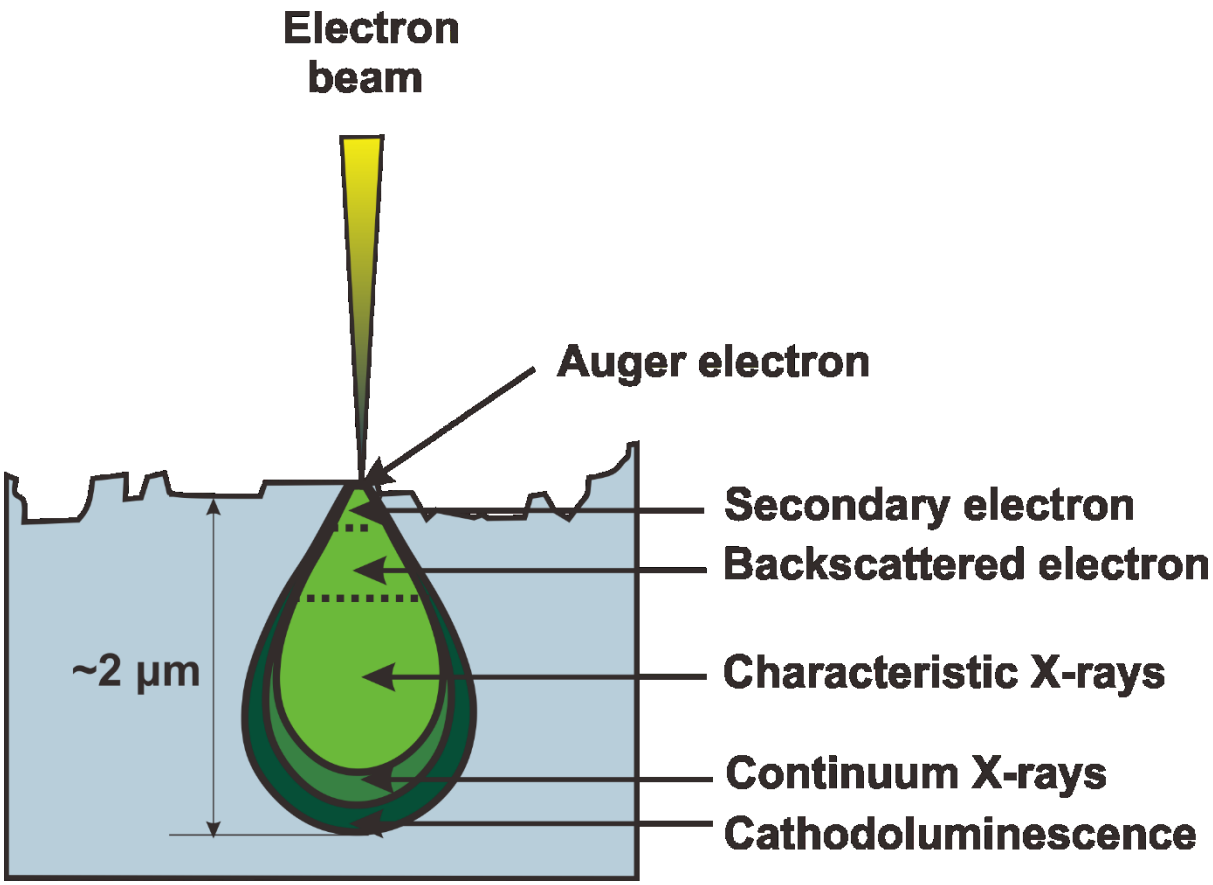

Figure 1.5 The diagram shows a cross section of the various signals resulting from the electron-beam interaction.

The incident electrons cause secondary electrons to be emitted from the sample due to elastic and inelastic scattering events within the sample's surface and material near the surface (Figure 1.6A). Elastic events are broadly associated with nuclear scattering, in which the electrons change their direction without significant energy loss. Inelastic events produce excitations of atomic electrons which results in some energy loss but no change in the direction. High-energy electrons that are ejected by an elastic collision of an incident electron, typically with a sample´s nucleus, are referred to as backscattered electrons (Figure 1.6B). The energy of the backscattered electrons is comparable to that of the incident electrons. Scintillator type or solid-state detectors are used for the collection of backscattered electrons.[58-59] Emitted low-energy electrons which result from inelastic scattering events are called secondary electrons. Secondary electrons can be formed by collision with the core electrons bound to the nuclei of the sample, resulting in the ejection of loosely bound electrons. The energy of secondary electrons is typically lower than 50 eV. Scintillator type detectors (Everhart-Thornley) are used for secondary electron imaging with a detector charged with a positive voltage to attract electrons for improved signal-to-noise ratio. The X-ray signal is a result of the recombination of free electrons and positive electron holes that are generated within the material (Figure 1.6C). The X-ray signal can originate from the bulk part of the specimen surface, and allows for determination of the elemental composition through EDS (energy dispersive X-ray spectroscopy) analysis of characteristic X-ray signals.[60]

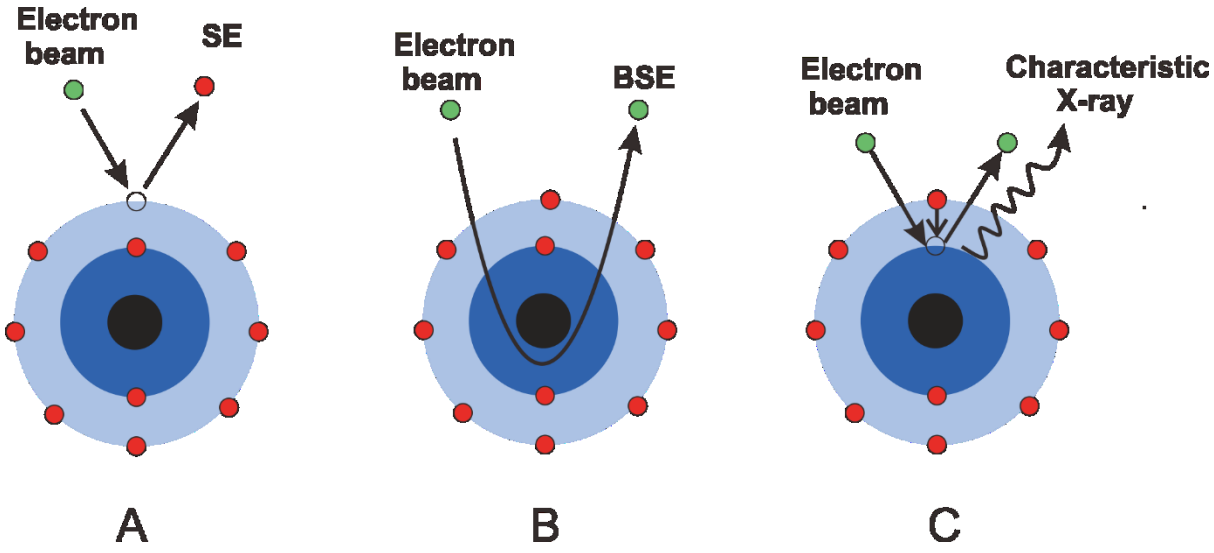

Figure 1.6 Three mechanism of A) emission of secondary electrons, B) backscattered electrons and C) characteristic X-rays.

1.5.2 Conventional scanning electron microscope

As we are already familiar with the SEM working principle, a brief introduction about the conventional scanning electron microscope will be presented. SEM is used to image the sample surface using focused electron beams. From the description, the electron beam is the key part during the whole imaging process. The equipment can be divided into four main sections: electron gun (beam source), lenses (focus beam), vacuum system (reduce scattering of beam), specimen stage (beam interaction with specimen) and detector (collected beam induced secondary electrons, backscattered electrons, X-rays (Figure 1.7).

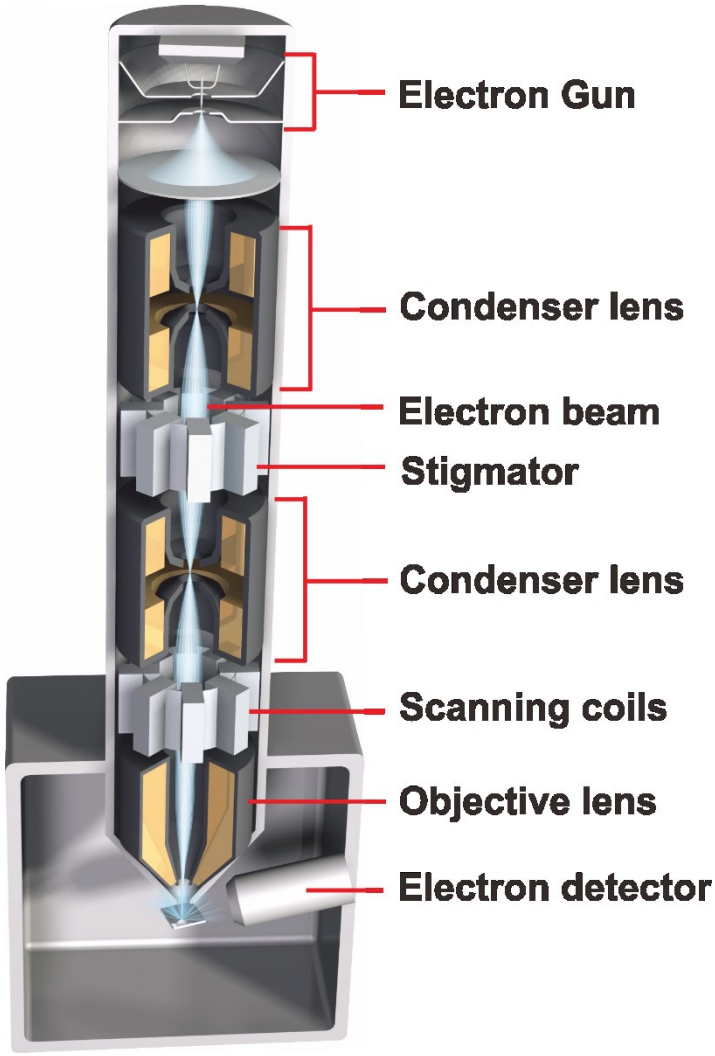

Figure 1.7 A schematic drawing of scanning electron microscope cross section.

Electron gun: The electron gun is located at the top of the column to produce the steady stream of electrons from a filament. Two types of electron guns are typically used: Thermionic guns are the most common types of electron sources. Thermal energy is applied to overcome the work function of a filament. Electrons then can escape from the filament and are accelerated toward the specimen. The materials that are commonly used for the filaments are tungsten and lanthanum hexaboride (LaB_6). Thermionic guns suffer from a relatively low brightness, the evaporation of the cathode materials and high drift during the operation. The other type of electron gun is the Field emission gun (FEG). Here, electrons are extracted from the filament tip by applying an additional strong electrical filed. The FEG usually use a ZrO_2 coated tungsten wire as a sharp tip.

Condenser lenses: The condenser lenses help to converge the electron beam that originated from the gun by electromagnetic forces. Combined with the selected accelerating voltage and emission and brightness of the gun, the condenser lenses determine the intensity of the electron beam on the sample.

Vacuum system: For three reasons a high vacuum system is required for SEM imaging. 1) The hot filament used as the electron beam source would be oxidized at atmospheric pressures or sufficiently high oxygen partial pressures; 2) The electromagnetic condenser lenses need to be operated under a fairly clean, dust-free environments for reliable operation; 3) Air particles and dust can influence the beam by scattering or even blocking the electrons from reaching the specimen. Pressures below 1 Pa are easily reached by turbo-molecular pumps, which exhibit rotation speeds between 20,000 to 50,000 rotations per minute. Thus, pressures ranging from intermediated vacuum (~10^{-2} Pa) to ultra-high vacuum levels (~10^{-8} Pa) can be obtained. In a SEM a different combination of pumps can produce pressure in the column and chamber around 10^{-5} Pa or 10^{-7} Pa at the gun.

Specimen stage: The traditional specimen stage works as a conductive sample holder to support and stabilize the sample during scanning. The specimen should generally have a high electrical conductivity to avoid electron accumulation on the sample surface, which can induce the charging effect.

Detector: Detectors are the ‘eyes’ of a SEM and collect secondary electrons, backscattering electrons and characteristic X-ray signals. Everhart-Thornley detectors are used to collect the secondary electrons emitted from the outer surface of a specimen. They provide detailed images of the specimen surface. Backscattering electron detectors and energy dispersive X-ray spectroscopy (EDX) detectors are mainly used to distinguish different chemical composition.

In summary, traditional SEM can measure the morphology and chemical composition of the outer surface of a conductive specimen at room temperature under high vacuum conditions. It is difficult to study non-conductive specimens due to the effect of charging. It is also not possible to investigate samples under reaction conditions, due the requirement of high vacuum. In order to overcome these limitations, a modified environmental scanning electron microscope (ESEM) was developed.

1.5.3 Commercial environmental scanning electron microscope

The environmental scanning electron microscope (ESEM) is different from the conventional scanning electron microscope in several aspects. The differences include a differential pump system and a gaseous secondary detector.[61]

Differential pump system: Differential pump system allows for imaging wet and insulating specimens in a gaseous atmosphere, while the electron gun itself can still maintain high vacuum pressure around 10^{-7} Pa. This is realized by the use of a 'bullet-shape' device specially designed for ESEM, which is mounted at the pole piece and contains five pressure-limiting apertures (PLA)[62], seen in Figure 1.8A. The apertures are simple discs with small pinholes bored through the centre, 2 pieces of 1.25 mm and 3 pieces of 400μm. The chamber gas that passes through the first aperture (PLA1) is quickly removed from the system by a pump to maintain a very low pressure in a downstream region (Figure 1.8B). Some of the gas escapes further from the first stage pump will be pumped away through PLA2, the same holds for PLA3, PLA4 and PLA5. The achieved pressures follow the order $P_5 << P_4 << P_3 << P_2 << P_1$. By applying this differential pump system, it is able to remain with very good vacuum at the electron gun (~10^{-7} Pa) and relatively low vacuum (i.e. high pressure) in the specimen chamber, around 200 Pa, without endangering the electron gun.

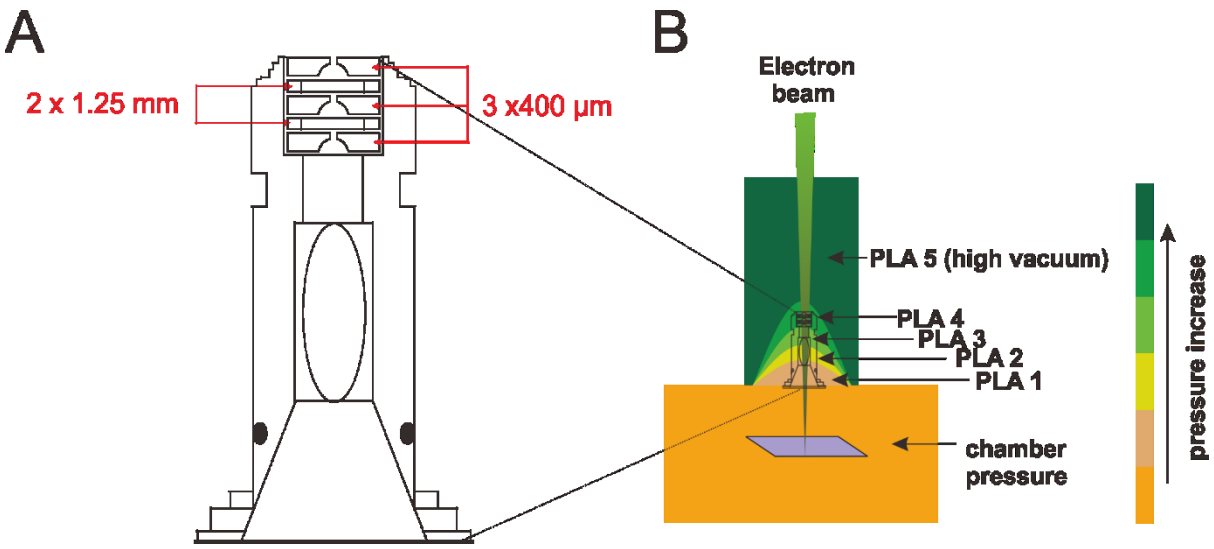

Figure 1.8 A) Schematic diagram of "bullet- shape" device of ESEM (FEI Quanta 200); B) isodensity contours of gas flowing through pressure-limiting aperture (PLA).

Gaseous secondary detector: The Everhart-Thornley detector commonly used in high-vacuum conditions cannot be used in gaseous atmosphere because of

unwanted gas ionization and breakdown caused by the high voltage on the scintillator surface.[61, 63] An alternative detector has been designed based on the well-understood 'ionization behaviour' of low pressure gases. Gas ionization is induced by a moderate electric field, forcing collisions between highly mobile secondary electrons and neutral gas molecules. This results in the formation of an additional daughter electrons. A cascade amplification take place, as illustrated in Figure 1.9. The electrons produced are drawn towards the positively charged detector. These positive gas phase ions generated in this process also effectively neutralize the troublesome surface charging of insulating specimens, regardless of the beam acceleration voltage.[61, 64-66] Two modes (low Vacuum or ESEM) of our instrument (Quanta 200) are available for image recording. A large field detector (LFD) is used in the low vacuum mode, which operates at pressures from 14 Pa to 200 Pa. The gaseous secondary electron detector (GSED) is mainly used for ESEM mode, which can reach gas pressures up to 2600 Pa.

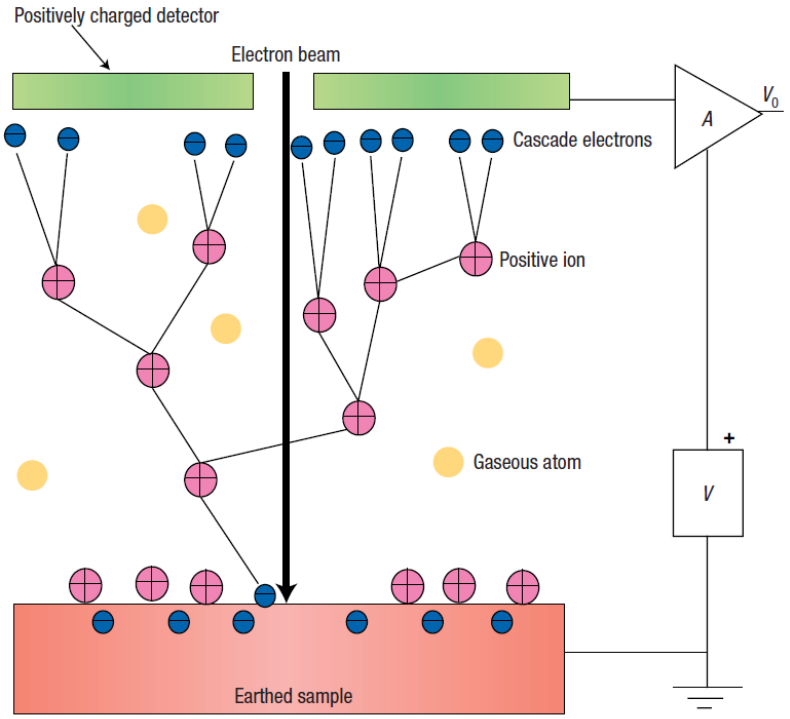

Figure 1.9 Schematic illustration of electron beam/sample/gas interactions in an ESEM chamber. The electrons emitted from the sample ionize the gas molecules. Each ionizing collision gives rise to a daughter electron, which, like the original electron, is accelerated toward the positively charged detector. The positive ions drift back toward the sample surface.[65]

1.5.4 Modified environmental scanning electron microscope

The development from SEM to ESEM was a major step in scientific research. However, due to the temperature (T < room temperature) and unicity of gas (water vapor is mainly used), the application of this method was mainly limited to biological fields. For catalyst investigation under reaction conditions, which require higher temperatures, various gas atmospheres and catalytic activity testing instruments, we modified a commercial ESEM with gas lines and a heating stage, and connected a mass spectrometer (MS) in order to be able to investigate catalyst surface dynamics under reaction conditions, and correlate observations with online catalyst activity data.

Gas line: A gas feeding system, designed for stable and constant gas flow rates, was built. The present gas-feeding system consists of several identical lines, consisting of pressure regulators, mass flow controllers and valves (Figure 1.9). Pressure regulators are used to reduce the input gas pressure from the gas supplies (ca. 200 bar) to the 3 bar needed to operate the mass flow controllers. Mass flow controllers (EL-FLOW Select from Bronkhorst) are used to control the gas flow rate in the ESEM chamber. The MFCs were equipped with a digital pc-board, featuring self-diagnostics, alarm and counter functions, digital communication and remotely adjustable control settings.[67] This ensures a stable and precise gas flow into the ESEM chamber. Imaging in low vacuum mode/ESEM mode is sensitive to the imaging gas. Thus, small gas fluctuations can lead to severe contrast changes on the images. In the experiment, it is often necessary to subsequently change gases in order to reduce or oxidize the materials. The dose of the second, or third gas can induce gas overshoot, which is due to the pressure difference between the residual gas in the gas line and the ESEM. Therefore, three-way valves were built to avoid the gas overshoot by pumping the residual gas through one outlet before introducing it into the chamber through the other outlet (Figure 1.10).

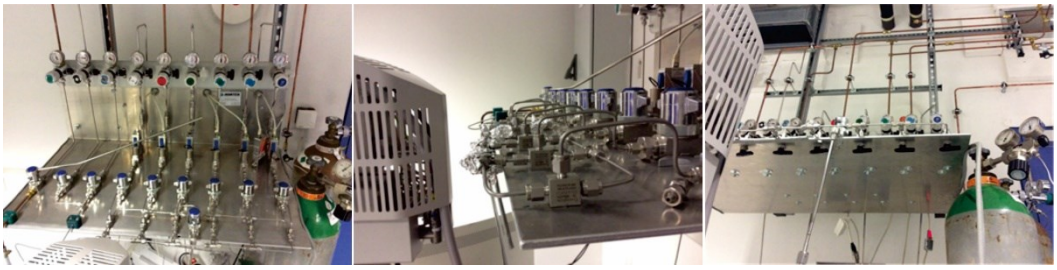

Figure 1.10 A schematic overview of the modified gas feeding system, top view, side face and backside.

Heating stage: The commercial ESEM (Quanta 200) heating stage is based on resistance heating and the temperature can reach up to 1000 °C. However, several drawbacks made it not suitable for the investigation of catalyst dynamics: 1) thermo-resistance heating showed long time hysteresis during the temperature increase and decrease process, which made it impossible to quench the temperature and freeze the sample morphology for further investigation; 2) the temperature measurement is based on the current applied to the heating plate instead of monitoring the real temperature from the surface, which resulted in inaccuracies of temperature measurements. Therefore, a modified laser heating stage has been built.

The home-built laser heating is composed of a laser source, an optical fibre, a prism and a cooling stage (Figure 1.11A). A laser purchased from LIMO company worked as the heating source, with a power output of 40 W and a wavelength of 808 nm. An optical fibre (CeramOptec GmbH) with a length of 2.2 m was employed to guide the laser light into the ESEM specimen chamber. For transition into the chamber, the fibre was glued into a small hole drilled into a vacuum flange of the supply ports of the ESEM. The flange was sealed by an exchangeable rubber O-ring. Inside the specimen chamber, the laser was further converged by a collimator and guided by a prism to illuminate the backside of the sample (Figure 1.11B). During the heating process, the collimator and prism temperature could be too high to work properly, therefore, a cooling stage was built to maintain the temperature at 16 ~ 20 °C.

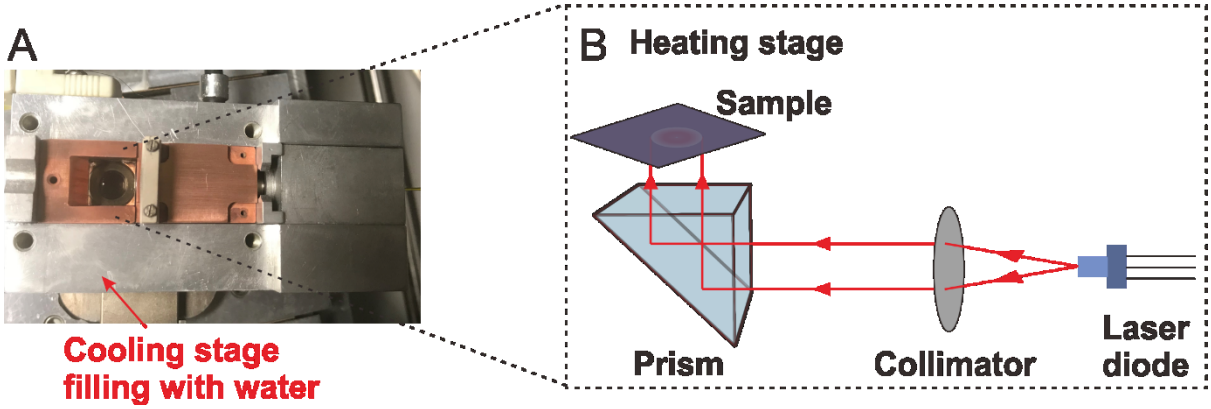

Figure 1.11 A) an overview of the heating stage, including prism, cooling stage and laser fiber; B) a scheme of laser path route.

Mass Spectrometer: A quadruple mass spectrometer (Pfeiffer OmniStar) was connected to the ESEM chamber to measure the gas compositions change of the ESEM sample environment. The base-pressure of the instrument is 2×10^{-5} Pa under high vacuum conditions, with residual gas compositions consisting mainly of water, N_2 and O_2 (Figure 1.12). The instrument is not ultra-high vacuum capable, due to the use of rubber O-ring for sealing. Therefore, the chamber cannot be baked out. Under low vacuum conditions, the mass spectrometer around 10^{-4} Pa was selected to monitor the gas composition during the reaction. H_2, O_2 and H_2O were the most common compounds analysed in our experiments.

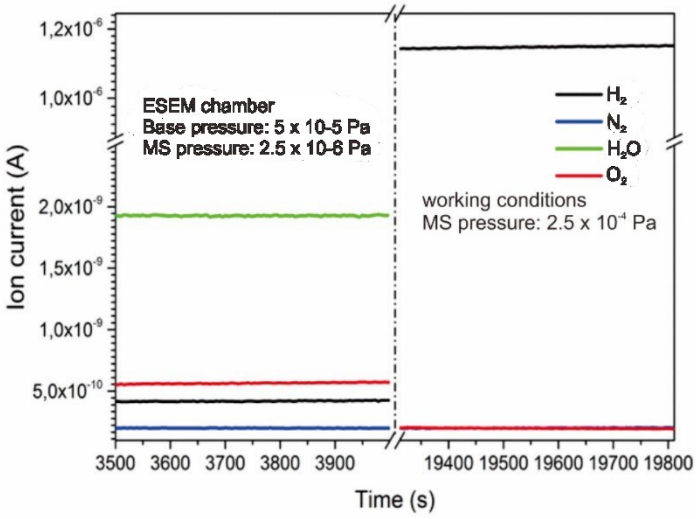

Figure 1.12 The base pressure of the ESEM under high vacuum conditions and low vacuum working conditions.

In summary, the modified ESEM is capable of investigating the surface morphological changes under reaction conditions and catalytic activity can be recorded *in situ*.

1.6 Scientific objective and outline of this work

Our aim is to investigate gas phase induced morphological changes of metal surface and to conclude on their relation to heterogeneous catalysis. A pre-requisite for harvesting this information is the possibility to detect online catalytic conversion. The combination of real-time imaging and on-line gas analysis would allow for observing the evolution of transient phases relevant for catalytic turnovers. Dynamics of the metal catalysts under reaction conditions are observed by environmental SEM, while the catalyst activity can be measured online using mass spectrometry.

To complement the results *in situ* XPS measurements of the surface are applied under similar conditions to identify the chemical changes that take place under the examined conditions. In most cases, focus ion beam (FIB) is also used to cut a region of interest from the catalyst, for subsequent investigation be TEM to identify the local chemical structures.

Hydrogen and oxygen have been selected as a model system in this work, due to the simplicity of the product distribution, in order to study the behaviour of metallic catalysts in a redox gas mixture. This investigation will provide important insights for understanding how active phases behave in reactive conditions and how this behaviour is related to activity. Three representative metals were chosen for this work–copper, nickel and platinum–, which are prominent catalysts in many industrial processes. In addition, they exhibit similarities in their crystal structure. All three crystalize in face centred cubic (fcc) structures. However, they have variable sensitivities for the adsorption of reductants and oxidants. For instance, compared to Ni and Pt, copper is more oxophilic and less easy to reduce. Conversely, Pt is very reactive to H_2 and less to O_2. Ni represents an intermediate case.[68]

In Chapter 2, *in situ* studies were performed to investigate the redox behaviour of copper using an environmental scanning electron microscope. The co-existence of three different morphologies oscillated with time at 700 °C at 4% O_2 in a hydrogen and oxygen mixture gas. Subsequently, *in situ* XPS was employed to characterize the copper oxidation states under similar conditions. Finally, the reasonable

mechanism was proposed to explain the occurrence of redox dynamics phenomena and to illustrate the phase transitions.

In Chapter 3, platinum redox dynamics were investigated in the presence of H_2 and O_2 mixtures at different temperatures, while monitoring the H_2 conversion. It was found that the platinum catalyst surface highly reconstructs in the presence of a specific mixture of gases. The morphological change rate correlates positively with the hydrogen conversion rate, demonstrating the significance of dynamic surfaces to catalytic activity.

In Chapter 4, synchronized oscillations on a nickel catalyst in a mixture of H_2 and O_2 at different temperatures were observed in the ESEM and MS. The highest activity corresponded to metallic nickel and the lowest catalytic activity is attributed to nickel oxide.

In Chapter 5, final conclusions and outlook of the thesis are provided.

1.7 References

1. Vedrine, J. C., Heterogeneous Catalysis on Metal Oxides. *Catalysts* **2017,** *7* (11).

2. Tamaru, K., In situ surface dynamics in heterogeneous catalysis. *Appl Catal a-Gen* **1997,** *151* (1), 167-177.

3. Wang, Y. F.; Xiao, Z. M.; Wu, L., Metal-nanoparticles Supported on Solid as Heterogeneous Catalysts. *Curr Org Chem* **2013,** *17* (12), 1325-1333.

4. Zambelli, T.; Wintterlin, J.; Trost, J.; Ertl, G., Identification of the "active sites" of a surface-catalyzed reaction. *Science* **1996,** *273* (5282), 1688-1690.

5. Salmeron, M.; Gale, R. J.; Somorjai, G. A., Molecular-Beam Study of H2-D2 Exchange-Reaction on Stepped Platinum Crystal-Surfaces - Dependence on Reactant Angle of Incidence. *J Chem Phys* **1977,** *67* (11), 5324-5334.

6. Behrens, M.; Studt, F.; Kasatkin, I.; Kuhl, S.; Havecker, M.; Abild-Pedersen, F.; Zander, S.; Girgsdies, F.; Kurr, P.; Kniep, B. L.; Tovar, M.; Fischer, R. W.; Norskov, J. K.; Schlogl, R., The Active Site of Methanol Synthesis over Cu/ZnO/Al2O3 Industrial Catalysts. *Science* **2012,** *336* (6083), 893-897.

7. Polarz, S.; Strunk, J.; Ischenko, V.; van den Berg, M. W. E.; Hinrichsen, O.; Muhler, M.; Driess, M., On the role of oxygen defects in the catalytic performance of zinc oxide. *Angew Chem Int Edit* **2006,** *45* (18), 2965-2969.

8. Amakawa, K.; Sun, L. L.; Guo, C. S.; Havecker, M.; Kube, P.; Wachs, I. E.; Lwin, S.; Frenkel, A. I.; Patlolla, A.; Hermann, K.; Schlogl, R.; Trunschke, A., How Strain Affects the Reactivity of Surface Metal Oxide Catalysts. *Angew Chem Int Edit* **2013,** *52* (51), 13553-13557.

9. Pfeifer, V.; Jones, T. E.; Velez, J. J. V.; Massue, C.; Greiner, M. T.; Arrigo, R.; Teschner, D.; Girgsdies, F.; Scherzer, M.; Allan, J.; Hashagen, M.; Weinberg, G.; Piccinin, S.; Havecker, M.; Knop-Gericke, A.; Schlogl, R., The electronic structure of iridium oxide electrodes active in water splitting. *Phys Chem Chem Phys* **2016,** *18* (4), 2292-2296.

10. Tamaru, K., Adsorption Measurements during Surface Catalysis. *B Chem Soc Jpn* **1958,** *31* (5), 666-667.

11. Greiner, M. T.; Jones, T. E.; Klyushin, A.; Knop-Gericke, A.; Schlogl, R., Ethylene Epoxidation at the Phase Transition of Copper Oxides. *J Am Chem Soc* **2017,** *139* (34), 11825-11832.

12. Wehner, S.; Baumann, F.; Ruckdeschel, M.; Kuppers, J., Kinetic phase transitions in the reaction CO+O -> CO2 on Ir(111) surfaces. *J Chem Phys* **2003,** *119* (13), 6823-6831.

13. Wu, X. G.; Kapral, R., Catalytic Co Oxidation on Pt Surfaces - a Lattice-Gas Cellular Automaton Model. *Physica A* **1992,** *188* (1-3), 284-301.

14. Reuter, K.; Scheffler, M., First-principles atomistic thermodynamics for oxidation catalysis: Surface phase diagrams and catalytically interesting regions. *Physical Review Letters* **2003,** *90* (4).

15. Reuter, K.; Scheffler, M., First-principles kinetic Monte Carlo simulations for heterogeneous catalysis: Application to the CO oxidation at RuO2(110). *Phys Rev B* **2006,** *73* (4).

16. Nibbelke, R. H.; Hoebink, J. H. B. J.; Marin, G. B., Kinetically induced multiplicity of steady states in integral catalytic reactors. *Chem Eng Sci* **1998,** *53* (12), 2195-2210.

17. McCaskill, J. S., A. S. Mikhailov: Foundations of Synergetics I Distributed Active Systems. Vol. 51 from: Springer Series in Synergetics. Springer Verlag, Berlin, ISBN 3-540-52775-3, 1990. 187 Pages, Price: DM 110, –. *Berichte der Bunsengesellschaft für physikalische Chemie* **1991,** *95* (10), 1308-1309.

18. Eiswirth, M., P. Gray und S. K. Scott: Chemical Oscillations and Instabilities – Non-linear Chemical Kinetics, Oxford Science Publications, Clarendon Press, Oxford 1990. 453 Seiten, Preis: £ 50,00. *Berichte der Bunsengesellschaft für physikalische Chemie* **1991,** *95* (4), 545-546.

19. Scott, S. K., Chapter 14 Instability, periodic reactions, and chaos. In *Comprehensive Chemical Kinetics*, Helfferich, F. G., Ed. Elsevier: 2004; Vol. 40, pp 445-459.

20. Zhdanov, V. P.; Kasemo, B., Kinetic Phase-Transitions in Simple Reactions on Solid-Surfaces. *Surf Sci Rep* **1994,** *20* (3), 111-189.

21. Ma, W. H., Polarization rotation associated critical phenomena in epitaxial PbTiO3 thin films near room temperature. *Aip Adv* **2016,** *6* (4).

22. Zhdanov, V. P.; Matsushima, T., Interplay of first-order kinetic and thermodynamic phase transitions in heterogeneous catalytic reactions. *Physical Review Letters* **2007,** *98* (3).

23. Nettesheim, S.; Vonoertzen, A.; Rotermund, H. H.; Ertl, G., Reaction-Diffusion Patterns in the Catalytic Cooxidation on Pt(110) - Front Propagation and Spiral Waves. *J Chem Phys* **1993,** *98* (12), 9977-9985.

24. Beusch, H.; Wicke, E.; Fieguth, P., Thermally and Kinetically Produced Instabilities in Reaction Behavior of Individual Catalyst Grains. *Chem-Ing-Tech* **1972,** *44* (7), 445-&.

25. Hugo, P., Stabilitiit und Zeitverhalten von DurchflubKreislauf-Reaktoren. *J Phys Chem B* **1970,** *74*, 121.

26. Cox, M. P.; Ertl, G.; Imbihl, R., Spatial Self-Organization of Surface-Structure during an Oscillating Catalytic Reaction. *Physical Review Letters* **1985,** *54* (15), 1725-1728.

27. Ertl, G.; Norton, P. R.; Rustig, J., Kinetic Oscillations in the Platinum-Catalyzed Oxidation of Co. *Physical Review Letters* **1982,** *49* (2), 177-180.

28. Ertl, G., Oscillatory Kinetics and Spatiotemporal Self-Organization in Reactions at Solid-Surfaces. *Science* **1991,** *254* (5039), 1750-1755.

29. Hendriksen, B. L. M.; Ackermann, M. D.; van Rijn, R.; Stoltz, D.; Popa, I.; Balmes, O.; Resta, A.; Wermeille, D.; Felici, R.; Ferrer, S.; Frenken, J. W. M., The role of steps in surface catalysis and reaction oscillations. *Nat Chem* **2010,** *2* (9), 730-734.

30. Shang, Y.; Guo, L., Facet-Controlled Synthetic Strategy of Cu2O-Based Crystals for Catalysis and Sensing. *Adv Sci* **2015,** *2* (10).

31. Han, X. G.; Jin, M. S.; Xie, S. F.; Kuang, Q.; Jiang, Z. Y.; Jiang, Y. Q.; Xie, Z. X.; Zheng, L. S., Synthesis of Tin Dioxide Octahedral Nanoparticles with Exposed High-Energy {221} Facets and Enhanced Gas-Sensing Properties. *Angew Chem Int Edit* **2009,** *48* (48), 9180-9183.

32. Zhang, J. A.; Langille, M. R.; Personick, M. L.; Zhang, K.; Li, S. Y.; Mirkin, C. A., Concave Cubic Gold Nanocrystals with High-Index Facets. *J Am Chem Soc* **2010,** *132* (40), 14012-14014.

33. Leng, M.; Liu, M. Z.; Zhang, Y. B.; Wang, Z. Q.; Yu, C.; Yang, X. G.; Zhang, H. J.; Wang, C., Polyhedral 50-Facet Cu2O Microcrystals Partially Enclosed by {311} High-Index Planes: Synthesis and Enhanced Catalytic CO Oxidation Activity. *J Am Chem Soc* **2010,** *132* (48), 17084-17087.

34. Vendelbo, S. B.; Elkjaer, C. F.; Falsig, H.; Puspitasari, I.; Dona, P.; Mele, L.; Morana, B.; Nelissen, B. J.; van Rijn, R.; Creemer, J. F.; Kooyman, P. J.; Helveg, S.,

Visualization of oscillatory behaviour of Pt nanoparticles catalysing CO oxidation. *Nat Mater* **2014,** *13* (9), 884-890.

35. Wilde, M.; Fukutani, K.; Ludwig, W.; Brandt, B.; Fischer, J. H.; Schauermann, S.; Freund, H. J., Influence of Carbon Deposition on the Hydrogen Distribution in Pd Nanoparticles and Their Reactivity in Olefin Hydrogenation. *Angew Chem Int Edit* **2008,** *47* (48), 9289-9293.

36. Johnson, A. D.; Daley, S. P.; Utz, A. L.; Ceyer, S. T., The Chemistry of Bulk Hydrogen - Reaction of Hydrogen Embedded in Nickel with Adsorbed Ch3. *Science* **1992,** *257* (5067), 223-225.

37. Maynard, K. J.; Johnson, A. D.; Daley, S. P.; Ceyer, S. T., A New Mechanism for Absorption - Collision-Induced Absorption. *Faraday Discuss* **1991,** *91*, 437-449.

38. Morcrette, M.; Chabre, Y.; Vaughan, G.; Amatucci, G.; Leriche, J. B.; Patoux, S.; Masquelier, C.; Tarascon, J. M., In situ X-ray diffraction techniques as a powerful tool to study battery electrode materials. *Electrochim Acta* **2002,** *47* (19), 3137-3149.

39. Girgsdies, F.; Schlogl, R.; Trunschke, A., In-situ X-ray diffraction study of phase crystallization from an amorphous MoVTeNb oxide catalyst precursor. *Catal Commun* **2012,** *18*, 60-62.

40. Nix, R. M.; Rayment, T.; Lambert, R. M.; Jennings, J. R.; Owen, G., An Insitu X-Ray-Diffraction Study of the Activation and Performance of Methanol Synthesis Catalysts Derived from Rare-Earth Copper-Alloys. *J Catal* **1987,** *106* (1), 216-234.

41. Kaichev, V. V.; Gladky, A. Y.; Prosvirin, I. P.; Saraev, A. A.; Havecker, M.; Knop-Gericke, A.; Schlogl, R.; Bukhtiyarov, V. I., In situ XPS study of self-sustained oscillations in catalytic oxidation of propane over nickel. *Surf Sci* **2013,** *609*, 113-118.

42. Turner, N. H., X-ray photoelectron and Auger electron spectroscopy (Reprinted from Analytical Instrumentation Handbook, Second Edition, Revised and Expanded, pg 863, 1997). *Appl Spectrosc Rev* **2000,** *35* (3), 203-254.

43. Arrigo, R.; Havecker, M.; Schuster, M. E.; Ranjan, C.; Stotz, E.; Knop-Gericke, A.; Schlogl, R., In Situ Study of the Gas-Phase Electrolysis of Water on Platinum by NAP-XPS. *Angew Chem Int Edit* **2013,** *52* (44), 11660-11664.

44. Casalongue, H. G. S.; Ng, M. L.; Kaya, S.; Friebel, D.; Ogasawara, H.; Nilsson, A., In Situ Observation of Surface Species on Iridium Oxide Nanoparticles during the Oxygen Evolution Reaction. *Angew Chem Int Edit* **2014,** *53* (28), 7169-7172.

45. Knop-Gericke, A.; Kleimenov, E.; Havecker, M.; Blume, R.; Teschner, D.; Zafeiratos, S.; Schlogl, R.; Bukhtiyarov, V. I.; Kaichev, V. V.; Prosvirin, I. P.; Nizovskii, A. I.; Bluhm, H.; Barinov, A.; Dudin, P.; Kiskinova, M., X-Ray Photoelectron Spectroscopy for Investigation of Heterogeneous Catalytic Processes. *Adv Catal* **2009,** *52*, 213-272.

46. Kaichev, V. V.; Saraev, A. A.; Matveev, A. V.; Dubinin, Y. V.; Knop-Gericke, A.; Bukhtiyarov, V. I., In Situ NAP-XPS and Mass Spectrometry Study of the Oxidation of Propylene over Palladium. *J Phys Chem C* **2018,** *122* (8), 4315-4323.

47. Tao, F.; Tang, D.; Salmeron, M.; Somorjai, G. A., A new scanning tunneling microscope reactor used for high-pressure and high-temperature catalysis studies. *Rev Sci Instrum* **2008,** *79* (8).

48. Rossler, M.; Geng, P.; Wintterlin, J., A high-pressure scanning tunneling microscope for studying heterogeneous catalysis. *Rev Sci Instrum* **2005,** *76* (2).

49. Laegsgaard, E.; Osterlund, L.; Thostrup, P.; Rasmussen, P. B.; Stensgaard, I.; Besenbacher, F., A high-pressure scanning tunneling microscope. *Rev Sci Instrum* **2001,** *72* (9), 3537-3542.

50. Mcintyre, B. J.; Salmeron, M. B.; Somorjai, G. A., A Scanning Tunneling Microscope That Operates at High-Pressures and High-Temperatures (430-K) and during Catalytic Reactions. *Catal Lett* **1992,** *14* (3-4), 263-269.

51. Herbschleb, C. T.; van der Tuijn, P. C.; Roobol, S. B.; Navarro, V.; Bakker, J. W.; Liu, Q.; Stoltz, D.; Canas-Ventura, M. E.; Verdoes, G.; van Spronsen, M. A.; Bergman, M.; Crama, L.; Taminiau, I.; Ofitserov, A.; van Baarle, G. J. C.; Frenken, J. W. M., The ReactorSTM: Atomically resolved scanning tunneling microscopy under high-pressure, high-temperature catalytic reaction conditions. *Rev Sci Instrum* **2014,** *85* (8).

52. Ando, T.; Kodera, N.; Maruyama, D.; Takai, E.; Saito, K.; Toda, A., A high-speed atomic force microscope for studying biological macromolecules in action. *Jpn J Appl Phys 1* **2002,** *41* (7b), 4851-4856.

53. Ando, T.; Kodera, N.; Naito, Y.; Kinoshita, T.; Furuta, K.; Toyoshima, Y. Y., A high-speed atomic force microscope for studying biological macromolecules in action. *Chemphyschem* **2003,** *4* (11), 1196-1202.

54. Schitter, G., Advanced Mechatronics for Precision Engineering and Mechatronic Imaging Systems. *IFAC-PapersOnLine* **2015,** *48* (1), 942-943.

55. Suchorski, Y.; Spiel, C.; Vogel, D.; Drachsel, W.; Schlogl, R.; Rupprechtert, G., Local Reaction Kinetics by Imaging: CO Oxidation on Polycrystalline Platinum. *Chemphyschem* **2010,** *11* (15), 3231-3235.

56. Vogel, D.; Spiel, C.; Suchorski, Y.; Urich, A.; Schlogl, R.; Rupprechter, G., Mapping the local reaction kinetics by PEEM: CO oxidation on individual (100)-type grains of Pt foil. *Surf Sci* **2011,** *605* (23-24), 1999-2005.

57. Novikov, Y. A., Virtual Scanning Electron Microscope: 2. Principles of Instrument Construction. *J Surf Investig* **2015,** *9* (3), 604-611.

58. Noro, H., The Principle of Scanning Electron Microscope / Electron Probe Micro Analyzer and Information to be Provided. *Tetsu to Hagane* **2013,** *99* (5), 249-256.

59. Murat, M., Scanning Electron-Microscope - Principles, Apparatus, Use in Chemistry of Solids and Materials. *Chim Ind-Milan* **1975,** *57* (2), 99-113.

60. Donoso, E., Principles and Operation of the Scanning Electron-Microscope. *Arch Biol Med Exp* **1979,** *12* (4), 492-492.

61. Baumgarten, N., Environmental SEM premières. *Nature* **1989,** *341*, 81.

62. Danilatos, G. D., Design and Construction of an Environmental Sem .4. *Scanning* **1990,** *12* (1), 23-27.

63. Thiel, B. L.; Toth, M., Secondary electron contrast in low-vacuum/environmental scanning electron microscopy of dielectrics. *J Appl Phys* **2005,** *97* (5).

64. Danilatos, G. D., Foundations of Environmental Scanning Electron-Microscopy. *Adv Electron El Phys* **1988,** *71*, 109-250.

65. Donald, A. M., The use of environmental scanning electron microscopy for imaging wet and insulating materials. *Nat Mater* **2003,** *2* (8), 511-516.

66. Meredith, P.; Donald, A. M.; Thiel, B., Electron-gas interactions in the environmental scanning electron microscopes gaseous detector. *Scanning* **1996,** *18* (7), 467-473.

67. Demichelis, A.; Sassi, G.; Sassi, M. P., Metrological performances of mass flow controllers for dynamic gas dilution. *Accredit Qual Assur* **2013,** *18* (3), 181-186.

68. Kepp, K. P., A Quantitative Scale of Oxophilicity and Thiophilicity. *Inorg Chem* **2016,** *55* (18), 9461-9470.

2 The redox dynamics of copper revealed by *in situ* scanning electron microscopy

2.1 Abstract

Using *in situ* scanning electron microscopy, we have performed studies on the redox behaviour of copper in the model reaction of oxygen with hydrogen. Real-time observation of the dynamic interplay between gas-phase reactants, temperature and the surface of the substrate reveals rich structural dynamics that are associated with the competing action of the simultaneously present oxidizing and reducing agents. On polycrystalline Cu foils, the interaction between the reactive gas-phase and the Cu surface induces grain-orientation dependent modifications. This modification consequently changes the interaction strength with the two gas phase reactants, resulting in a delayed feedback mechanism that induces oscillatory redox phase transitions. Under these conditions, the surface shows a constant inter-conversion between metal and oxide. A dynamic state between the three co-existing phases is established in which the resulting average composition of the surface is controlled by the H_2/O_2 ratio and temperature. At low oxygen concentration (4% in total pressure 20 Pa), lateral coupling between local redox oscillations can result in the formation of complex spatiotemporal dynamics. Detailed analysis of the observed morphological changes by *in situ* SEM and characterization of the involved phases by *in situ* X-ray absorption and scanning photoemission microscopy provides insight into the three surface phases that are involved in the metal-cuprite transition and into the local chemistry of the morphological dynamics. The work highlights the importance of combing microscopy and spectroscopy executed under the same reaction conditions for disentangling the interplay of surface and sub-surface chemistry occurring under elevated chemical potentials which could be of relevance in heterogeneously catalysed reactions.

2.2 Introduction

In heterogeneous catalysis, solids facilitate reactions between adsorbed molecules. The reactant molecules can also chemically alter the catalyst, and in doing so, can give rise to a dynamically changing catalyst surface, the coexistence of multiple surface phases, and even the formation of meta-stable phases.[1-5] Such situations occur when an oxidizable or reducible material is used to catalyse a redox reaction. Examples are methanol oxidation on copper,[6-8] ethylene oxidation on silver, or CO oxidation over palladium.[9] In oxidation reactions, an oxidant and reductant are mixed together over the catalyst's surface. The action of the oxidant and reductant counteract each other with respect to the phase stability of the catalyst material. The result is a dynamic structure fluctuating between oxidized and reduced states, with fluctuating phases and surface terminations at any point in time.[8, 10] It is a major challenge for catalysis research to determine what phases are present under such conditions and how coexistence and inter-conversion correlate with catalytic activity. This feat requires experimental insight about non-equilibrium processes, which is one of the reasons why *in situ* characterization methods are so vital.[11]

Recent years have seen a major growth in the use of *in situ* methods for studying catalysts.[9, 12-14] *In situ* methods are so essential for understanding catalysts because a finite chemical potential of the gas phase larger than the conditions of more conventional surface science reaction experiments may be required to transform the catalyst into its reactive form. In practical catalysis science, this effect is well known under the term 'activation'.[9, 15] As mentioned above, the redox action of mixed oxidizing and reducing agents can give rise to repeated phase transitions on a catalyst surface.[16] During such inter-conversion periods, high energy transient structures can arise. These structures are excellent candidates for active sites. Such sites require non-equilibrium geometric and electronic structures in order to execute their catalytic function. In contrast to the conventional wisdom of static active sites being produced during catalyst synthesis, the process of dynamical restructuring provides a convenient mechanism of generating high-energy sites for catalytic action.

In such a picture, an active site is constantly regenerated through phase dynamics. The present approach attempts to gain conceptual knowledge of such scenarios using a model study that exemplifies structural dynamics. What kinds of sites

transiently exist on a dynamic surface, is still very much a mystery to the scientific community. The origins of phase transition phenomena and their evolution are difficult to study because they must be examined using *in situ* methods. Furthermore, they are difficult to predict using computational methods because transition states represent non-equilibrium structures.[11]

In the present work we investigate the behaviour of copper when exposed to a model redox reaction mixture of H_2 and O_2. Copper was chosen because of its relevance in a number of industrial redox reactions, such as methanol oxidation ($CH_3OH + O_2$)[17], water gas shift reaction[18], CO_2 reduction[19] and as an active component in methanol synthesis catalysts.[20] To date, several surface science methods have been applied for surface oxidation mechanism and phase transitions.[21] However, despite of the detailed integral spectroscopic characterization, spatially resolved insight about the associated morphological and chemical dynamics during phase transitions is still scarce.

We have optimized a commercial environmental scanning electron microscope (ESEM) for *in situ* observation of structural dynamics of metals in a gas atmosphere. The instrument is equipped with a gas feeding station, a home-built laser heating system. By combining direct imaging with additional chemical-state-sensitive methods, we are able to correlate the morphological dynamics with information about the involved phases. While near-ambient pressure X-ray photoemission spectroscopy (NAP-XPS) delivers information about the chemical composition of the involved phases in the redox material, environmental scanning photoemission microscopy (ESPEM) complements the *in situ* SEM data with laterally resolved chemical information.

2.3 Experimental section

2.3.1 Sample preparation

Polycrystalline copper foils of 0.1 mm thickness and 99.998% purity were purchased from Advent Research Materials Ltd. Prior to all experiments, copper samples were cleaned using ion polishing (Gatan Model 691, 1 hour @ 5 kV Ar^+), followed by annealing in 20 Pa high purity (99.999%) H_2 at 700 °C inside the chamber of an environmental scanning electron microscope (ESEM) for 2 hours. The high-

temperature annealing removes surface contaminants and induces grain growth and migration[4-6], as detailed in Supplementary Fig.2.1 & Video S2.1. Increased contrast in the secondary electron image and brightness variations caused by grain-orientation dependent electron channelling conditions and differences in the work-function confirm a high degree of surface reconstruction.[22]

2.3.2 *In situ* studies

In situ scanning electron microscopy measurements were performed using a commercial ESEM (FEI Quantum 200). The base-pressure of the instrument is 2×10^{-5} Pa, with residual gas composed mainly of water, N_2 and O_2. The instrument is equipped with a home-built infrared laser heating stage, oil-free pre-vacuum pumps and a gas supply unit with mass flow controllers (Bronkhorst). Each time a new sample was loaded, the ESEM chamber was pumped to 10^{-3} Pa and purged with nitrogen three times. During *in situ* measurements, reaction gases were directly fed into the differentially-pumped chamber of the microscope. At a hydrogen flow of 10 sccm and oxygen flows between 0 sccm and 5 sccm, the pressure in the chamber equilibrated in the range between 20 and 50 Pa. The temperature was measured via type K thermocouples that were directly spot-welded onto the sample.

Near-ambient X-ray absorption fine structure (NEXAFS) measurements were carried out at the Innovative Station for *In situ* Spectroscopy (ISISS) beamline at the Helmholz-Zentrum Berlin (HZB) synchrotron light source (BESSY II). The NAP-XPS set-up is equipped with a Specs GmbH Phoibos 150 differentially-pumped electrostatic lens and analyser system. It contains a reaction cell in which the sample is mounted and enables measurements at pressures of up to 100 Pa. Details of the equipment are available elsewhere.[7, 23] During *in situ* experiments, reaction gases (from Westfalen AG, purities: hydrogen and oxygen 6.0N) were continuously fed into the reaction cell via mass-flow controllers. The pressure in the chamber was maintained at 20 Pa during the measurements. The sample was heated from the back side using an infrared laser, and the temperature was measured by type K thermocouples that were mechanically clamped onto the surface of the sample.

Environmental scanning photoelectron microscopy measurements were performed at the ESCAmicroscopy beamline at the Elettra synchrotron facility in Trieste, Italy. The setup consists of a hemispherical energy analyser, attached to a chamber that

contains a specially designed cell that can be back-filled to 20 Pa of a reaction gas mixture. The reaction cell is separated from the high vacuum region via a 300 µm diameter aperture. The X-ray radiation used as the excitation source was generated via an undulator and focused using Fresnel optics onto a 190 nm-diameter spot on the surface of the sample. The photon energy used for the measurements was 1071 eV. The sample was heated during the measurements using a boron-nitride-coated resistive heater. Further details of the experimental set-up can be found elsewhere.[24]

2.3.3 *Ex situ* analysis

Energy dispersive X-ray (EDX) mapping was performed in the chamber of the ESEM using a Si(Li) detector from Bruker. Focused ion beam milling (FIB) was performed in a FEI (Thermo Fisher) Heilos G3 FIB/SEM. High resolution transmission electron microscopy (HRTEM), high angle annular dark-field (HAADF) scanning TEM (STEM), electron energy-loss spectroscopy (EELS) and EDX mapping on TEM lamella was performed using a double corrected JEOL ARM 200F instrument that is equipped with a Gatan Quantum ER imaging filter and a JEOL silicon drift EDX detector.

2.4 Results

2.4.1 Morphological dynamics under red-ox conditions - phase diagram

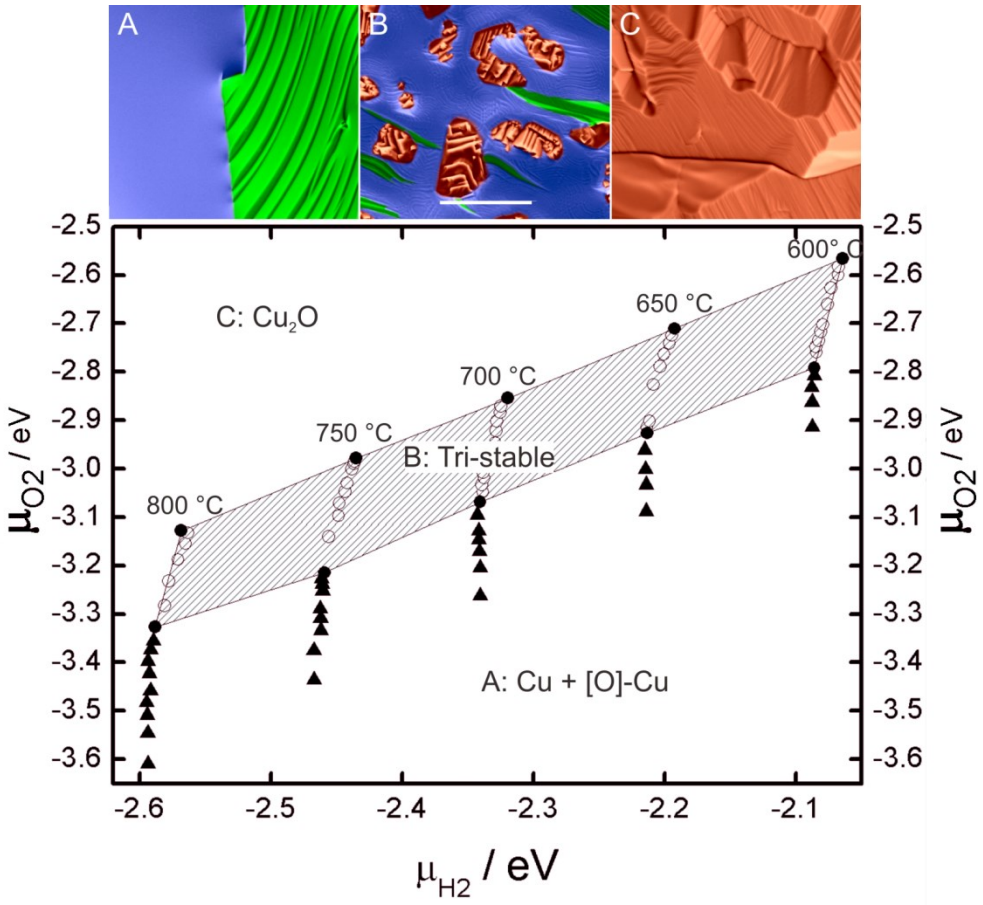

Figure 2.1 The plot shows three regimes in the copper phase diagram observed by ESEM at varying oxygen and hydrogen chemical potentials and at different temperatures. The detailed calculations are avaliable in Table S2.1: In regime A) the reductant dominates, and the catalyst remains in the metallic state, only some surfaces show oxygen induced reconstruction. In B), the counteracting oxidizing and reducing agent induce a dynamical interconversion between oxidized and reduced domains which are simultaneously present on the surface. In C), the oxidant dominates and the copper is oxidized. Scale bar is 5 μm. All sample started with the same pre-treatment (i.e. H_2 annealing), followed by a progressive increase of O_2 concentration. All measurements were performed in the pressure range from 20 to 50 Pa.

Samples were pre-treated by annealing in 20 Pa H_2, at 700 °C, then prior to the investigation, were held at the temperature of interest in H_2. Various temperatures between 600 °C and 800 °C were tested. At each temperature, the O_2 concentration was increased stepwise and at each step, the morphological changes of the sample

were monitored for two hours. The resulting data was used to construct the 'dynamic phase diagram' in Figure 2.1. The compositions for which dynamics were observed were noted and are indicated in the phase diagram. From the recorded movies the cuprite coverage was calculated at different points of the phase diagram (Figure S2.2 and 2.3). Except for 750 °C and 800 °C the onset of the tri-stable regime can be translated to a cuprite surface coverage of approximately 20% (Figure S2.2) and oscillation terminate for all temperatures at cuprite coverage of 99.5%. Further details related to the oxygen concentration change induced Cu_2O morphology coverage ratio and chemical potential variations are available in supporting information, seen in Figure S2.2 and S2.3, Video S2.2 to 2.26 and Table S2.1 to S2.2.

Figure 2.1 A-C shows representative ESEM images of a polycrystalline Cu foil at 700 °C under O_2 concentrations ranging from 0% to 37% in a H_2/O_2 atmosphere pressure. Depending on the H_2/O_2 ratio, three distinct regimes can be identified: As soon as oxygen is added (region A in Figure 2.1), the surface of the grains restructure. Initially, at low O_2 concentrations, the surface is faceted. As the O_2 concentration increases, the surface smoothens. As long as the oxygen concentration is below 3-5 % (depending on temperature), no oxide growth is observed. At oxygen concentrations above this threshold, the formation of corrugated oxide islands can be observed (region B in Figure 2.1). Due to the competing action of oxygen and hydrogen, a dynamic bi-stability is established, showing temporal changes. A time series is shown in Figure 2.2. The dynamic surface is characterized by the simultaneous presence of oxidized and metallic domains and a constant inter-conversion between the two. At high oxygen concentration (region C in Figure 2.1), the surface becomes fully covered with oxide. The O_2 partial pressures at which the boundaries between the different regimes are observed, depend on oxygen chemical potentials. In the diagram of Figure 2.1, one can see that at higher temperatures, higher O_2 partial pressures (related to lower chemical potential) are required to move out of the bi-stability regime into the oxidized regime. Similarly, lower O_2 chemical potential needed to transition from the metallic regime to bi-stability increases from 600 to 800 °C, respectively. The need for higher O_2 partial pressures with higher temperatures is expected, given that oxide chemical potentials decrease with increasing temperature.[25-27]

In the present work, we focus on the redox dynamics observed in regime B. To examine the redox process more closely, we have chosen conditions in which spatiotemporal surface dynamics are laterally coupled over extended regions and the oscillatory behaviour of the redox process is revealed. A time series of images recorded at two different magnifications at 700 °C in an atmosphere containing 4% oxygen (with oxygen chemical potential -3.07 eV) in hydrogen are shown in Figure 2.2.

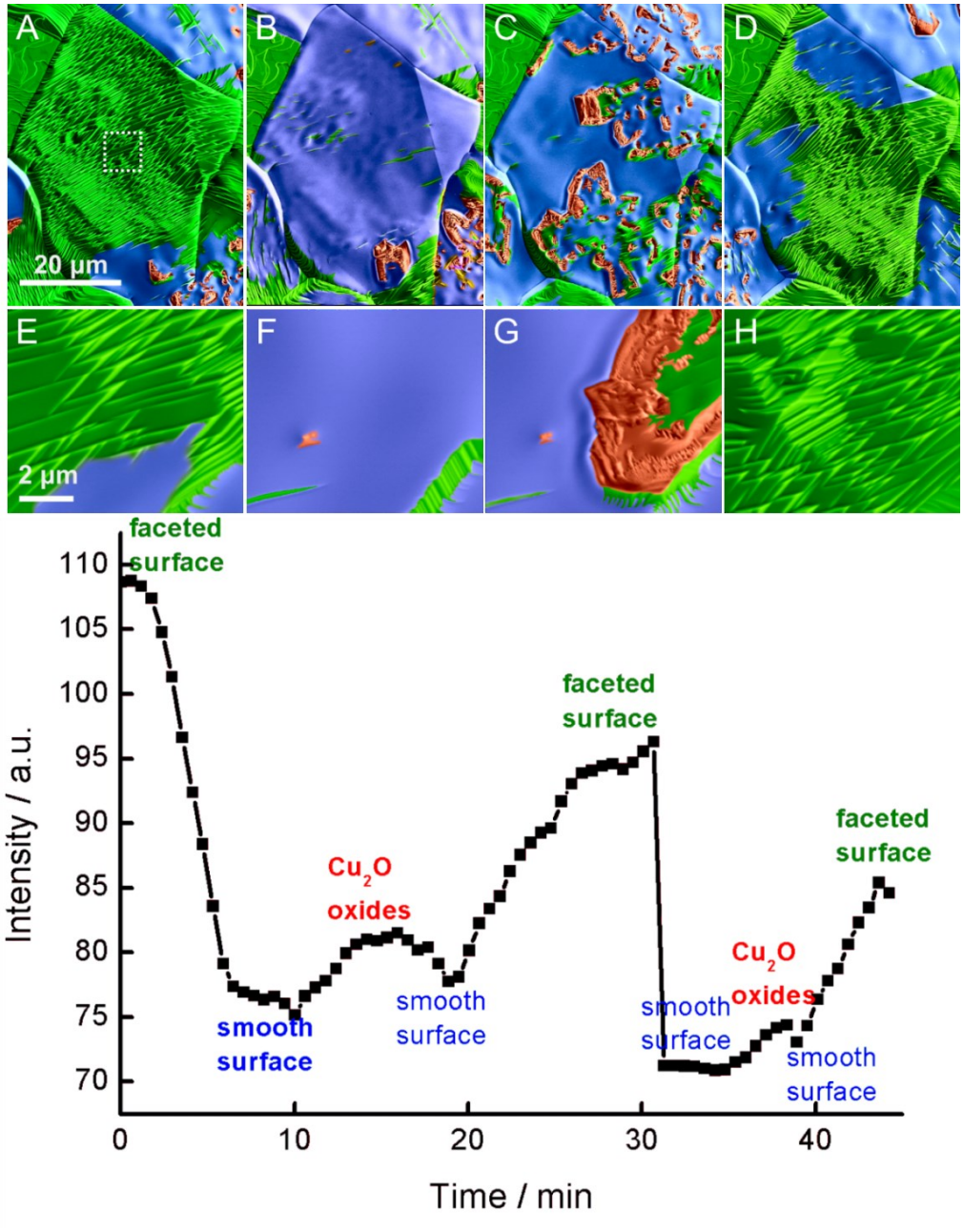

Figure 2.2 Surface morphological evolution with time can be seen in images recorded at 700 °C at 4% oxygen concentration, seen in Video S2.27. Colors are used to highlight the

different stages that are observed during a redox-cycle: green is for the faceted surface, the red color for the islands and blue for the flat morphology. Bottom row of SEM images shows snapshots from the central grain (marked by white square) at higher magnification under identical conditions, but recorded during a later redox-cycle, seen in Video S2.28. The different morphologies coverage ratios are also extracted from the Video 2.28 and plotted in Figure S2.4. The intensity changes with time from marked region (Video S2.27) are also extracted and plotted with time.

From panels Figure 2.2A-D one can see that the interaction of the surface with the gas phase induces a sequence of stages that are characterized by distinct morphologies. Starting with a heavily facetted surface of the central grain in Figure 2.2A, the surface transforms into a microscopically smooth state (Figure 2.2B). Thereafter, the formation of copper oxide islands is observed (Figure 2.2C). They propagate in a wave-like manner across the surface and are swiftly reduced in the hydrogen dominated atmosphere. With the disappearance of the oxide islands, the facetted surface state is re-established (Figure 2.2D) and the redox-cycle closed. Figure E – H are snapshots from the central spots at higher resolutions but recorded for the later cycles. At 700 °C and a total pressure of around 30 Pa, one complete redox-cycle takes about 30 minutes. The dynamics are thus relatively slow and can nicely be followed by *in situ* SEM, even when using a scanning speed of several 10 s per image frame. This cycle of re-occurring morphologies continues as long as the experimental conditions remain unchanged. Interestingly, oxide growth is exclusively observed on the smooth surface, and the locally observed sequence of surface reconstruction, surface flattening and oxide formation- and reduction is repeated in the same order on all grains. This phenomenon also can be clearly reflected by the intensity plot in Figure 2.2, as the morphology evolution is accompanied by surface intensity changes, In Figure 2.3 and the movie provided in the supplementary information (Video S2.27), not only the oxide islands propagate across the surface in the form of waves, but also the boundaries between different phases of characteristic surface morphology meander across the surface of the polycrystalline foil in the form of waves.

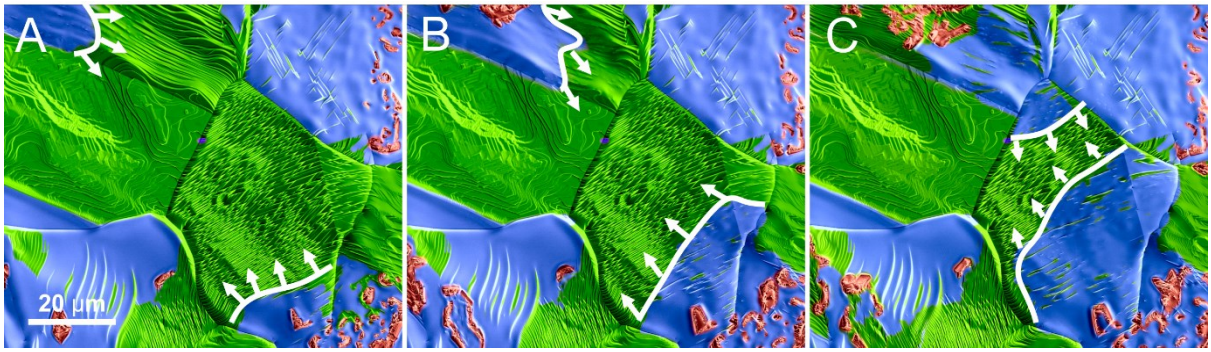

Figure 2.3 Wave-like propagation of different surface morphologies. Blue lines drawn on the SEM images roughly indicate the position of the boundaries between different surface structures. For video please see supplementary Video S2.27.

2.4.2 Identification of surface phases

2.4.2.1 *Ex situ* EDX, HRTEM and EELS characterization

In order to enable a discussion of the surface dynamics, the chemical nature of the observed phases needs to be addressed. To examine the oxide islands in the tri-stable state, the *in situ* experiments in the ESEM were interrupted and the state of the surface frozen by sudden removal of the reaction gases rapid cooling. A freezing of the surface dynamics is possible at any desired moment due to the low inertia of the laser heating stage, which enables cooling rates of up to 50 °C/s, and because of a vacuum system that allows fast switching to high-vacuum mode. After quenching, the samples were subjected to further *ex situ* analysis. The composition of the samples was first analysed in the ESEM using energy dispersive X-ray (EDX) mapping. Subsequently, samples were transferred to a FIB/SEM for target preparation of TEM lamella. High-resolution TEM imaging combined with electron energy-loss spectroscopy (EELS) analysis was used to study the surface structure and to identify compositional differences between smooth and faceted grains. Figure 2.4 A and B show an SEM image and corresponding O-K EDX map of the quenched tri-stable state. The EDX analysis clearly confirms the formation of copper oxide islands on the copper surface. However, is not sensitive enough to distinguish between flat and stepped surfaces of the metallic copper.

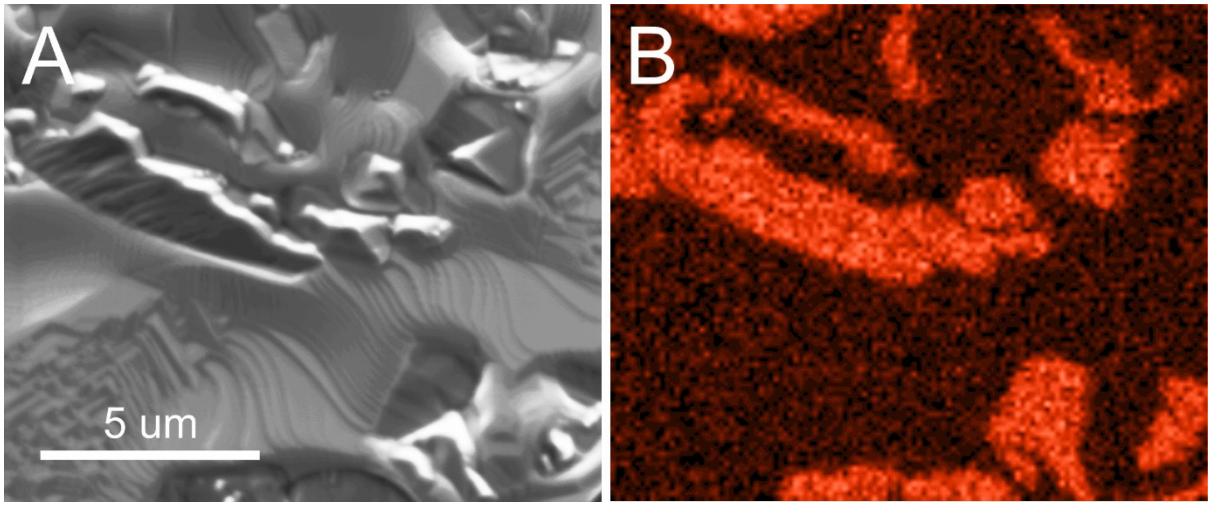

Figure 2.4 A) SEM images after redox dynamics; B) EDX element mapping of O (K) showed islands are oxygen rich.

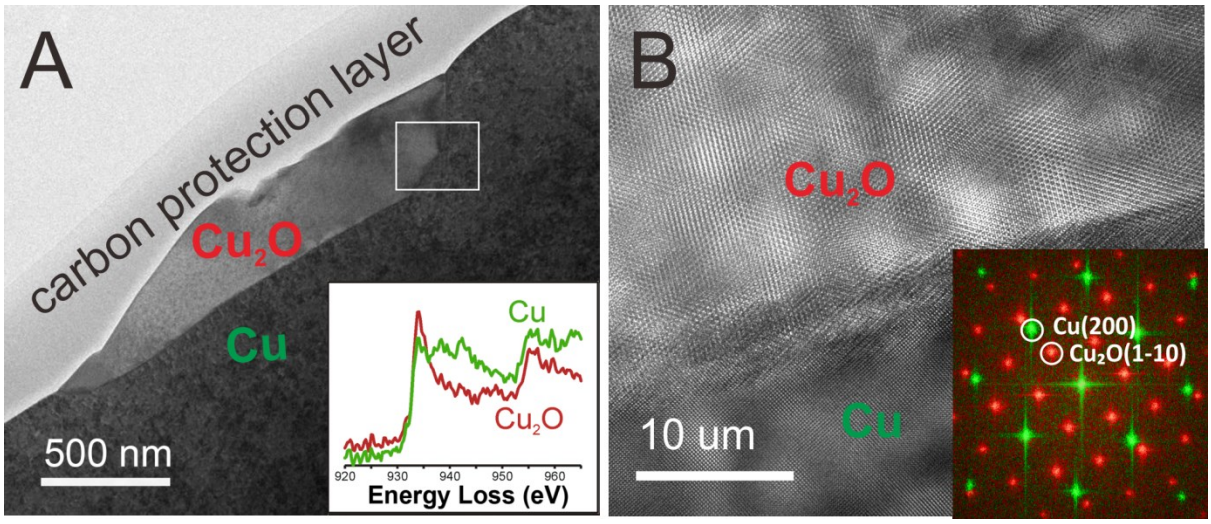

Figure 2.5 A) TEM low resolution overview of lamella by focus ion beam (FIB) cut after reaction and EELS spectrum; B) HRTEM images from the marked square and diffraction pattern of Cu_2O and Cu.

Analytical TEM investigation performed on a lamella cut through an oxide island is summarized in Figure 2.5 A and B. The carbon protection layer was deposited after the reaction in order to avoid surface oxidation during the transport and TEM preparation. From the cross section of the oxide island, one can see that the oxide layer has expanded below the copper metal surface, with the metal-oxide boundary reaching depth of several 100 nm (see Figure S2.6 image of complete cross-section). Oxidation is thus not limited to the surface, but also involves the bulk. Lattice fringe imaging shows that the structure of the oxide corresponds to Cu_2O. The chemical

state of the copper is further confirmed by the Cu L-edge EELS spectra, which shows the fingerprint of Cu^{1+} (inset of Figure 2.5A). The EELS spectra also confirm that the material surrounding the oxide islands is metallic Cu. High resolution TEM images of the Cu_2O/Cu interface, as well as and fast Fourier transform (FFT) analysis of the lattice fringes, show that the Cu_2O and Cu exhibit an epitaxial relationship and thus, a sharp interface. Furthermore, no void formation due to diffusion of copper atoms into the oxide layer is observed at the interface between metal and oxide. In Figure 2.5B, the Cu_2O/Cu interface is inclined with respect to the [001] zone axis of Cu and the viewing direction, so one cannot distinguish a clear atomically sharp interface from the image. However, the existence of sharp boundaries between Cu_2O and Cu with coherent and semi coherent crystalline interfaces is known[28] and their formation has recently been observed under *in situ* conditions[29-30], which allows us to conclude that this type of interface is not due to recrystallization during rapid cooling. Figure 2.5A reveals also some information about the structure of the metallic copper in the proximity of the oxide. From TEM EELS and HRTEM, no signs of oxygen termination can be detected, but a surface reconstructing leading to atomically flat facets can clearly be observed.

One should note that CuO is not observed in the redox dynamic conditions. The reason is likely that CuO cannot form directly on Cu metal. Rather it only forms on Cu_2O, and Cu_2O becomes reduced back to Cu metal before CuO can form. Furthermore, previously reported sub-stoichiometric oxides of copper, such as Cu_3O_4 and Cu_4O_3 can also be excluded, as these oxides contain Cu^{2+}, which would give rise to a distinctive white line in the EELS spectra, which is not observed in the TEM/EELS cross section.

After confirming that the oxide islands consist of Cu_2O, the nature of the stepped and smooth surfaces that reappear sequentially in the redox cycle, needs to be addressed. Site-selected FIB lamella were prepared for TEM cross section analysis, after quenching a sample that was investigated under 3% O_2 in an H_2/O_2 mixture at 700 °C in the ESEM. Under these conditions (regime A in Figure 2.1), the surface has turned from a smooth state, after hydrogen annealing, to one that shows grain-orientation dependent faceting with co-existence of flat and stepped surfaces.[31]

Figure 2.6A shows the region from which a lamella was extracted. It spans two grains with different surface morphology. An overview TEM image of the lamella is shown in Figure 2.6B. High resolution imaging shows that the faceted surface is due to the decomposition of a vicinal (310) plane of metallic copper into terraces of (110) and (210) orientation in figure 2.6C and D. The faceting process is driven by a reduction of surface energy, and was possibly enabled by the increased mobility of copper atoms at elevated temperature in the presence hydrogen and oxygen. A sphere model of the atomic structure of the surface is shown in Figure 2.6E. From high-resolution imaging and EELS spectroscopy (performed on different lamella, see also Figure 2.5 A, B), no sign of surface oxidation could be detected on the flat or faceted regions. From electron backscattering diffraction, the twin boundary was identified as sima-3, with the flat grain exposing a (110) surface (see Figure S2.5).

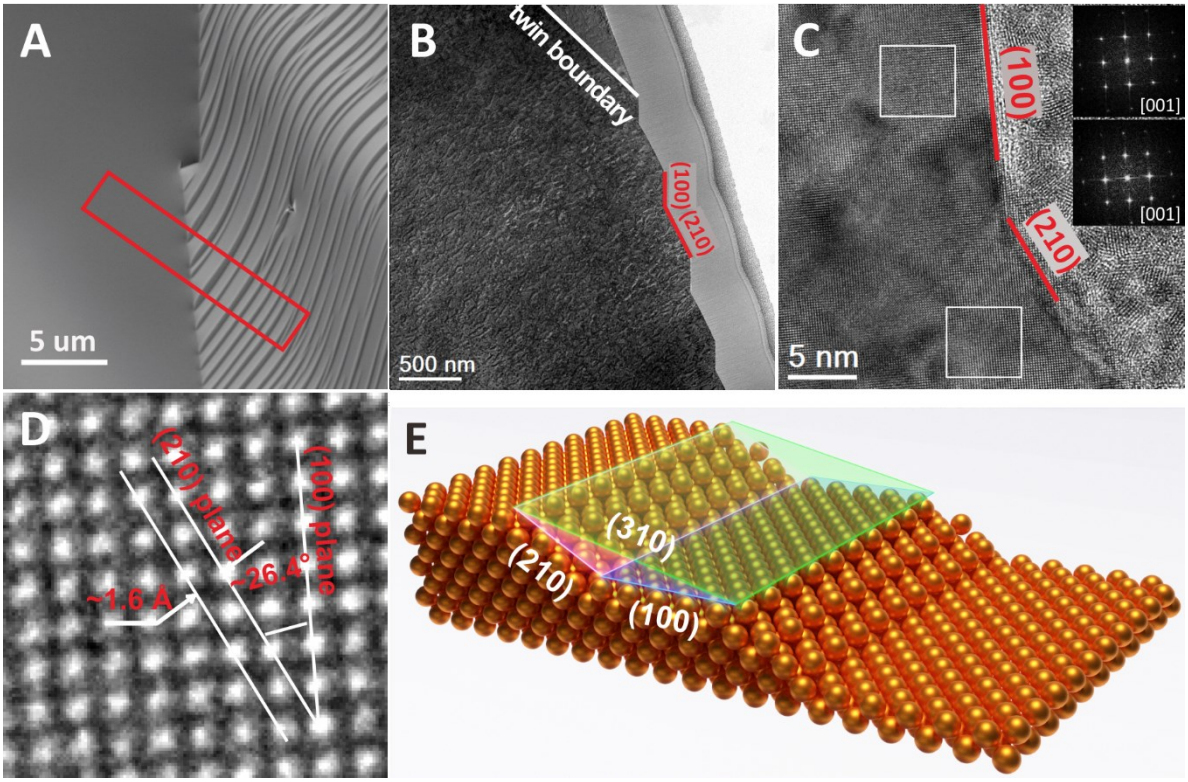

Figure 2.6 A) SEM image of copper showing two grains with different surface structure and the area from where the TEM lamella was extracted using FIB (red rectangle). B) Overview TEM image showing flat and stepped surfaces separated by a twin boundary. The steps are due to (210) and (100) planes. C) High-resolution image with lattice fringes and corresponding fast Fourier transformation (FFT) show that the surface facets are due to (210) and (100) planes. D) HRTEM image with Cu columns viewed in [001] direction with the

orientation of (100) and (210) panes indicated. E) Ball model showing the (100) and (210) surfaces of fcc copper.

2.4.2.2 *In situ* NEXAFS characterization

To investigate the chemical nature of the surface, we turned to *in situ* near-ambient pressure NEXAFS (Near-Edge X-ray Absorption Fine Structure). Figure 2.7 A and B show *in situ* Cu L_3- and O K-edge spectra of a copper foil measured at 700 °C, in a 25 Pa atmosphere of H_2 and at various partial pressures of O_2. These are the same conditions used in the ESEM observation. The Cu L_3 spectra show that the surface starts off metallic in pure H_2. When O_2 is added to the feed (p_{O2} = 0.8 Pa, corresponding to 3% O_2 in a H_2/O_2 atmosphere) the Cu L-edge indicates metallic Cu, while the O K-edge shows a feature with an edge at 529.5 eV, which is indicative of an O-terminated Cu surface.[32]

When the O_2 partial pressure is increased to 16 Pa, signs of Cu_2O begin to appear. Cu_2O is apparent from the Cu L-edge by the intensity increase at 932.9 eV (edge position), and in the O K-edge by the formation of a feature at 531.8 eV (edge position).[6-7] The conditions for these spectra are comparable to those in the ESEM measurements for which dynamic redox changes were observed (Figure 2.7C). This observation implies that the morphologies observed in ESEM represent a coexistence of O-terminated Cu and Cu_2O. As we have identified the island structures as Cu_2O using TEM, this implies that at least one of the flat or faceted morphologies is an O-terminated surface. The NEXAFS observations represent an integral measure of the Cu surface and can be interpreted as superpositions of cuprite and metallic states. Without spatially resolved surface chemical information, one cannot conclusively identify the cause and nature of the two surface morphologies.

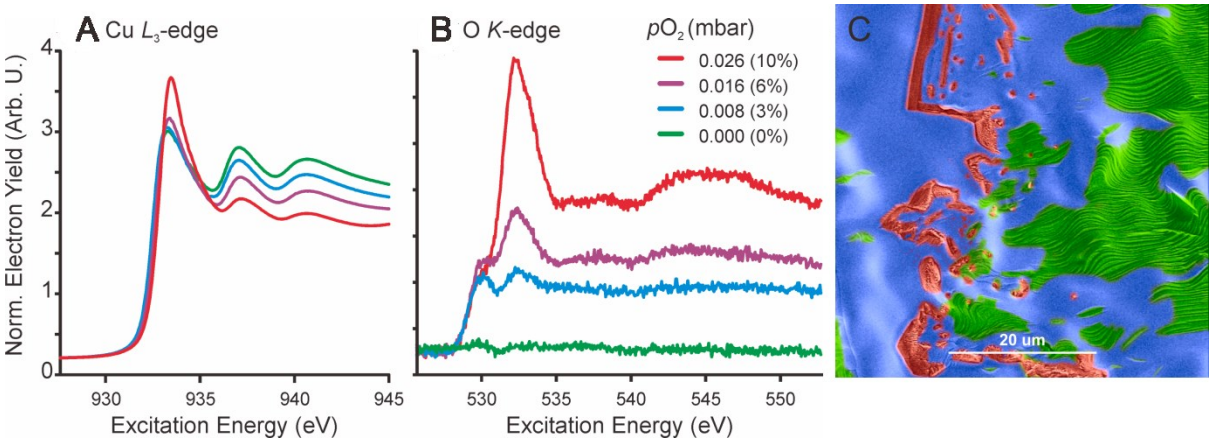

Figure 2.7. In situ photoemission measurements of copper foil at 700 °C in a 25 Pa mixture of hydrogen and oxygen, with various oxygen partial pressures ranging from 0% to 10%. (A) Cu L_3-edge NEXAFS spectra and (B) O K-edge NEXAFS spectra. (C) in situ SEM image exhibiting different surface morphologies. The image is colored to highlight the faceted Cu surface (yellow), smooth Cu surface (orange), and Cu_2O islands (red).

2.4.2.3 *In situ* scanning XPS characterization

To perform an *in situ* chemical-state sensitive, microscopic characterization of the material, we utilized micro-focused scanning photoemission microscopy (SPEM). This method uses a Fresnel zone plate to focus soft X-rays onto a 190 nm diameter spot at the surface of the sample, while photo-emitted electrons are energy filtered and detected by means of a hemispherical analyser. The sample is rastered in two dimensions while the photoemission signal is recorded. In this way, one can obtain spatially resolved XPS spectra with a spatial resolution of 190 nm. A recent development[33] has enabled this method to be applied in atmospheres up to 100 Pa, by placing the sample inside an isolated cell with a small aperture for letting in X-rays and detecting photoelectrons.

Using this method, we heated a polycrystalline Cu foil to 650 °C in a mixture of H_2 and O_2 at 20 Pa. A slightly lower temperature was chosen in order to slow down the kinetics of the process, as SPEM acquisition times are considerably longer than ESEM image acquisition times (ca. 5 minutes per map for SPEM versus 0.5 minutes per image for ESEM). A time series of SPEM maps showing the spatial distribution of $Cu2p_{3/2}$ intensity is shown in Figure 2.8a. These maps represent the intensity of the photoemission signal centered at 932.7 eV, and energy window of 2 eV. Thus, bight points indicate higher Cu content. Here one can observe the formation of dark

islands, which were identified using Cu LMM spectra as Cu_2O. The Cu_2O islands grow with time, and eventually bright intensity forms in the middle of the oxide islands. The bright patches showing up in the middle of the Cu_2O grain in frames 2-4 indicates the reduction of Cu_2O to Cu metal. The behaviour of the copper surface in the SPEM set-up nicely reproduces the dynamics that were observed by *in situ* SEM.

A large-area $Cu2p_{3/2}$ map is shown in Figure 2.8b, from which we measured high-resolution point spectra of the Cu LMM and O1s regions at the locations indicated in Figure 2.8b. The Cu LMM spectrum

at point A and B indicate that Cu in these regions is metallic, while the Cu LMM spectrum taken from point C indicates that it is Cu_2O, as expected. Note that spectrum A consists of a mixture of Cu LMM spectra from Cu_2O and Cu because the spatial resolution was not sufficient to isolate a purely metallic region on the oxide grain.

An interesting observation from the ESEM investigations was that oxide islands nucleate only on the smooth surface morphology (Figure 2.8c). From the *in situ* SPEM investigation, we can see that the smooth region surrounding the oxide islands consists of metallic Cu (based on the Cu LMM spectra), yet the O1s spectra of the same regions show the existence of an oxygen species. Based on the O1s binding energy and the lack of an oxide signal in the Cu LMM spectra, we expect these O-species to represent an O-terminated Cu surface. This observation suggests that the metallic copper surrounding the Cu_2O islands consists of O-terminated metallic Cu. As mentioned above, the spatial resolution was not sufficient to determine whether or not the reduction fronts formed on the Cu_2O islands also contain an O1s signal.

From the above paragraph, we conclude that the smooth surface morphology represents an O-terminated metallic surface. However, the faceted surface could not be prepared simultaneously with the Cu_2O islands during the SPEM experiments due to the lower temperature compared to the ESEM experiments. Nonetheless, regions were located where both smooth and faceted surfaces could be simultaneously observed, although from two different grains. Comparative SPEM measurements performed on two neighbouring grains in regime A, where one showed a smooth, the other a facetted surface, did not reveal any measurable

difference in oxygen termination (shown the corresponding oxygen spectra to the data A, B, C). In order to identify difference in termination that are not related to the orientation of the copper grain and obtain clues about the observed sequence of structures in the redox cycle, both reoccurring morphologies have to be captured on the same grain. So far, we have not been able to attain conditions in which the two could be sufficiently well distinguished and SPEM spectra recorded. At this stage, we are thus not able to draw any firm conclusions as to the chemical difference between smooth and faceted morphologies.

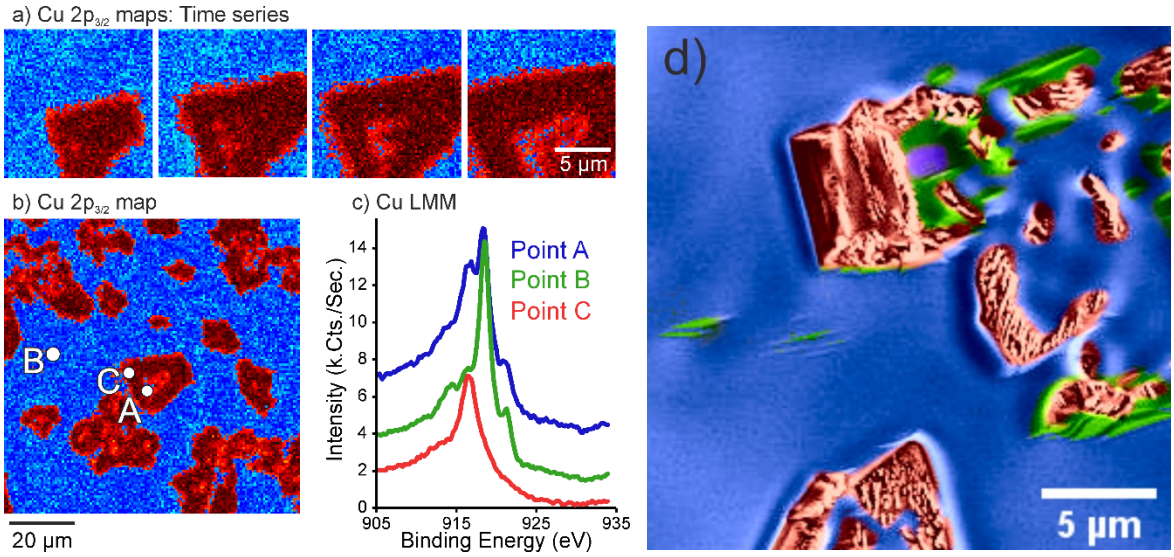

Figure 2.8 a) A scanning photoelectron microscopy Cu2p maps recorded the Cu surface evolution at around 4% O_2 and 96% H_2 at 650 °C. b) Cu surface morphology was frozen by pumping out the gas to high vacuum conditions at 650 °C. Three representative points have been chosen to investigate the copper state (A is the reduction front, B is the position between two oxides, C is the oxide island); c) Cu LMM spectra corresponding to point A showed the mixture of Cu and Cu_2O, point B showed metallic state and point C is Cu_2O, d) is the SEM images.

2.5 Discussion

In the following, we summarize the findings and build up a model to explain the about the observed dynamics. To understand the reactions that are occurring during redox dynamics, we will first consider some hypothetical scenarios. We consider what each of the possible phases would do when exposed to each of the pure reactant gases. These scenarios are: 1) pure metallic Cu in O_2; 2) O-terminated Cu in O_2; 3) Cu_2O in O_2; 4) pure metallic Cu in H_2; 5) O-terminated Cu in H_2; 6) Cu_2O in

H_2. All cases are considered ay high temperature of 700 °C. The first three cases consider heating the respective phases in O_2, while the last three consider heating the respective phases in H_2.

If metallic Cu were heated in pure O_2, Cu would become rapidly oxidized to Cu_2O. Previous works have shown that the initial stages of oxidation (i.e. before the nucleation of Cu_2O) involve the formation of an O-termination (i.e. an O monolayer on the Cu surface).[34] Cu_2O then nucleates and grows over the surface. Note that CuO would not form because it is not thermodynamically stable at such high temperatures (see phase diagram).[25] Thus Cu_2O would be the highest oxide expected at such temperatures. If O-terminated Cu were heated in O_2, it would simply proceed with oxidation to Cu_2O. If Cu_2O were heated in O_2 at 700 °C it would remain as Cu_2O, although it would likely have a relatively high concentration of defects.

In contrast, if metallic Cu were exposed to H_2 (in the complete absence of O_2) no O-terminated surface would form and no Cu_2O would form. The surface would remain metallic. Copper hydride would not be formed, as it is not stable above -60 °C[35]. Furthermore, H binds weakly to Cu, and desorbs from the surface at temperatures greater than 80 °C.[36] Thus, at high temperatures in pure H_2 one would expect a clean metallic Cu surface to be stable. If one were to expose an O-terminated surface to H_2 at 700 °C one would expect the O atoms on the surface to react with H_2 to form water, leaving the surface metallic and oxygen-free. This process has been observed spectroscopically using NAP-XPS, where the O-terminated surface loses its oxygen atoms at temperatures above 550 °C. If Cu_2O is exposed to H_2 at 700 °C it becomes reduced to Cu metal, where Cu nucleates on the Cu_2O surface, and passes through an O-terminated surface along the way to complete reduction.

To summarize, the stable state of copper at 700 °C in O_2 is Cu_2O, and the stable state of Cu in H_2 at 700 °C is metallic Cu. When we expose copper to a mixture of these reactants, the surface fluctuates between the two extremes, passing through intermediate states along the way. One can rank the various states according to their oxophilicity and nucleo-philicity. The oxophilicity increases in the order Cu > [O]-Cu > Cu_2O. Thus clean metallic Cu activates O_2 the fastest, while Cu_2O activates O_2 the slowest. In contrast, the nucleo-philicity follows the reverse order, i.e. Cu_2O > [O]-Cu >

Cu. Thus Cu_2O activates H_2 the fastest, while Cu activates H_2 the slowest. The competing rates of oxidation and reduction of the three possible phases, as well as the kinetic delay of phase nucleation gives rise, to complex dynamics, resulting in a tri-stability of morphologies and implies that for a simple Cu-Cu_2O phase transition three different phases are involved. These phases are illustrated in a schematic model of the multi-phase surface in Figure 2.9.

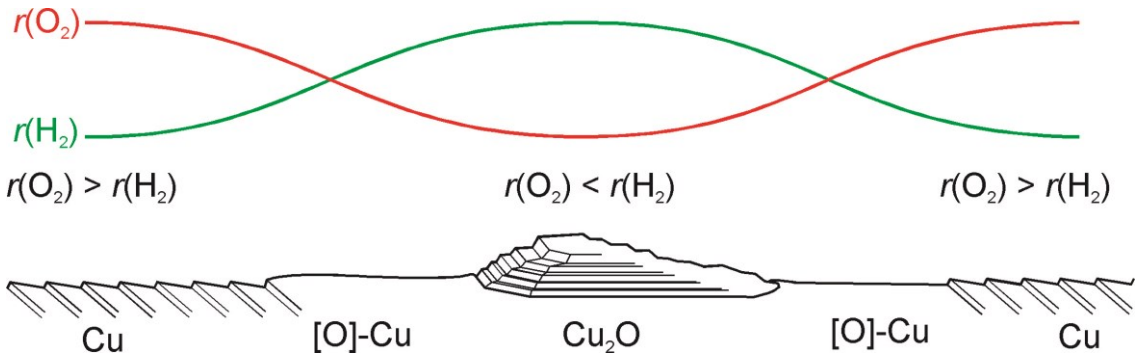

Figure 2.9 Illustration of different stages that the surface passes through during a redox cycle at 700 °C at 4% oxygen in a H_2/O_2 atmosphere and total pressure of 20 Pa. $r(O_2)$ and $r(H_2)$ represent the rates of O_2 adsorption and H_2 adsorption, respectively.

If we use $r(O_2)$ and $r(H_2)$ to represent rates of O_2 and H_2 activation, the on the Cu_2O phase $r(O_2) < r(H_2)$, while on a copper surface $r(O_2) > r(H_2)$. On an O-terminated surface, the rates would be intermediate, but it is not likely that $r(O_2) = r(H_2)$. The reason why a phase stays stable for a prolonged period of time, rather than being immediately oxidized or reduced, is that there is a nucleation barrier to the formation of a new phase, implying that phase transitions have a kinetic barrier associated with them. This property gives rise to the long-term temporal co-existence of the phases.

The difference between smooth and faceted morphologies

In the sequence of morphological changes that are observed during one redox-cycle, surface faceting and smoothening always precede oxide formation. Furthermore, the oxide always nucleates on the smooth morphology. In order to understand the reasons for this, we first need to address the difference in surface termination between the stepped and smooth surface. Note that morphology alone cannot serve as a complete characterization of a phase. However, the observation of morphological changes under constant conditions is a reliable indicator that a change in thermodynamic stability has occurred. Thus, if monitoring a single

crystallographic orientation with time, reversible morphology changes can be used as a reliable indicator of surface energy changes.

According to *in situ* SEM, surface restructuring and step formation on freshly reduced samples begin upon the admission of low concentrations of oxygen. Figure 2.10 shows that the surface of individual grains transit through different morphologies with increasing oxygen concentration. Eventually, at the point where the oxygen concentration is high enough to induce oxide growth, periodic fluctuations between faceted and smooth morphologies occurs. These changes in morphology indicate a change in surface energy. Since the macroscopic bulk structure of the surface stays the same, we infer that the difference between the faceted and smooth morphologies is a result of differences in surface termination.

Chemisorbed oxygen is known to induce several surface reconstructions on copper, such as well-ordered c(2 x 2) phases and the Cu-(2 ×) R45°-O missing-row reconstructions on the Cu(100) surface, the p(2×1) and c(6×2) reconstructions on Cu(110)[37], and the relatively complex '29'- and '44'-structures on Cu(111).[38-40] Each of these structures differ in their surface energies and result in different equilibrium crystal shapes that depend on oxygen chemical potential.[41] In general, crystal shapes tend to be more isotropic as oxygen chemical potential increases, because a larger variety of low-energy reconstructions are possible. Whereas on pure Cu, the crystal shape is dominated by the low-index faces (100), (110) and (111).

When comparing the faceted and smooth morphologies observed in the ESEM measurements, we can say that the surface energy of the smooth surface is more isotropic with regards to crystallographic orientation than the stepped surface is. Faceting occurs on the stepped surface because only a few low-index faces are stable. Unstable, high-index faces re-structure into low-index faces, resulting in an overall higher surface area but a lower total surface energy. In contrast, for a more isotropic crystal shapes, the high-index surfaces are relatively low energy, so the total surface energy can be minimized by taking on a rounder shape. Clearly, from comparison of stepped and smooth morphologies in the ESEM images, the smooth surface is more isotropic.

Based on these arguments, as well as the general trend of equilibrium crystal shape with O-chemical potential shown by Duan et. al..[41] we expect that the smooth

morphology represents a surface termination with higher O-content than the faceted morphology. This interpretation would be in-line with the observation that the Cu_2O islands only nucleate on the smooth morphology. That is, the O-chemical potential increases in the order stepped < smooth < Cu_2O.

Previous works have shown that the initial stages of Cu_2O nucleation occur after the surface is covered with an O-termination. For instance, Lahtonen.[31, 39-40, 42] showed that the oxidation of Cu(100) proceeds via the formation of a c(2×2) reconstruction, followed by the more O-rich Cu-(2 ×) R45°-O reconstruction, and then by the nucleation of Cu_2O. Interestingly Lahtonen *et al.* showed that the Cu-(2 ×) R45°-O phase is a particularly stable reconstruction. Thus, while the oxidation from clean Cu to the Cu-(2 ×) R45°-O reconstruction occurs rapidly, the further oxidation to Cu_2O is kinetically slower. This type of kinetics could have a strong influence on the dynamics observed in the ESEM measurements.

This interpretation is qualitatively in line with the SPEM observation, where first the formation of an O species with a binding energy of O-terminated Cu is observed, followed by formation of Cu_2O. Indeed, no Cu_2O formation has been observed without first seeing the precursor species.

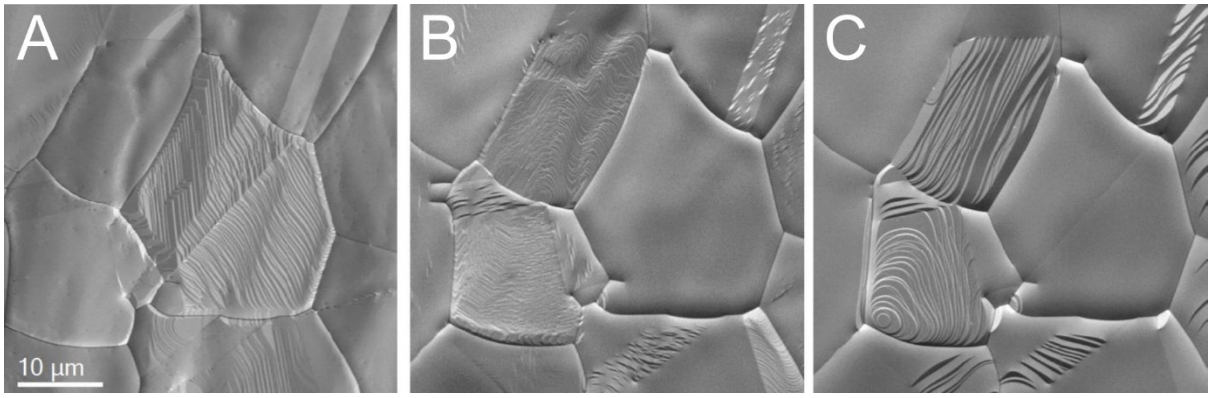

Figure 2.10 A: ESEM images recorded during H_2 annealing at 700 °C. The central grain is still showing a faceted surface. Complete surface flattening in pure hydrogen is only reached after prolonged annealing at high temperature (700 °C). B: After pumping away H_2 and introducing 5×10^{-3} Pa O_2, the surface of the central grain has flattened, while other grains exhibit faceting. C: Upon further increase of the O_2 pressure to 1×10^{-2} Pa, the surface morphologies adapted accordingly.

Based on these arguments, we propose a model of the reaction dynamics where the transitions from faceted to smooth to Cu_2O represent oxidation steps and the transitions from Cu_2O to smooth to faceted represent reduction steps. The reason for the complex dynamic and the tri-phase co-existence is that there is no single phase that is good at activating both reactants. Cu can activate O_2 well, but not H_2. Cu_2O can activate H_2 well but is slow at activating O_2. Thus Cu will continue to oxidize until it can activate H_2 faster than it can activate O_2. this process results in the surface swinging between two extremes, passing through an intermediate along the way. the presence of the intermediate phase is a consequence of the delayed kinetics of phase nucleation, due to nucleation barriers.

In particular, a phase change begins as a nucleation event. Once a new phase nucleates, it rapidly propagates over the surface, replacing the previous phase. The new phase remains until the nucleation another phase occurs and replaces it. The nucleation barriers to each phase change results in a delayed response in the oscillatory behaviour.

2.6 Conclusions

We have presented an *in situ* ESEM study of the morphological changes to copper that occur when it is heated in a mixture of O_2 and H_2. We find that under certain H_2:O_2 ratios three distinct morphologies coexist and dynamically transition among one another. Using post-reaction EDX, TEM and in- situ NEXAFS, these phases have been identified as Cu_2O and two surface terminations of metallic copper. We conclude that the morphologies represent three different surface phases, differing in terms of their oxygen chemical potentials. With time, the surface oscillates between surface phases of low oxygen chemical potential to phases of high oxygen chemical potential. Complex dynamics results from the kinetic barriers to transitions between the phases. Such complex dynamics are expected to play a role when catalysts that can exhibit several oxidation states are exposed to a mixture of oxidizing and reducing reactants. A complete understanding of such processes requires further developments in *in situ* methodologies, specifically spatially and time resolved chemical-state sensitive *in situ* methods.

2.7 References

1. Butcher, D. R.; Salmeron, M. B.; Somorjai, G. A., STM studies of adsorbate-induced surface restructuring of Pt(100) in ethylene adsorption, hydrogenation, and poisoning by CO. *Abstr Pap Am Chem S* **2010,** *240*.

2. Tamaru, K., Dynamic in-Situ Studies of Catalytic Reactions. *Appl Catal a-Gen* **1994,** *113* (2), 125-130.

3. Somorjai, G. A.; Vanhove, M. A., Adsorbate-Induced Restructuring of Surfaces. *Prog Surf Sci* **1989,** *30* (3-4), 201-231.

4. Besenbacher, F.; Klink, C.; Laegsgaard, E.; Nielsen, L. P.; Ruan, L.; Stensgaard, I., Dynamics of Adsorbate-Induced Restructuring and Reaction between Adsorbates on Cu and Ni Surfaces Studied by Scanning-Tunneling-Microscopy. *J Vac Sci Technol A* **1993,** *11* (4), 1637-1639.

5. Xu, F.; Mudiyanselage, K.; Baber, A. E.; Soldemo, M.; Weissenrieder, J.; White, M. G.; Stacchiola, D. J., Redox-Mediated Reconstruction of Copper during Carbon Monoxide Oxidation. *J Phys Chem C* **2014,** *118* (29), 15902-15909.

6. Bluhm, H.; Havecker, M.; Knop-Gericke, A.; Kleimenov, E.; Schlogl, R.; Teschner, D.; Bukhtiyarov, V. I.; Ogletree, D. F.; Salmeron, M., Methanol oxidation on a copper catalyst investigated using in situ X-ray photoelectron spectroscopy. *J Phys Chem B* **2004,** *108* (38), 14340-14347.

7. Greiner, M. T.; Jones, T. E.; Johnson, B. E.; Rocha, T. C. R.; Wang, Z. J.; Armbruster, M.; Willinger, M.; Knop-Gerickea, A.; Schlogl, R., The oxidation of copper catalysts during ethylene epoxidation. *Phys Chem Chem Phys* **2015,** *17* (38), 25073-25089.

8. Greiner, M. T.; Cao, J.; Jones, T. E.; Beeg, S.; Skorupska, K.; Carbonio, E. A.; Sezen, H.; Amati, M.; Gregoratti, L.; Willinger, M. G.; Knop-Gericke, A.; Schlogl, R., Phase Coexistence of Multiple Copper Oxides on AgCu Catalysts during Ethylene Epoxidation. *Acs Catal* **2018,** *8* (3), 2286-2295.

9. Hendriksen, B. L. M.; Ackermann, M. D.; van Rijn, R.; Stoltz, D.; Popa, I.; Balmes, O.; Resta, A.; Wermeille, D.; Felici, R.; Ferrer, S.; Frenken, J. W. M., The role of steps in surface catalysis and reaction oscillations. *Nat Chem* **2010,** *2* (9), 730-734.

10. Greiner, M. T.; Jones, T. E.; Klyushin, A.; Knop-Gericke, A.; Schlogl, R., Ethylene Epoxidation at the Phase Transition of Copper Oxides. *J Am Chem Soc* **2017,** *139* (34), 11825-11832.

11. Imbihl, R.; Ertl, G., Oscillatory Kinetics in Heterogeneous Catalysis. *Chem Rev* **1995,** *95* (3), 697-733.

12. Ek, M.; Ramasse, Q. M.; Arnarson, L.; Moses, P. G.; Helveg, S., Visualizing atomic-scale redox dynamics in vanadium oxide-based catalysts. *Nat Commun* **2017,** *8*.

13. Huang, T. J.; Tsai, D. H., CO oxidation behavior of copper and copper oxides. *Catal Lett* **2003,** *87* (3-4), 173-178.

14. Over, H.; Kim, Y. D.; Seitsonen, A. P.; Wendt, S.; Lundgren, E.; Schmid, M.; Varga, P.; Morgante, A.; Ertl, G., Atomic-scale structure and catalytic reactivity of the RuO2(110) surface. *Science* **2000,** *287* (5457), 1474-1476.

15. Zambelli, T.; Wintterlin, J.; Trost, J.; Ertl, G., Identification of the "active sites" of a surface-catalyzed reaction. *Science* **1996,** *273* (5282), 1688-1690.

16. Schlogl, R., Heterogeneous Catalysis. *Angew Chem Int Edit* **2015,** *54* (11), 3465-3520.

17. Ammon, C.; Bayer, A.; Held, G.; Richter, B.; Schmidt, T.; Steinruck, H. P., Dissociation and oxidation of methanol on Cu(110). *Surf Sci* **2002,** *507*, 845-850.

18. Pradhan, S.; Reddy, A. S.; Devi, R. N.; Chilukuri, S., Copper-based catalysts for water gas shift reaction: Influence of support on their catalytic activity. *Catal Today* **2009,** *141* (1-2), 72-76.

19. Mistry, H.; Varela, A. S.; Bonifacio, C. S.; Zegkinoglou, I.; Sinev, I.; Choi, Y. W.; Kisslinger, K.; Stach, E. A.; Yang, J. C.; Strasser, P.; Cuenya, B. R., Highly selective plasma-activated copper catalysts for carbon dioxide reduction to ethylene (vol 7, 12123, 2016). *Nat Commun* **2016,** *7*.

20. Lunkenbein, T.; Schumann, J.; Behrens, M.; Schlogl, R.; Willinger, M. G., Formation of a ZnO Overlayer in Industrial Cu/ZnO/Al2O3 Catalysts Induced by Strong Metal-Support Interactions. *Angew Chem Int Edit* **2015,** *54* (15), 4544-4548.

21. Choudhury, F. K.; Rivero, R. M.; Blumwald, E.; Mittler, R., Reactive oxygen species, abiotic stress and stress combination. *Plant J* **2017,** *90* (5), 856-867.

22. Seiler, H., Secondary-Electron Emission in the Scanning Electron-Microscope. *J Appl Phys* **1983,** *54* (11), R1-R18.

23. Knop-Gericke, A.; Kleimenov, E.; Havecker, M.; Blume, R.; Teschner, D.; Zafeiratos, S.; Schlogl, R.; Bukhtiyarov, V. I.; Kaichev, V. V.; Prosvirin, I. P.; Nizovskii, A. I.; Bluhm, H.; Barinov, A.; Dudin, P.; Kiskinova, M., X-Ray Photoelectron Spectroscopy for Investigation of Heterogeneous Catalytic Processes. *Adv Catal* **2009,** *52*, 213-272.

24. Sezen, H.; Al-Hada, M.; Amati, M.; Gregoratti, L., In situ chemical and morphological characterization of copper under near ambient reduction and oxidation conditions. *Surface and Interface Analysis* **2017**.

25. Schmidtw.Rd; Martinez.M, Growth and Microstructural Control of Single-Crystal Cuprous-Oxide Cu2o. *J Cryst Growth* **1974,** *23* (2), 113-120.

26. DeNardis, D.; Rosales-Yeomans, D.; Borucki, L.; Philipossian, A., Studying the effect of temperature on the copper oxidation process using hydrogen peroxide for use in multi-step chemical mechanical planarization models. *Thin Solid Films* **2010,** *518* (14), 3903-3909.

27. Wan, Y.; Wang, X. M.; Sun, H.; Li, Y. B.; Zhang, K.; Wu, Y. H., Corrosion Behavior of Copper at Elevated Temperature. *Int J Electrochem Sc* **2012,** *7* (9), 7902-7914.

28. Yang, J. C.; Evan, D.; Tropia, L., From nucleation to coalescence of Cu2O islands during in situ oxidation of Cu(001). *Appl Phys Lett* **2002,** *81* (2), 241-243.

29. Zou, L. F.; Li, J.; Zakharov, D.; Stach, E. A.; Zhou, G. W., In situ atomic-scale imaging of the metal/oxide interfacial transformation. *Nat Commun* **2017,** *8*.

30. LaGrow, A. P.; Ward, M. R.; Lloyd, D. C.; Gai, P. L.; Boyes, E. D., Visualizing the Cu/Cu2O Interface Transition in Nanoparticles with Environmental Scanning Transmission Electron Microscopy. *J Am Chem Soc* **2017,** *139* (1), 179-185.

31. Milne, R. H.; Howie, A., Electron-Microscopy of Copper Oxidation. *Philos Mag A* **1984,** *49* (5), 665-682.

32. Greiner, M. T.; Jones, T. E.; Johnson, B. E.; Rocha, T. C. R.; Wang, Z. J.; Armbruster, M.; Willinger, M.; Knop-Gericke, A.; Schlogl, R., The oxidation of copper catalysts during ethylene epoxidation. *Physical Chemistry Chemical Physics* **2015,** *17* (38), 25073-25089.

33. Kolmakovl, A.; Gregoratti, L.; Kiskinova, M.; Gunther, S., Recent Approaches for Bridging the Pressure Gap in Photoelectron Microspectroscopy. *Top Catal* **2016,** *59* (5-7), 448-468.

34. Ho, J. H.; Vook, R. W., (111)Cu2o Growth Modes on (111)Cu Surfaces. *J Cryst Growth* **1978,** *44* (5), 561-569.

35. Burtovyy, R.; Utzig, E.; Tkacz, M., Studies of the thermal decomposition of copper hydride. *Thermochim Acta* **2000,** *363* (1-2), 157-163.

36. Yasumori, I.; Momma, N.; Kiyomiya, M., Mechanism of Hydrogen Adsorption and Hydrogen-Deuterium Equilibration on Copper Surface. *Jpn J Appl Phys* **1974**, 485-488.

37. Coulman, D.; Wintterlin, J.; Barth, J. V.; Ertl, G.; Behm, R. J., An Stm Investigation of the Cu(110)-C(6x2)O System. *Surf Sci* **1990,** *240* (1-3), 151-162.

38. Jensen, F.; Besenbacher, F.; Stensgaard, I., 2 New Oxygen Induced Reconstructions on Cu(111). *Surf Sci* **1992,** *269*, 400-404.

39. Lian, X.; Xiao, P. H.; Liu, R. L.; Henkelman, G., Calculations of Oxygen Adsorption-Induced Surface Reconstruction and Oxide Formation on Cu(100). *Chem Mater* **2017,** *29* (4), 1472-1484.

40. Lahtonen, K.; Hirsimaki, M.; Lampimaki, M.; Valden, M., Oxygen adsorption-induced nanostructures and island formation on Cu{100}: Bridging the gap between the formation of surface confined oxygen chemisorption layer and oxide formation. *J Chem Phys* **2008,** *129* (12).

41. Duan, X.; Warschkow, O.; Soon, A.; Delley, B.; Stampfl, C., Density functional study of oxygen on Cu(100) and Cu(110) surfaces. *Phys Rev B* **2010,** *81* (7).

42. Lampimaki, M.; Lahtonen, K.; Hirsimaki, M.; Valden, M., Nanoscale oxidation of Cu(100): Oxide morphology and surface reactivity. *J Chem Phys* **2007,** *126* (3).

2.8 Supplementary information

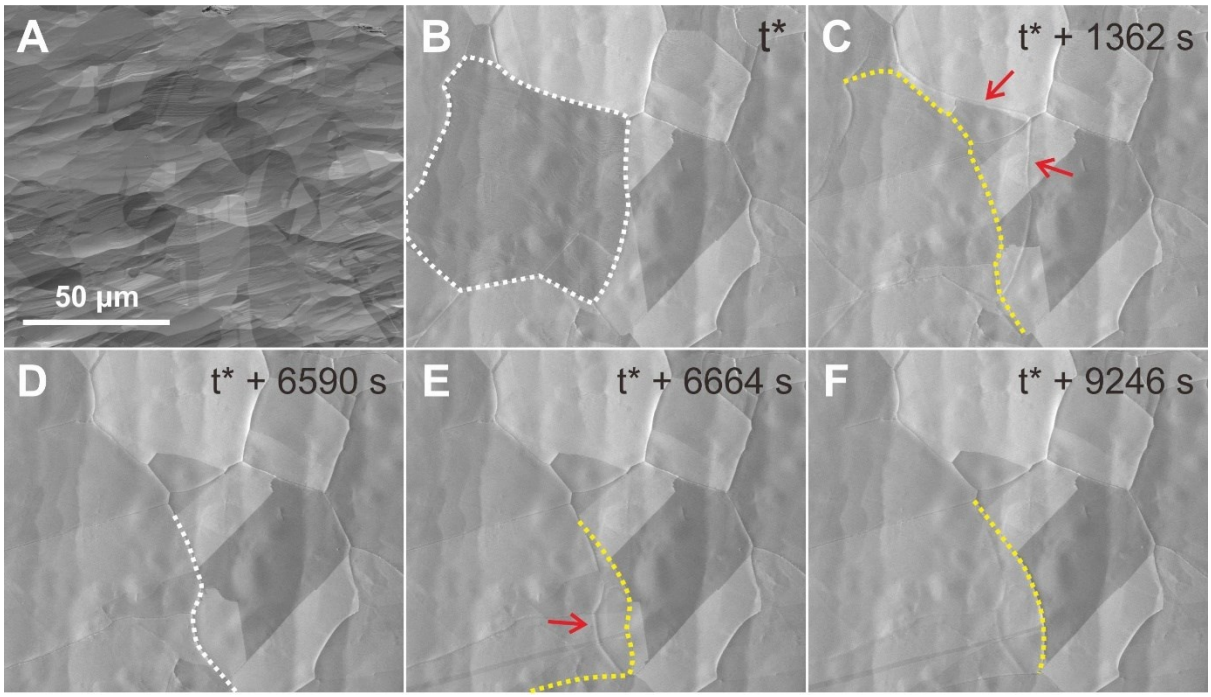

Figure S2.1 A) shows the morphology of copper foil before annealing. In B-F), a sequence of modification images shows grain growth *and migration at 700 °C during exposure to 21 Pa hydrogen. White dot lines highlight the grain boundaries maintained during the annealing process, yellow dot lines for the emerging boundaries. t* indicated the annealing process until obvious grain boundaries transformation can be observed. Different grain reveals different contrast due to electron channeling effect.*

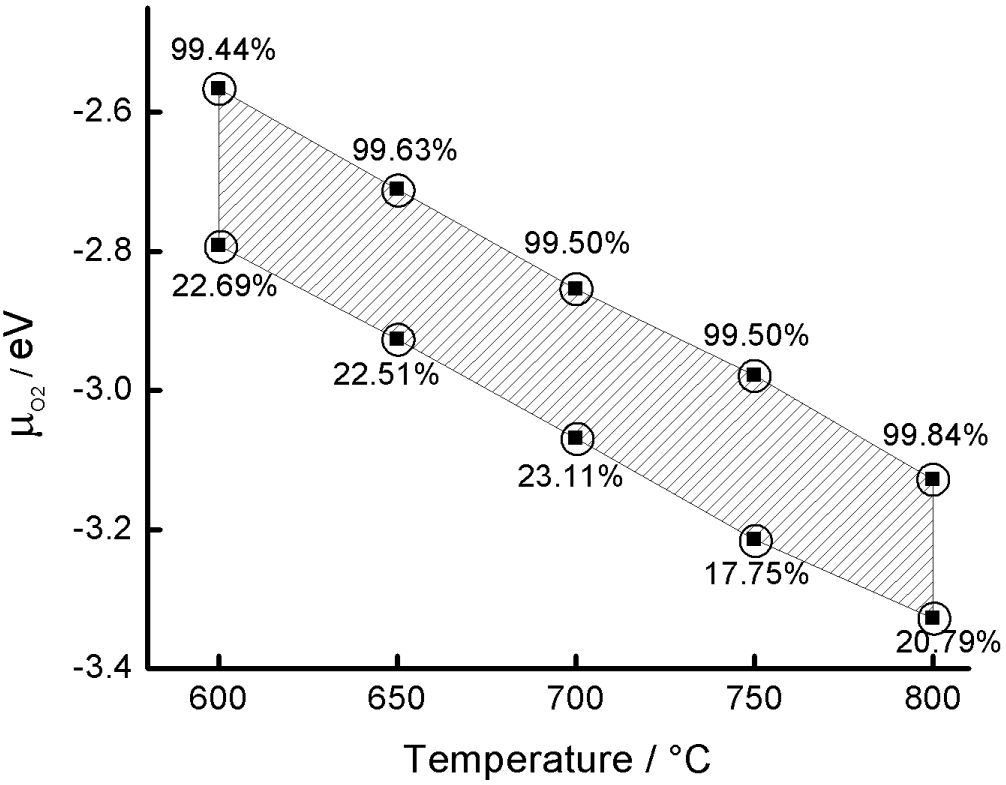

Figure S2.2 Circles show Cu_2O coverage ratios at the boundary transited from reduced region A to tri-stable region B and finally converted to Cu_2O.

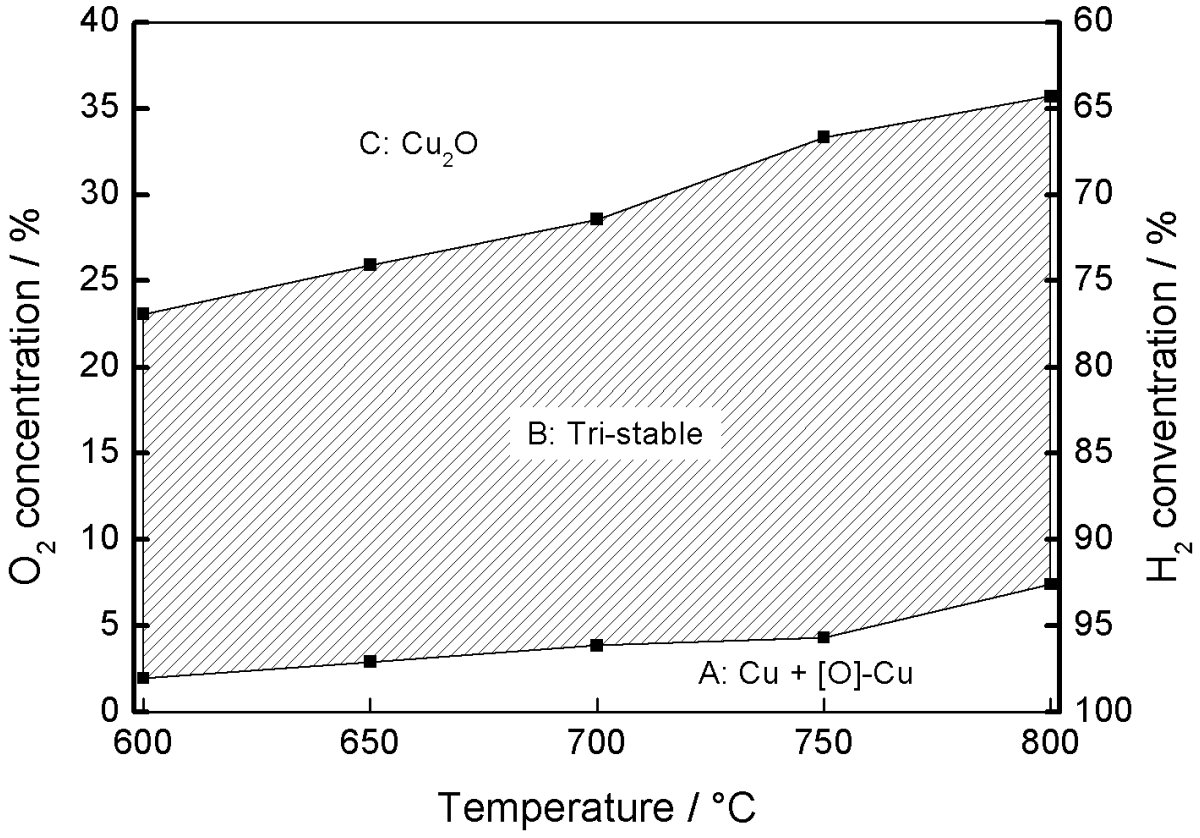

Figure S2.3 exhibits the Cu_2O coverage extracted form Videos 2.2-2.26. For each Cu_2O coverage correlated O_2 chemical potential are available in Table S2.2.

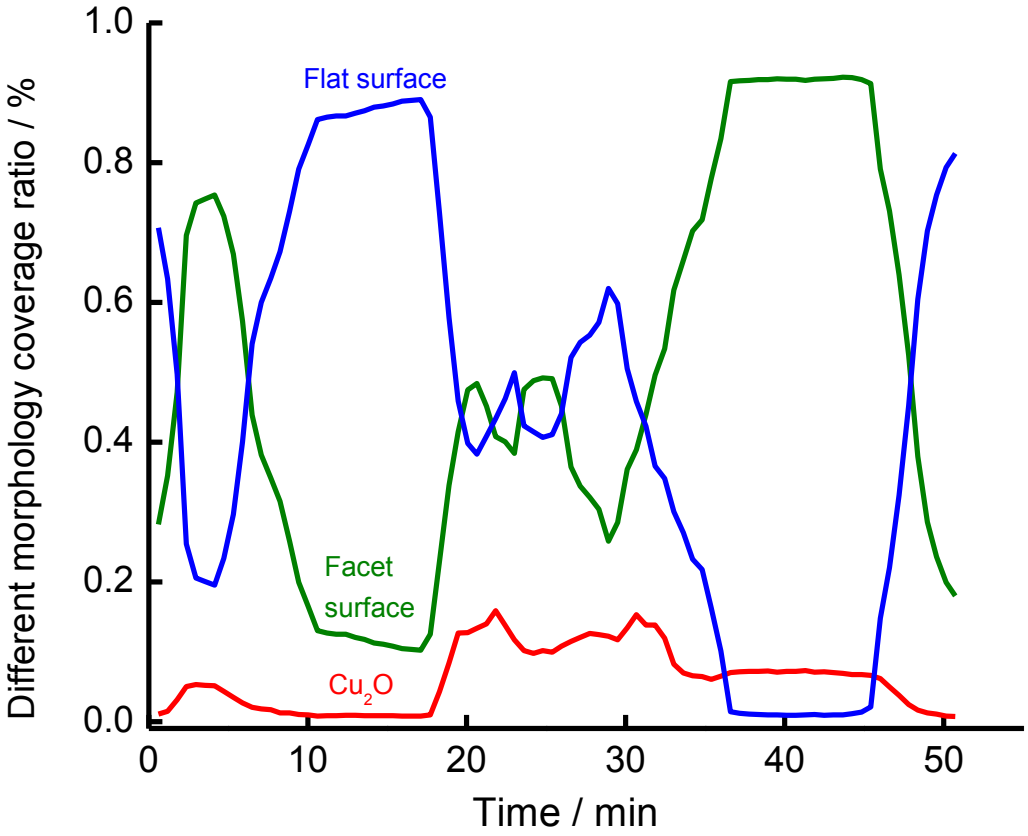

Figure S2.4 exhibits the different morphologies coverage ratio change with time, which are extracted from Video S2.28, including Cu_2O, facet surface and flat surface.

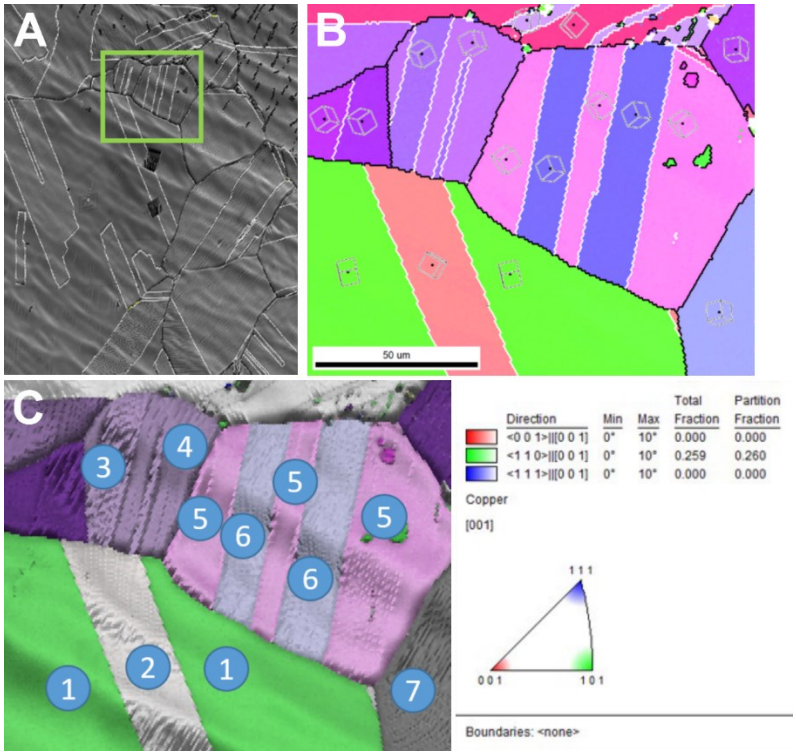

Figure S2.5 A) is an overview of the facet and flat surface frozen after reaction, where two FIB cuts were lifted out of the surface. Region of interest (ROI), marked in green square, is analyzed by electron backscattering diffraction (EBSD). B) EBSD orientation map of ROI. Twin boundaries (while lines), sigma 3, are appeared, which is 60° rotation around <111>. Each set of twins is separated by a grain boundaries (black). C) shows the grain orientation: grain①: ~7° misorientation from <110>; grain②: ~7° <310>; grain③: ~5° <211>; grain④: ~5° <211>; grain⑤: ~6° <311>; grain⑥: ~13° <111>; grain⑦: ~3° <123>.

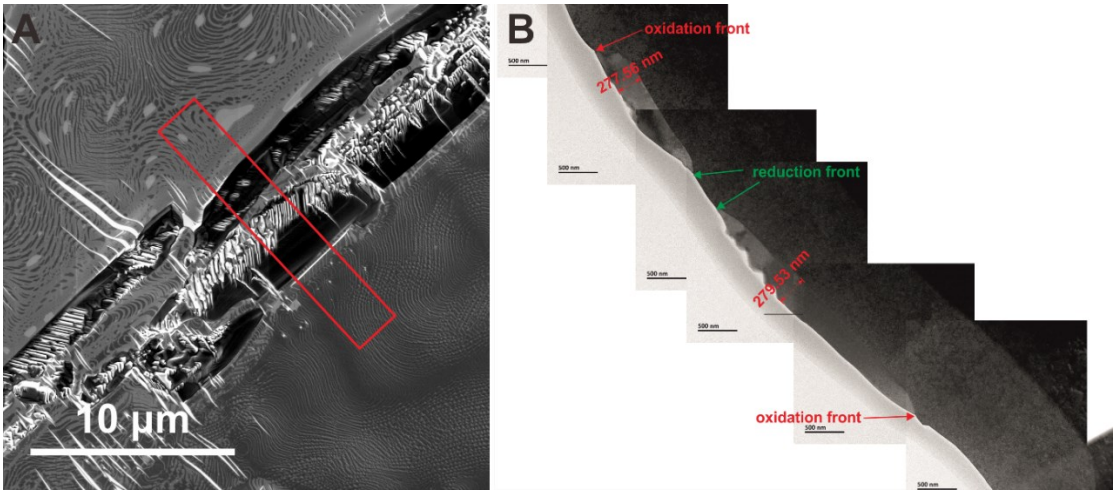

Figure S2.6 A) is the quenched morphology after redox dynamics on Cu (110). A thin lamella is cut out a defined location (marked by red rectangular) from copper foil, tinned and then analyzed with a transmission electron microscope, in Figure B).

Table S2.1 μ_O (T, P°) in the temperature range of the interest to our study. The standard pressure (P^0) is 0.1 MPa.

Temperature	Temperature / K	μ_{O2} (T, P°) / eV	μ_{H2} (T, P°) / eV
600	873.15	-0.94244	-0.73704
650	923.15	-0.99994	-0.78272
700	973.15	-1.05744	-0.88911
750	1023.15	-1.11494	-0.93479
800	1073.15	-1.17244	-0.98047

Oxygen chemical potential (μ_{O2}) at different temperatures and pressures are calculated via equation,

$$\mu\,(T, P) = 2\,(T, P°) + kT \ln (P/P^0)$$

k is Boltzmann constant, 8.617 x 10^{-5} eV/K.

Table S2.2 shows the Cu_2O coverage and chemical potential at different oxygen concentrations.

Temperature / °C	Cu_2O coverage / %	μ_{O2} / eV	Oxygen concentration / %
600	0.00	-2.80785	1.57
600	22.69	-2.79135	1.96
600	70.37	-2.59976	16.67
600	99.74	-2.58276	20.00
600	99.44	-2.56585	23.08
650	0.00	-2.96095	1.96
650	22.51	-2.92677	2.91
650	39.08	-2.82623	9.09
650	99.63	-2.71058	25.93
650	81.33	-2.6983	28.57
700	0.00	-3.09481	3.38
700	23.12	-3.06865	3.85
700	97.38	-3.01868	6.54
700	99.44	-2.87092	25.93
700	99.50	-2.85429	28.57
750	0.00	-3.22696	3.38
750	17.76	-3.23831	4.31
750	34.49	-3.21428	4.76
750	98.40	-3.0974	13.04
750	99.46	-2.97817	33.33
800	0.00	-3.35495	5.66
800	20.78	-3.32722	7.41
800	95.87	-3.18743	23.08
800	99.48	-3.12795	35.71
800	99.84	-3.11213	50.00

3 Direct observation of chemical potential induced dynamics of platinum by *in situ* scanning electron microscopy

3.1 Abstract

Understanding how surface restructuring influences catalyst activity is an essential but challenging step toward tailoring and designing high-performance catalysts. Platinum, being an important catalyst in several applications, has been extensively studied by the scientific community. However, structure-reactivity correlations are generally not straightforward, as platinum can reconstruct when in contact with reactive atmospheres, and it is non-trivial to determine which surfaces are present under reaction conditions, let alone determine which of the surfaces or defects are responsible for catalytic activity. In the present study, hydrogen and oxygen are used as prototype reductants and oxidants to examine how the gas phase influences the platinum morphology, and how changing chemical potential of the gas phase leads to catalytic activity variations. Environmental scanning electron microscope is employed to record the morphological dynamics that occur under reaction conditions, while on-line mass spectrometry is used to track corresponding changes in catalyst activity.

3.2 Introduction

Surfaces are extremely important in heterogeneous catalysis. They influence chemisorption, diffusion, reaction and desorption processes involved in the catalytic cycle. All these key steps critically depend on the surface composition and structure of the catalytic particle on the atomic scale.[1-2] A catalyst's surface can be chemically altered by the adsorption of molecules, and thereby a surface can undergo a restructuring when exposed to a mixture of gaseous adsorbates. The adsorbate-induced restructuring can greatly change the catalyst's activity during a given reaction.[3] Therefore, it is important to understand the morphological and structural changes that occur to catalysts under reaction conditions, and it could be essential for understanding how to further enhance a catalyst's activity.

Platinum serves as a fundamental system for surface science and catalysis research, due to its ability to perform both oxidizing and reducing reactions without changing its metallic character. It has been extensively used in various industrially important reactions, such as hydrocarbon oxidation and dehydrogenation, carbon monoxide (CO) reduction in automotive exhaust gases,[4-5] fuel cells,[6] ammonia oxidation,[7] and reforming in petroleum industry.[6] The surface of a Pt catalyst is prone to reconstruction under reaction conditions, and the surface reconstruction can influence the catalytic activity. It was found that Pt (110) can reconstruct from a (1 × 1) structure in CO-rich conditions to a (1 × 2) structure in CO-lean conditions during CO oxidation.[8] The surface transition is accompanied by CO oxidation-rate oscillations.[9-11] Other examples of surface restructuring include faceting during H_2S decomposition[12], as well as stepped[7], roof[13] and cauliflower[14] structures in ammonia oxidation. The adsorption-induced surface reconstructions can change the exposed crystal face, which would generally alter the sticking coefficients of the exposed surface, thereby altering catalytic activity,[12-13, 15-16]

The morphological changes on Pt surfaces during NH_3 oxidation have been studied by scanning electron microscope (SEM), and transmission electron microscope (TEM) before and after reaction treatments at various gas compositions and temperatures.[17,13] Depending on temperature, pressure, and catalyst composition, the surfaces of Pt-based catalysts reconstruct into rows of facets and pits, and later on into bulky structures resembling the shape of a square. Those observations suggest that surface roughening improves the catalytic activity in ammonia oxidation. This process is called Platinum ‘activation’ and is supposed to result from increased surface area during roughing.[13] However, how the surface roughing influences the catalytic activity, and what the ideal surface looks like are still matters of debate. In fact, surface roughening is a dynamic process, so the static images recorded after reaction can hardly provide a satisfactory answer to the above questions.

Platinum exhibits a similar morphology when exposed to a mixture of hydrogen and oxygen. Here we employed environmental scanning electron microscopy (ESEM), in tandem with a quadrupole mass spectrometer (QMS) to monitor the platinum surface roughening under *in situ* conditions. We studied the morphological changes of Pt that occur when heated in a mixture of oxidizing and reducing agent, using hydrogen oxidation as model reactants, due to hydrogen's moderate reducing and oxygen

oxidizing potentials. We examined the material under two different conditions: First, where the total pressure was kept constant, while oxygen chemical potential and hydrogen chemical potential were simultaneously changed (Figure 3.1A). The second set of conditions were to keep oxygen chemical potential constant and vary hydrogen chemical potential. In order to hold the total pressure constant, an inert balancing gas (Ar) was added (Figure 3.1B). Furthermore, the dynamics that occur under these conditions are at suitable length and time scales to be observed by ESEM, while the catalytic cycle is much faster.[18] This comparative study provides new insights on the morphological dynamics that can occur in reactive atmospheres and how they influence the reactivity.

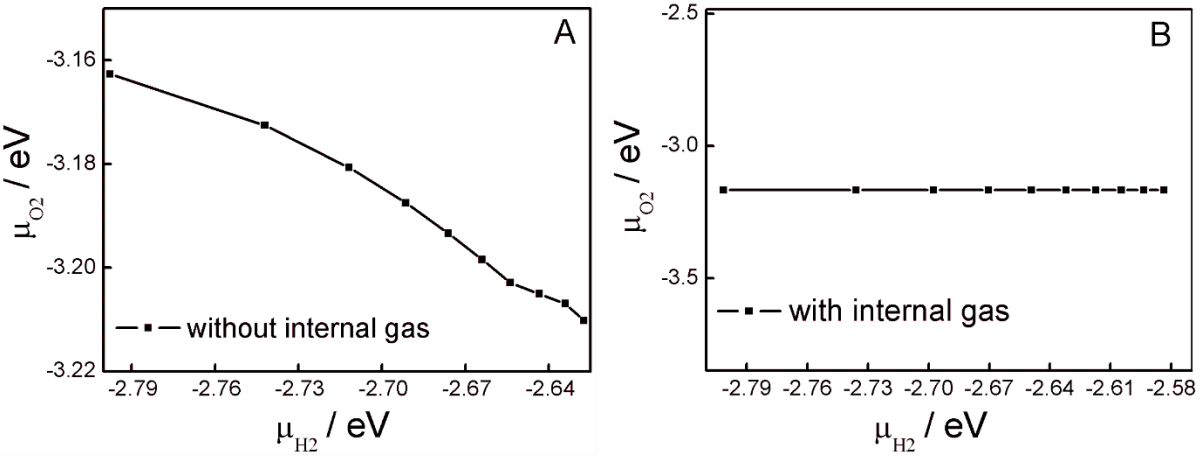

Figure 3.1 Experiments performed under two conditions: A) the gas composition is only hydrogen and oxygen, without internal gas; B) Argon as used as internal gas to keep the total pressure constant.

3.3 Experiment section

3.3.1 Sample preparation

Polycrystalline Platinum foils with lateral dimensions of 5×5 mm^2 and thickness of 0.25 mm (99.99% from Alpha Aesar) were used as samples. Prior to all experiments, samples were annealed at 800 °C under a hydrogen flow of 10 ml/min and an oxygen flow 1 ml/min, at a total pressure of 20 Pa for 10 hours to remove the carbon contamination on the surface, see the supplementary Video S3.1. Subsequently, the foils were reduced in pure H_2 at a constant gas flow rate of 10 ml/min at 800 °C for 3 hours.

3.3.2 *In situ* scanning electron microscopy

In situ experiments were performed inside a commercial ESEM chamber (FEI Quantum 200). The instrument was modified and equipped with a home-built heating stage, gas supply system (mass flow controllers from Bronkhorst) and a quadrupole mass spectrometer (QMS) to analyze the chamber atmosphere. The base pressure was ca. 2×10^{-5} Pa, with a residual gas composition mostly comprising water, nitrogen and oxygen. After sample loading, the chamber was purged with N_2 and pumped again to 10^{-3} Pa successively to remove residual gas. Experiments were conducted under low vacuum conditions (30 ~ 60 Pa). The temperature was measured with a K-type thermocouple that was spot-welded onto the foil, and simultaneously served to ground the sample.

During the experiments, the microscope was operated with an acceleration voltage of 7.5 kV. ESEM images were recorded by a large field detector with 35.40 s per frame. No influence of the electron beam on the surface was observed, as the imaged regions and their respective surroundings showed similar behavior at several magnifications. During the catalytic experiments at 800 °C, 700 °C and 600 °C, oxygen mass flow was maintained at 5 ml/min and hydrogen flow was stepwise decreased from 10 to 1 ml/min, then increased back to 10 ml/min, in the range of 30 Pa to 60 Pa. As a comparison, similar experiments at constant pressure at 800 °C were also performed. Argon, employed as an inert diluent, was used to compensate the H_2 flow rate to keep to total mass flow at 16 ml/min and pressure in the range of 100 Pa. Details are available in Table 3.1 The dwell time at each step was 30 minutes, allowing ca. 40 images to be recorded at each temperature step. In order to quantify the rate of change, we define the morphological variation rate *k* as:

$$k = D / t \tag{3-1}$$

Where D denotes the average image contrast differences, and t is recording time per image.

Table 3.1 H_2 chemical potential changes with hydrogen mass flow decrease under two different conditions. A) the total pressure varied from 60 to 30 Pa without internal gas; B) With internal gas, the total pressure can be maintained at 100 Pa. The calculation is similar to chapter 2.

A) Without internal gas							
H_2 mass flow	H_2 concentration	H_2 partial pressure	H_2 chemical potential	O_2 mass flow	O_2 concentration	O_2 partial pressure	O_2 chemical potential
(ml/min)	(%)	(Pa)	(eV)	(ml/min)	(%)	(Pa)	(eV)
10	66.67	39.33	-2.627	5	33.33	19.67	-3.210
9	64.29	36.64	-2.634	5	35.71	20.36	-3.207
8	61.54	33.23	-2.643	5	38.46	20.77	-3.205
7	58.33	29.75	-2.654	5	41.67	21.25	-3.203
6	54.55	26.73	-2.664	5	45.45	22.27	-3.198
5	50	23.50	-2.676	5	50.00	23.50	-3.193
4	44.44	20.00	-2.691	5	55.56	25.00	-3.188
3	37.5	16.13	-2.712	5	62.50	26.88	-3.181
2	28.57	11.71	-2.742	5	71.43	29.29	-3.173
1	16.67	6.50	-2.798	5	83.33	32.50	-3.163

B) Without internal gas								
H_2 mass flow	H_2 concentration	H_2 partial pressure	H_2 chemical potential	Ar mass flow	O_2 mass flow	O_2 concentration	O_2 partial pressure	O_2 chemical potential
(ml/min)	(%)	(Pa)	(eV)	(ml/min)	(ml/min)	(%)	(Pa)	(eV)
10	66.67	39.33	-2.584	10	5	31.25	31.25	-3.1667
9	64.29	36.64	-2.594	9	5	31.25	31.25	-3.1667
8	61.54	33.23	-2.605	8	5	31.25	31.25	-3.1667
7	58.33	29.75	-2.617	7	5	31.25	31.25	-3.1667
6	54.55	26.73	-2.632	6	5	31.25	31.25	-3.1667
5	50	23.5	-2.649	5	5	31.25	31.25	-3.1667
4	44.44	20	-2.670	4	5	31.25	31.25	-3.1667
3	37.5	16.13	-2.698	3	5	31.25	31.25	-3.1667
2	28.57	11.71	-2.736	2	5	31.25	31.25	-3.1667
1	16.67	6.5	-2.802	1	5	31.25	31.25	-3.1667

3.3.3 *In situ* mass spectrometry

To elucidate the relationship between the observed surface dynamics and catalytic activities, a QMS was used to monitor H_2 conversion. H_2O was not chosen as the

product to monitor the catalytic activity because the main component of the residual gas in the ESEM chamber was water, resulting in a rather large background H_2O signal and inaccurate H_2O detection. Therefore, the hydrogen conversion rate was used to characterize the platinum catalytic activity. Comparative experiments under the same conditions without heating were also measured, and used as a background signal according to:

$$\Delta I(H_2)_{(consumption)} = I(H_2)_{(control)} - I(H_2)_{(reaction)} \quad (3\text{-}2)$$

$$H_2 \text{ conversion} = (\Delta I(H_2)_{(consumption)} \div I(H_2)_{(control)}) \times 100\% \quad (3\text{-}3)$$

Where *I* denotes the ion current of the mass spectrometer.

3.3.4 Near-ambient pressure X-ray photoemission spectroscopy

Near-ambient pressure X-ray photoemission spectroscopy (NAP-XPS) measurements were carried out at the Innovative Station for *In situ* Spectroscopy (ISISS) beamline at the Helmholz-Zentrum Berlin (HZB) synchrotron light source (BESSY II). The set-up is equipped with a differentially-pumped electrostatic lens and analyzer system attached to a reaction cell. Details of this equipment are available elsewhere.[19] During *in situ* experiments, reaction gases (Westfalen AG, purities, H_2 and O_2 6.0N) were continuously fed into the reaction cell via mass-flow controllers. The pressure in the chamber was maintained at 20 Pa. The sample was heated from the back side using an infrared laser, and the temperature was measured with a type K thermocouple that was mechanically clamped onto the surface of the sample.

3.4 Results

3.4.1 Morphology studies under changing oxygen and hydrogen chemical potentials

Initially, the hydrogen chemical potential was varied from -2.63 eV to -2.80 eV, in the absence of an inert dilution gas, requiring the oxygen chemical potential to be adjusted to the range of -3.21 eV to -3.16 eV in order to keep constant pressure. Under these conditions, the optimal operating temperature, the morphology variation rate and the reversibility of reconstructions were examined.

3.4.1.1 Catalytic activity at various temperatures

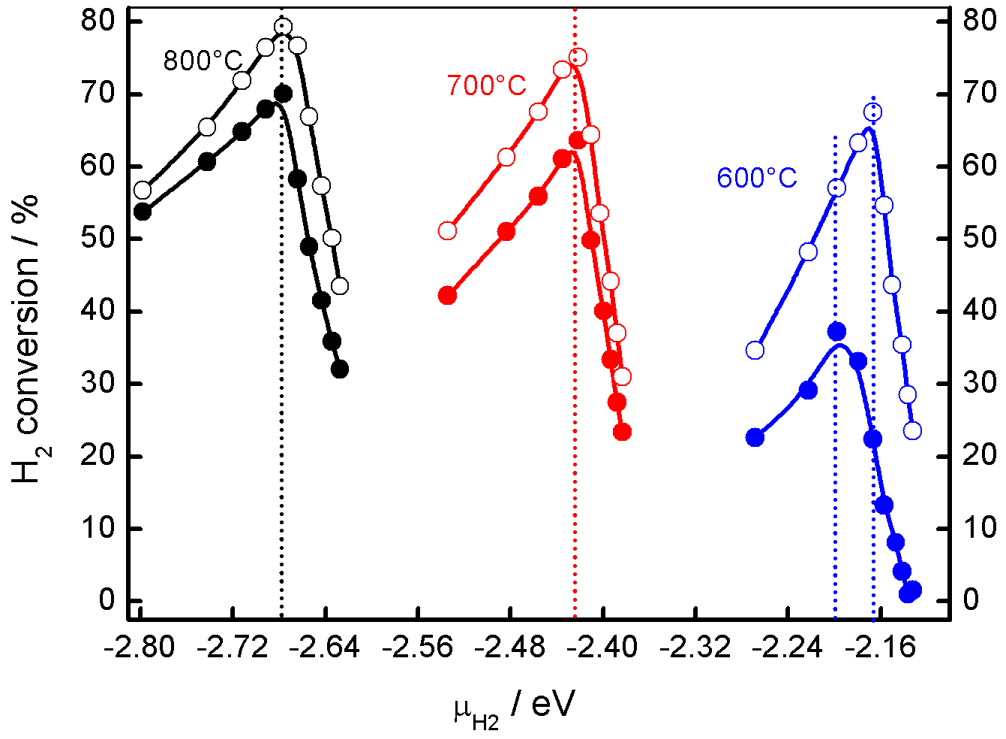

Figure 3.2 H_2 conversion at different temperatures (600 °C, 700 °C, 800 °C) for various H_2 chemical potential. Lines with solid circles indicate H_2 conversion changes with decreasing H_2 chemical potential and lines with open circles show the H_2 conversion variations with increasing H_2 chemical potential at each temperature.

Reduced Pt foil was exposed to hydrogen and oxygen mixtures at various temperatures, ranging from 600 to 800 °C, in a total pressure ranging from 30 to 60 Pa. The H_2 chemical potential was cycled between -2.63 eV to -2.80 eV which corresponds to a H_2 mass flow change between 10 and 1 ml/min to tune the O_2 and H_2 ratio to examine the resulting surface morphological changes. The hydrogen conversion at 600 °C, 700 °C, and 800 °C are shown in Figure 3.2. In general, the hydrogen conversion depends on the H_2 chemical potential in a volcano-type shape, with maxima of conversion observed H_2 chemical potential -2.68 eV at 800 °C and -2.42 eV at 700 °C. Here the H_2 conversion is independent of initial state. The maximum is different at 600 °C, the H_2 conversion reached maximum at μ_{H2} = -2.20 eV with decreasing regime, while it peaks at H_2 increasing regime at -2.17 eV.

While total conversion depends on the direction of the H_2 chemical potential. The H_2 chemical potential for which the highest activity was observed was independent of cycles at 800 °C and 700 °C. At these temperatures, the maximum in conversion was invariably found to be -2.68 eV at 800 °C and -2.42 eV at 700 °C. The hysteresis at lower temperature (600 °C) can be assigned to initial activation of the Pt surface. Below we provide further details of the results for the reaction temperature of 800 °C, as this is where the activity was the greatest.

From considerations of the overall reaction stoichiometry of $H_2 + ½O_2 \rightarrow H_2O$, one might expect the highest conversion to be at H_2 chemical potential -2.63 eV and O_2 -3.21 eV (calculated from partial pressure under conditions without internal gas), which corresponds to H_2:O_2 ratio of 2:1. Hypothetically, if no catalyst were involved, the highest activity would be observed for the stoichiometric ratio. However, a stoichiometric ratio in the gas phase does not necessarily imply a stoichiometric ratio of reactants adsorbed to the surface. The adsorbate populations also depend on the adsorption/desorption rate of the respective reactants. The fact that the rate maximum was observed at H_2 chemical potential -2.68 eV (5 ml/min H_2 and 5 ml/min O_2) for an H_2:O_2 ratio of 1:1 is likely a result of the lower activation barrier for H_2 on Pt compared to O_2 on Pt. This point will be discussed further below.

3.4.1.2 Qualitative ESEM observation of Pt foil in H_2 and O_2 at 800 °C

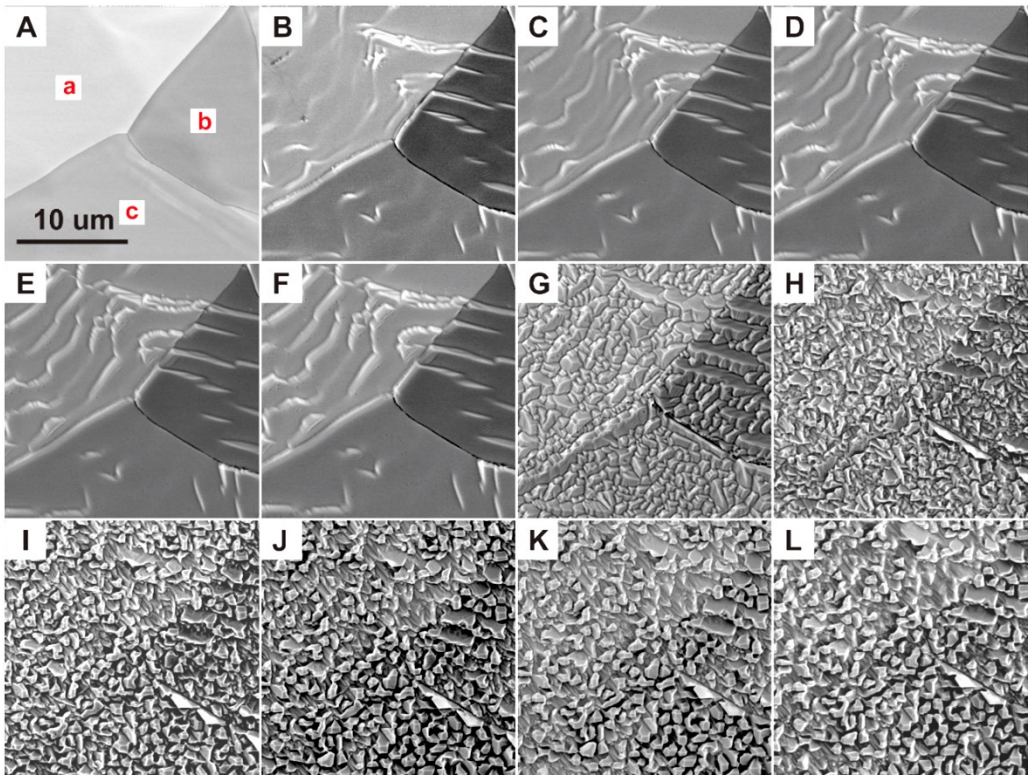

Figure 3.3 A) is the freshly reduced polycrystalline foil; B – K) are platinum surface morphological evolutions when H_2 chemical potential is decreased from -2.63 to -2.80 eV at 800 °C, corresponding to a decrease of the H_2 mass flow from 10 to 1 ml/min, L) at H_2 0 ml/min. The O_2 mass flow was kept constant at 5 ml/min.

Prior to the reaction, the sample has been annealed to 800 °C in pure H_2. This treatment resulted in a smooth surface on the micrometer scale (Figure 3.3A). The three grains seen in Figure 3.3A exhibit different contrasts due to the electron channeling effect. Subsequent introduction of 5 ml/min O_2 (H_2 chemical potential at -2.62 eV) into the chamber leads to an immediate surface reconstruction, shown in Figure 3.3B. This reconstruction is grain dependent. For instance, grains a and b form curved, faceted structures, while grain c forms relatively straight, parallel striations. Additionally, in the H_2 chemical potential regime of -2.63 to -2.66 eV (H_2 flow 9 to 6 ml/min), the morphological stability of each grain varies. For instance, on grains a and b, the parallel facets become more visible, due to what seems to be an increase in the facets' step heights. Meanwhile grain c exhibits almost no apparent change. Similar reaction-induced reconstructions of the Pt surface have been observed for NH_3 oxidation reactions.[13] As opposed to previous literature reports, the

surface roughening during hydrogen oxidation initiates over the entire grain area, rather than from the grain boundary. This observation could be the result of the different gas atmospheres or pre-treatments employed here.

Decreasing the H_2 chemical potential to -2.68 eV (H_2 mass flow at 5 ml/min), (Figure 3.3G) results in the formation of protrusions on the surface. These protrusions supersede the parallel faceting and dominate the overall surface morphology. This phenomenon is grain independent and covers the entire surface within 30 minutes. During this process the grain boundaries are not clearly visible. The three-dimensional (3D) protrusions exhibit well-defined edges and transform the surface into islands with 'roof'-shaped structures, having sizes around 1µm at H_2 chemical potential of -2.70 and -2.71 eV (Figure 3.3H and 3.3I at H_2 mass flow at 4 ml/min and 3 ml/min). The formation of the roof-shaped structures is independent of the crystal orientation, and can be observed on grains a, b and c, in Figure 3.3. The grain orientations were determined post-reaction using electron back scattered diffraction (EBSD), shown in supporting information (Figure S3.1).

A further decrease of the H_2 chemical potential to -2.80 eV (at flow rate to 1 ml/min) converts the basal plane of the new structure from a roof-like structure to a square structure with sharp edges in a range of 2 ~ 5 um. High resolution images of the structures are shown in the supplementary material (Figure S3.2). The roof- and square-shaped structures were assumed to be induced by O_2. We therefore expect that these structures continue growing in the absence of H_2 which would lead to sharp and straight morphologies. However, Pt in pure oxygen leads to a smoothening of the edges of the roof- and square-shaped structures (see Video S3.2). This observation suggests that Pt surface roughening does not solely rely on the presence of either H_2 or O_2, but rather on the coexistence of both gases in a well-defined chemical potential.

3.4.1.3 Relationship between catalytic activity and morphological variation

As demonstrated above, variations of the H_2 and O_2 content induce a roughening of the Pt surface by the formation of 3D morphologies of various shapes, including corrugations, protrusions, roof- and square-shaped structures. Similar surface structures have been previously reported, such as pits[17], cauliflower[20 14], 'metal wool' structures[21 22] and bulky crystals that protrude from the surface during the NH_3

oxidation process. It has also been shown that the morphological changes are associated with an increase of the catalytic activity in the NH_3 oxidation.[13] The surface roughening process is dynamic, making it difficult to study the process by *ex situ* analysis, and to correlate the morphological changes before and after reaction with catalytic activity. Environmental SEM enables one to track morphological changes with time, and with changing hydrogen content. Such information can provide a more detailed understanding of the relationship between structural dynamics and catalytic activity. This approach makes it possible to investigate the correlation between the catalytic activity and surface morphological change rate. In the following paragraphs, we describe this correlation.

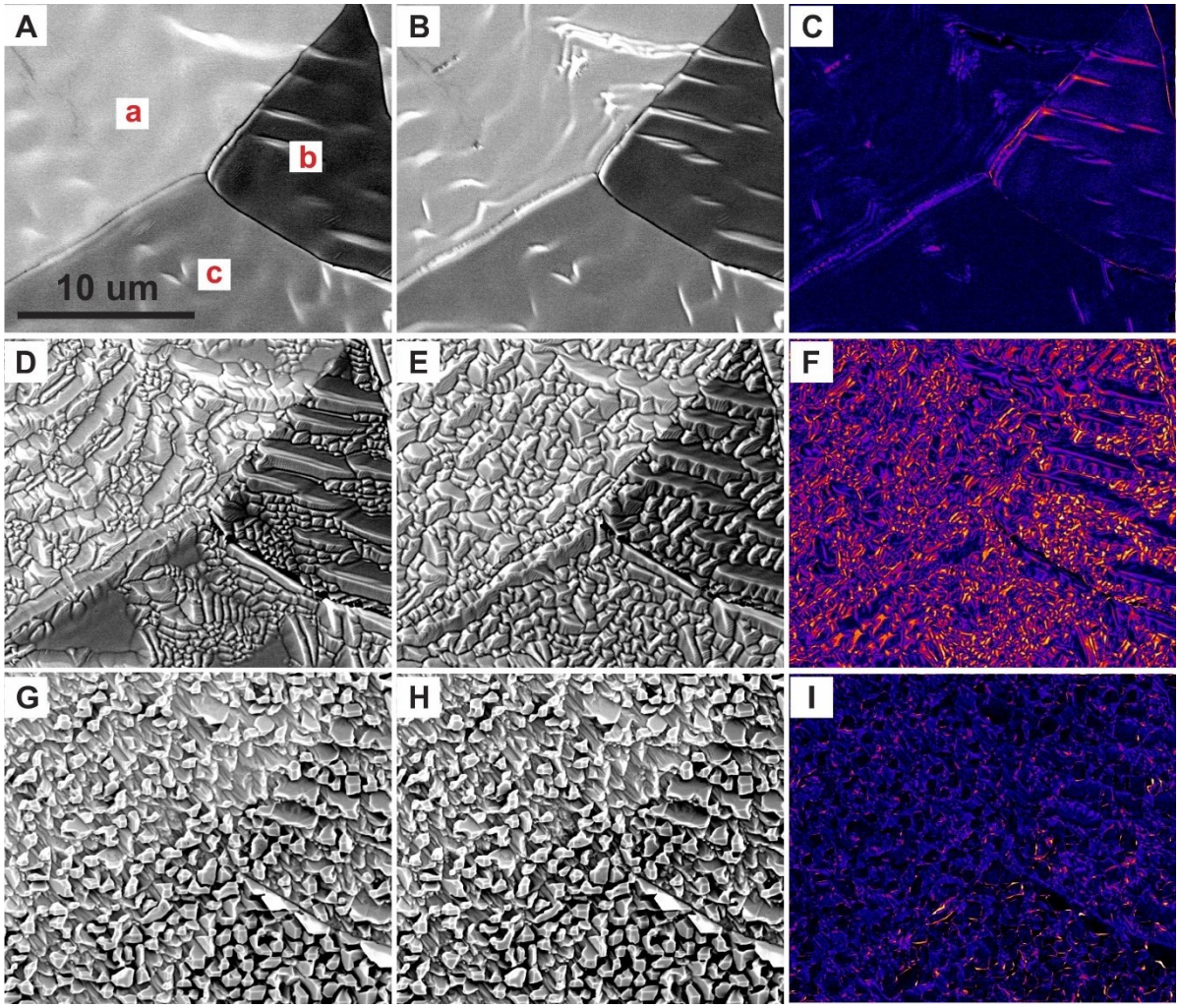

Figure 3.4 Snapshots were selected to show the platinum surface morphology evolutions in 30 mins at different H_2 chemical potential potentials -2.63 eV, -2.68 eV and -2.80 eV. A) is the surface morphology at the beginning, B) is after 30mins and C) is the difference of two morphologies at H_2 chemical potential -2.63 eV (H_2 at 10 ml/min); likewise, D – F) indicated

the morphology changes at H_2 chemical potential -2.68 eV (H_2 at 5 ml/min); G – I) at -2.80 eV (H_2 at 1 ml/min). Temperature was kept constant at 800 °C and oxygen mass flow at 5 ml/min.

As mentioned above, during the experiments, oxygen was introduced at a constant flow rate of 5 ml/min at a temperature at 800 °C, while the hydrogen flow rate was decreased in 1 ml/min steps from 10 ml/min to 0 ml/min. Each of the conditions were held for 30 minutes, while SEM images were recorded. Complete data sets at each ratio can be found in the supporting information (Videos S3.3-3.13). Figure 3.4 shows three different conditions, with H_2 chemical potential -2.63 eV (H_2 flow rate10 ml/min A-C), -2.68 eV (flow rate 5 ml/min D-F) and -2.80 eV (flow rate 1 ml/min G-I) at 800 °C. The first two columns represent different time points, while the last column represents a difference image from the images in the first two columns. Thus, the contrast in the images of the last column represents the amount of morphological change for a given time at each of the conditions shown here.

Figure 3.4A shows the surface morphology at the beginning of the conditions where 10 ml/min H_2 was flown into the chamber, at a H_2 chemical potential -2.63 eV. The surface starts off relatively flat. Some faceting is visible. Figure 3.4B shows the surface morphology after 30 minutes under these conditions. Figure 3.4C shows the grey-scale difference between panels A and B. It highlights the morphological changes that occurred during these conditions.

A decrease in the hydrogen chemical potential to -2.68 eV (5 ml/min H_2) resulted in a much rougher surface via the formation of pyramid-shaped structures. The roughening process at H_2 -2.68 eV (5 ml/min H_2) is much faster compared to $\mu(H_2)$ of -2.80 and -2.63 eV. Figure 3.4D and E show the morphologies before and after 30 minutes at H_2 -2.68 eV (5 ml/min H_2), respectively. As one can see from these images, the entire surface has been restructured, and the grain boundaries have become less distinct. The morphological changes after 30 minutes under these conditions are depicted in Figure 3.4F. This difference image shows that the degree of morphological change is much more significant than in the conditions of higher H_2 chemical potentials-2.63 eV (H_2 10 ml/min).

One might presume that the surface would continue to get rougher and more dynamic as the hydrogen flow rate decreases. However, the surface roughening

process slows down as the H_2 chemical potential is decreased from -2.70 (4 ml/min H_2) to -2.80 eV (1 ml/min H_2). At H_2 -2.80 eV (1 ml/min H_2), the surface dynamics have nearly stopped (seen in supporting Video S3.12). After 30 minutes at -2.80 eV, the surface morphological changes are minimal, as seen from the pixel intensities of Figure 3.4l. A further quantitative analysis of the morphological changes for each hydrogen mass flow condition is shown in Figure 3.5.

When considering how the higher surface area of the roughened surface should affect activity, one expects that the activity should be higher for the roughened surface. However, as Figure 3.5 shows, the H_2 conversion rate under these conditions is relatively low. Despite the higher surface area under the O_2-rich conditions, the surface populations of reactants are presumably too far dominated by O-coverage to provide optimal activity.

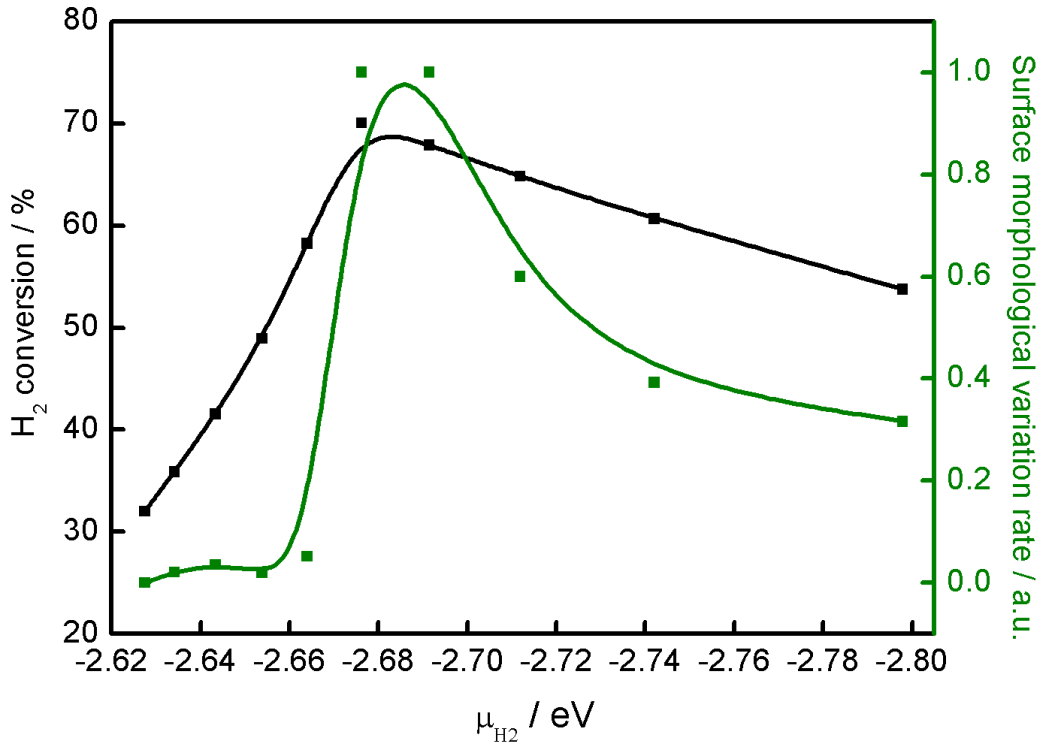

Figure 3.5 Comparison of surface morphological variation rate (green curve) and hydrogen conversion (black curve) versus H_2 chemical potentials.

Interestingly, here we see a correlation between surface morphological dynamics and activity. In order to quantify the rate of morphological change, we have summed together the pixel intensities from the difference images. This data is normalized and

plotted in Figure 3.5 (green curve) along with the measured H_2 conversion (black curve) as a function of the H_2 chemical potential.

The fastest morphological changes occur during the H_2 chemical potential transition from -2.68 eV to -2.70 eV (5 ml/min to 4 ml/min H_2), and correspond to the conditions for which H_2 consumption was the greatest. This observation demonstrates here that the surface morphological variation rate is correlated with high H_2 turnover ratios.

3.4.1.4 Relationship between catalytic activity and laser power and temperature difference variation

.

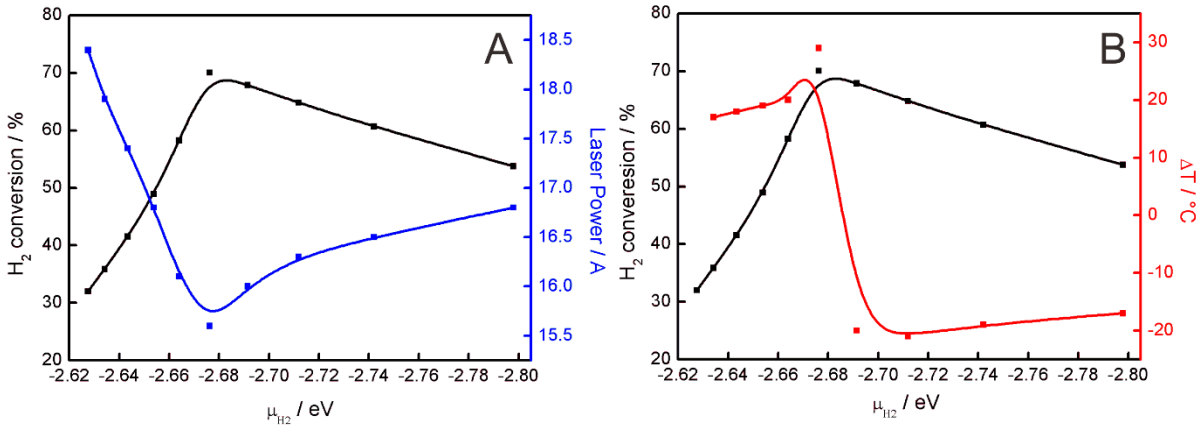

Figure 3.6 A) laser power and B) temperature variation with H_2 chemical potential at 800 °C during hydrogen oxidation.

The ESEM instrument is equipped with a heating stage that uses an infrared diode laser to heat the backside of the sample. The laser beam from the diode is coupled to an optical fiber to restrict the irradiation solely to the sample area, which maximizes the rate of local heating. The temperature of the platinum surface was measured via a *K-type* thermocouple spot-weld onto the sample center. Temperature was controlled by modulating the output current of the diode.

Hydrogen oxidation is an exothermic process (seen in equation (3-4)).

$$H_2\,(g) + 1/2O_2\,(g) \rightarrow H_2O\,(l) \quad \Delta H = -286\ kJ/mol \qquad (3\text{-}4)$$

The energy released during the reaction can be used to maintain the system temperature. Therefore one can also monitor the reaction rate by monitoring the laser power required to hold constant temperature. This parameter was recorded

and is shown in Figure 3.6A for different H_2 chemical potentials. Initially, the current output decreases when decreasing H_2 chemical potential from -2.63 eV (10 ml/min H_2). It reaches a minimum at -2.68 eV (5 ml/min H_2), and increases again with further decrease of the H_2 chemical potential to -2.80 eV (1 ml/min H_2). As water formation is an exothermic process, the reaction rate is positively correlated with the rate of thermal energy released and negatively correlated with the laser power output required to maintain a constant temperature. The laser power trend is in agreement with the catalytic activity measurements from the QMS.

To additionally pinpoint the fluctuation of Pt activity as a function of H_2 content, at each change to the H_2 flow rate, the laser output was initially kept constant to record the temperature change, ΔT, upon changing gas composition. In Figure 3.6B, the temperature change ΔT is plotted against hydrogen chemical potential. The decrease in H_2 chemical potential from -2.63 eV to -2.68 eV (10 ml/min to 5 ml/min H_2) is accompanied by a positive temperature difference, indicating that the reaction ratio increases each time the H_2 chemical potential decreases. The largest temperature increase occurs at the reaction ratio maximum (H_2 chemical potential at -2.68 eV at 5 ml/min). Further decreases in H_2 chemical potential after the rate maximum result in negative ΔT values, implying a decrease in reaction ratio for each decrease in H_2 chemical potential from -2.70 eV to -2.80 eV with H_2 mass flow from 4 ml/min to 1 ml/min. In addition, the sudden temperature drop at $\mu(H_2)$ = -2.68 eV of almost 50 °C may not only be explained by changes in the reactivity of the sample, but also may indicate a rapid surface cooling due to the endothermic reaction process.

3.4.1.5 Catalytic activity test for the second run

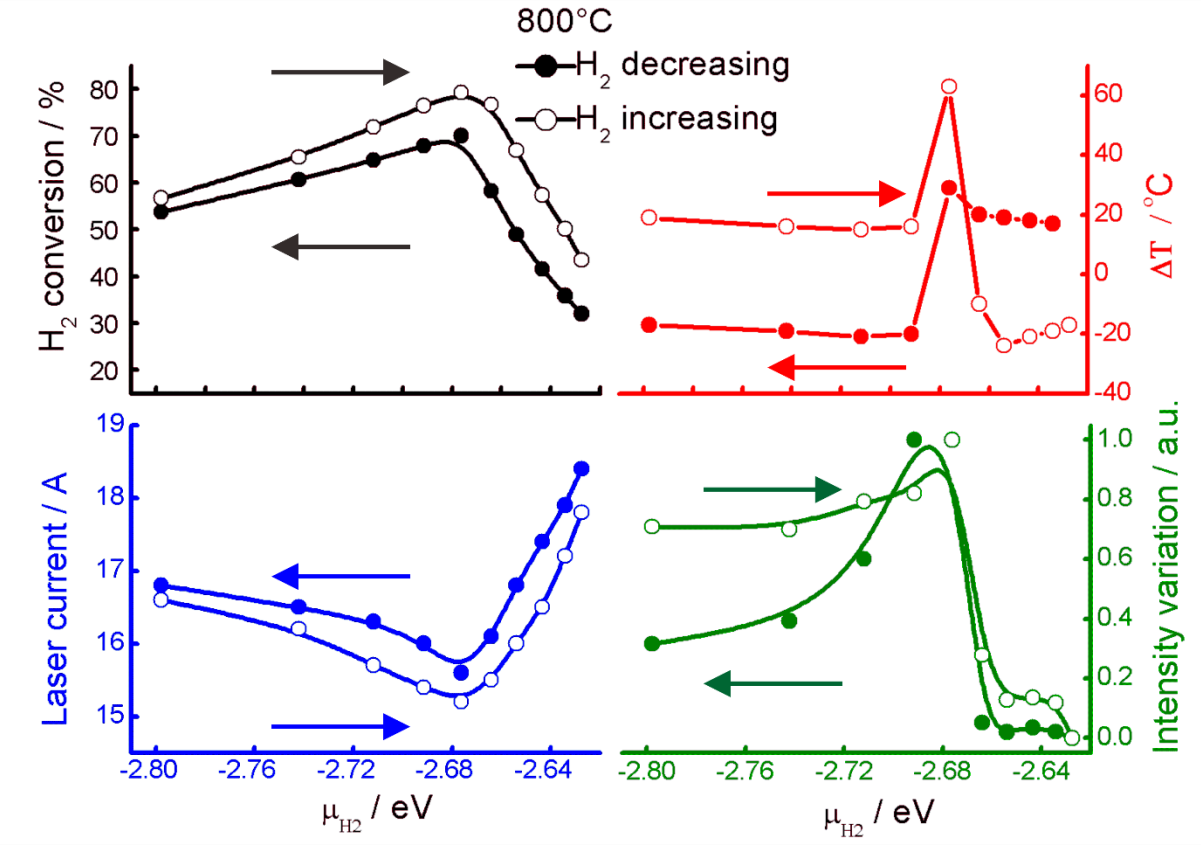

Figure 3.7 Hydrogen conversion, temperature variation, laser current and surface morphological variations versus H_2 chemical potential change of two consecutive cycles, hydrogen chemical potential decreasing (full circles) and increasing (open circles).

While each experiment started with a freshly reduced flat surface, previous work on ammonia oxidation points to the importance of surface roughening on catalyst activation.[13 23] In the present case, the entire surface became rough and covered with the roof- and square-shaped protrusions during the experiments where the H_2 chemical potential in progressively decreased. It would be interesting examine how the activity and dynamics change when starting from a rough surface and progressively increasing the H_2 concentration. The investigation is needed to investigate the influence of surface roughness on catalytic activity and to verify whether the morphological variation rate *k* is still the main factor influencing the catalytic activity.

To check this, we started from O_2-rich conditions with a roughened surface, and stepwise increased the H_2 chemical potential, while monitoring the H_2 consumption, laser power, ΔT and surface dynamics trends, seen in Figure 3.7. The H_2 chemical

potential was increased from -2.80 eV to -2.63 eV (1 ml/min to 10 ml/min H_2), with the sample at 800 °C while the oxygen mass flow was kept constant at 5 ml/min (O_2 chemical potential varied from -3.16 eV to -3.21 eV due to absence of internal gas). The H_2 conversion and surface dynamics showed similar trends, independent of the starting morphology of the surface.

Furthermore, in the second run (where the H_2 chemical potential was stepwise increased), that total H_2 conversion is higher than the first run (where the H_2 chemical potential was decreased). This observation is likely a reflection of the higher surface area of the roughened surface. The catalyst behavior has been further supported by monitoring the laser output and temperature variation. Laser power output decreased by 1 – 2 A in the second run compared to the first run due to the catalyst activity. Likewise, the temperature jump showed a large amplitude in the second run compared to the first run. During the second run, the surface morphologies were qualitatively similar to the first run.

3.4.1.6 Self-sustained oscillations induced by platinum catalyst activation

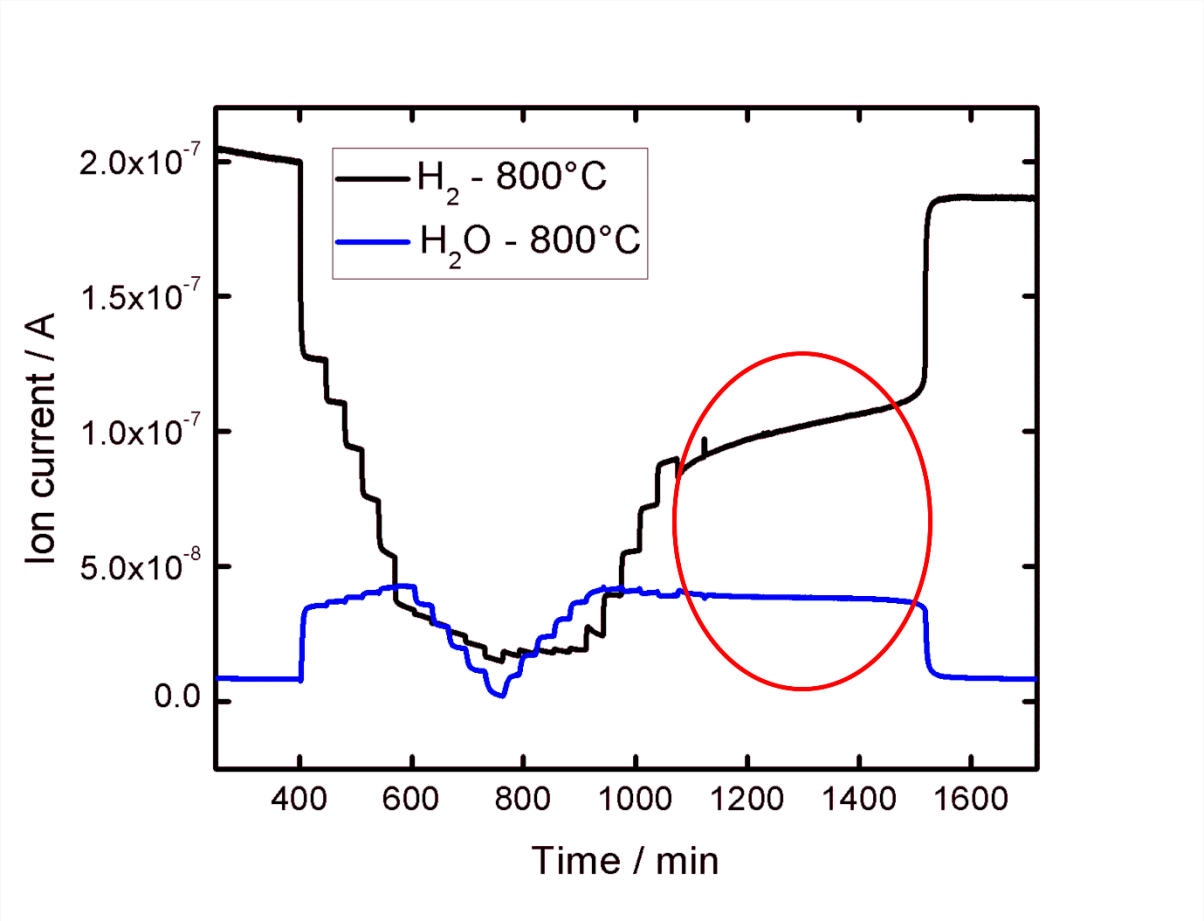

Figure 3.8 Self-sustained platinum activation at 800 °C at 5 ml/min O_2 and 10 ml/min H_2 marked by red circle, lasted for 7 hours.

Activation of the catalyst by oxygen or the reacting gases is the probable cause of the observed catalyst variability. Activation is often accompanied by a significant change in surface structure.[24] Here we can see that the surface became rougher and exhibited various structures depending on the reaction time and the gas composition. Interestingly, we have found here that, once activated, the catalyst can exhibit self-sustained activity, even after active heating is stopped. We find that after activation, if the laser power has been switched off, the catalyst continues to oxidize H_2 in a self-sustained way for an additional 7 hours, maintaining a temperature of ca. 412 °C. This phenomenon is demonstrated in Figure 3.8 marked by red circles. This plot shows the H_2 Ion current versus time, where at time of 1050 minutes the laser heating is stopped. The H_2 consumption continues, with a slow decrease in rate. The energy released from the exothermic reaction maintains an elevated temperature to continue and to drive the reaction. Eventually, as the reaction rate slowly decreases,

the temperature drops below 350 °C, at which point the reaction extinguishes and the H_2 consumption rapidly drops.

Sustained reaction was not observed when H_2 oxidation was carried out at 600 °C, and the sustained reaction only lasted for 20 minutes when H_2 oxidation was carried out at 700 °C. Clearly, in order for the reaction to be self-sustained, the reaction rate must be high enough that a temperature greater than 350 °C can be sustained.

3.4.2 XPS characterization

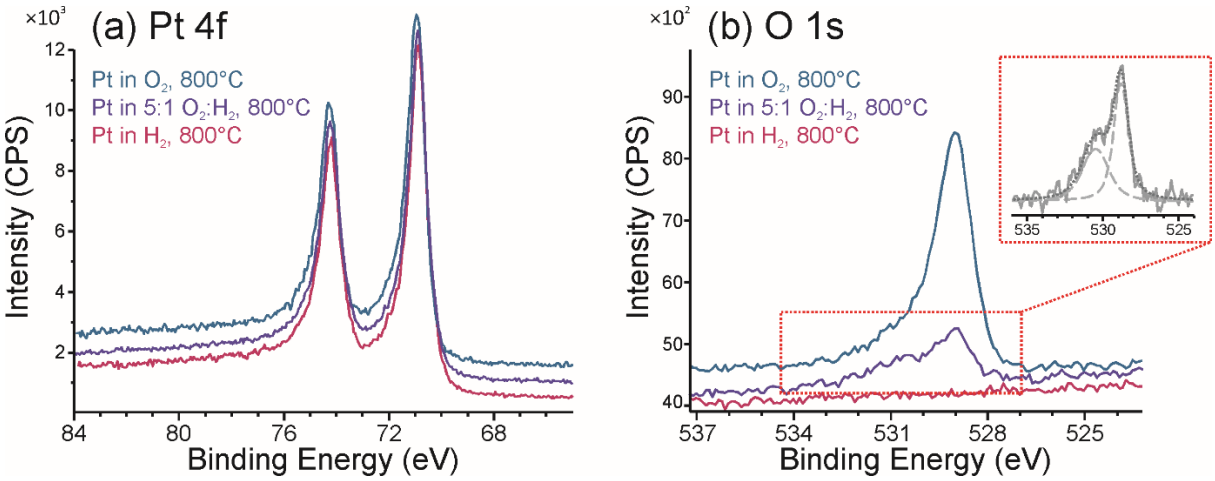

Figure 3.9 XPS spectra of Pt foil while being heated to 800 °C in 30 Pa of H_2, O_2 and a 1:5 mixture of H_2 and O_2.

In order to examine the chemical structure of the Pt surface under the relevant reaction conditions, we utilized NAP-XPS. We heated a sputter cleaned Pt foil to 800 °C in H_2, in O_2, and in a 1:5 mixture of H_2:O_2, while measuring the Pt 4*f*, O 1*s* and valence band spectra. The Pt 4*f* and O 1*s* spectra are shown in Figure 3.9. The photon energy used for the Pt 4*f* spectrum was 220 eV, and for the O 1*s* spectrum was 660 eV, yielding electron kinetic energies for the respective spectra of 150 eV and 130 eV. With these low kinetic energies the inelastic mean free path of electrons is ca. 0.4 nm, making the measurements extremely surface sensitive.

From the Pt 4*f* spectra there is no indication of chemical change when changing conditions. Thus, in O_2 at 800 °C there was no evidence for the formation of an oxide. Likewise, no oxide was evident in the mixture of H_2 and O_2. It should be noted that at these high temperatures, line broadening significantly decreases the energy resolution of XPS, such that subtle changes to peak shape, such as those expected for surface reconstructions could not be resolved.

By examining the O1s spectra under these conditions, one can see that an oxygen species is formed on the surface in O_2 at 800 °C. The fact that there is no observed chemical shift in the Pt spectrum, while an oxygen species is found in the O 1s spectrum suggests that the oxygen species could be from an O-termination. The O1s binding energy seen here (529.2 eV) is consistent with previous reports of O1s binding energies of O-reconstructions on Pt. Binding energies of O species on Pt span a rather wide range–from ca. 529.5 to 530.8 eV.[25-28] The O1s binding energies on Pt surface is rather sensitive to surface orientation. Oxygen species on high-index surfaces, such as Pt(533), Pt(332) and Pt(531), tend to have lower binding energies in the 529.5 eV range, while low-index surfaces such as Pt(111) have higher binding energies around 530.8 eV.

From the O1s spectrum measured in O_2 (Figure 3.9b), the main peak is located at 529.2 eV; however, the asymmetry on the high binding energy side of the peak suggests there are additional O species on higher binding energy side. When the reactive atmosphere was changed to a mixture of H_2 and O_2, the main O1s peak at 529.2 eV decreased in intensity, while the peak at higher binding energy becomes more apparent. A shoulder at higher binding energy becomes obvious (insert in Figure 3.9b), which could be a surface termination of sub-stoichiometric surface oxide. This observation could be a reflection the relative surface stabilities of O-terminated high index and O-terminated low-index surfaces. When H_2 is added to the mix, some of the adsorbed O-atoms are consumed by reaction with H_2. Presumably, the O atoms on the high-index surfaces are less stable than those on the low-index surface.[29] Thus, the O-atoms on the high index surfaces are the first to be consumed by reaction with H_2. This hypothesis could explain the change in relative O1s peak areas observed in Figure 3.9(b).

3.4.3 Morphological changes under constant oxygen chemical potential

In order to rate previous results, we compared the data to measurements that were conducted using Ar as balance gas to compensate the pressure drop during reduction of the hydrogen flow. This allowed us to maintain the identical operation pressure for various H_2 settings and keep the oxygen chemical potential constant.

3.4.3.1 Morphological changes at 800 °C

ESEM images which were recorded at different H_2 mass flows, in the presence of Ar as an internal balance gas, at a constant total mass flow of 16 ml/min and at a constant total pressure 100 Pa. These images are presented in Figure 3.10. The figures depict the situation monitored for the initial and end state as well as the difference for three different hydrogen chemical potentials. The contrast in the image of the last column represents the amount of morphological changes for a given time at each of the conditions.

Similar to Figure 3.4, the temperature was maintained at 800 °C, while the hydrogen flow rate was decreased in 1 ml/min steps from 10 ml/min to 1 ml/min. Each gas composition was held for 30 minutes to record the morphological variations. The difference is the total mass flow was kept constant in order to stabilize the total pressure. Complete data at each ratio are available (Video S3.24 to S3.43). Figure 3.10 shows images with a hydrogen chemical potential of -2.58 eV (flow rate of 10 ml/min A-C), -2.67 eV (H_2 flow rate at 4 ml/min D - F) and -2.80 eV (H_2 flow rate at 1 ml/min G - I). Obvious morphological changes begin when the hydrogen chemical potential of reaches -2.67 eV (4 ml/min H_2). Details on how the gas composition influences reactivity and morphological variation rate are given in Figure 3.11.

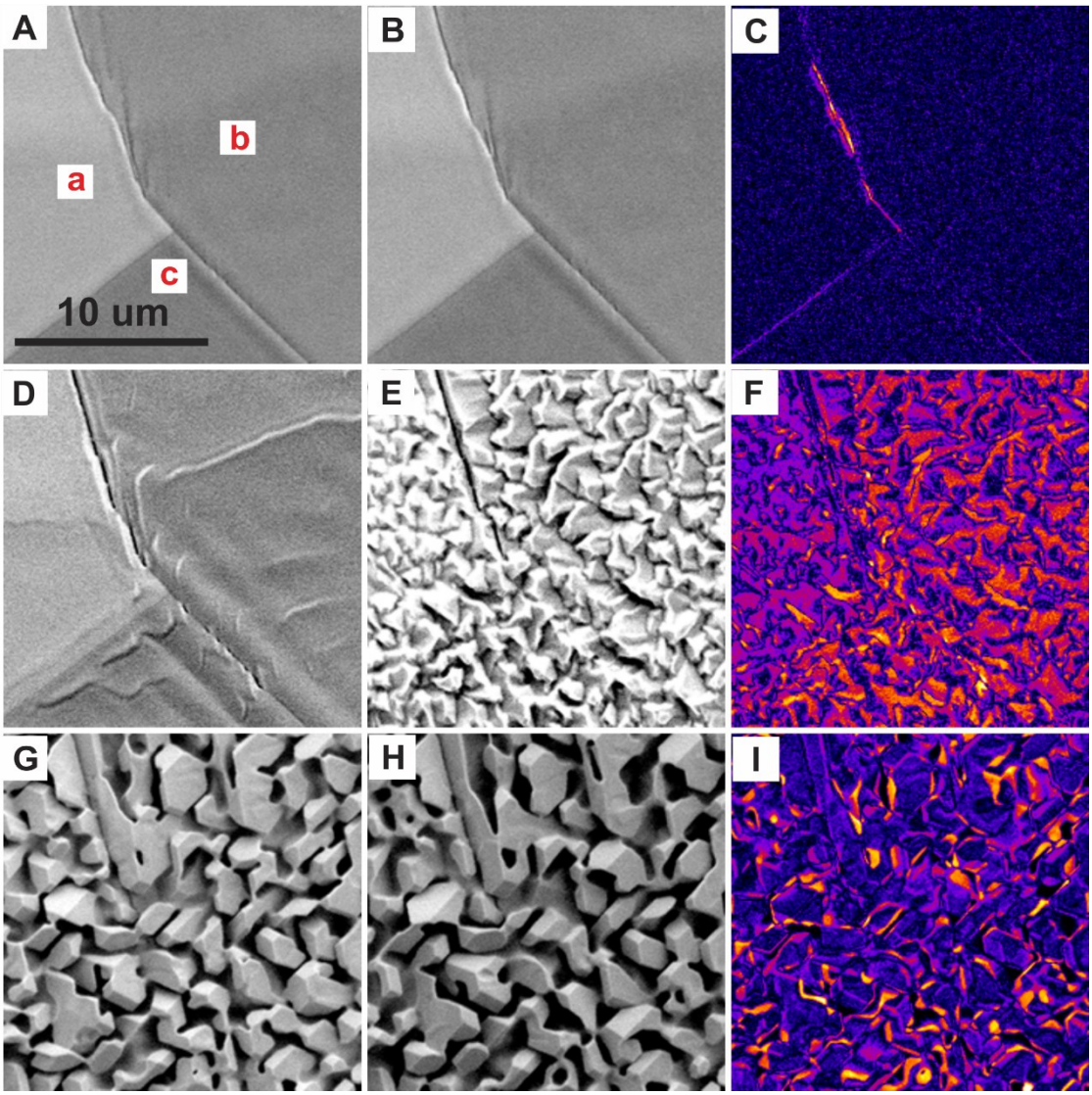

Figure 3.10. ESEM snapshots were selected to show the platinum surface morphology evolutions with the inert gas Ar in 30 mins at different H_2 chemical potentials -2.58 eV, -2.67 eV and -2.80 eV. A) is the surface morphology at the beginning, B) is after 30mins and C) is the difference of two morphologies at H_2 chemical potentials -2.58 eV (10 ml/min H_2); likewise, D – F) indicated the morphology changes at H_2 chemical potential -2.67 eV (4 ml/min H_2); G – I) at -2.80 eV (1 ml/min). Temperature was kept constant at 800 °C and total mass flow of 16 ml/min with constant oxygen chemical potential -3.17 eV at a mass flow of 5 ml/min.

3.4.3.2 Catalytic activity changes at 800 °C

Similar to the previous measurements, experimental conditions were cycled while the H_2 consumption, laser power, temperature difference ΔT and surface dynamics trends were monitored (Figure 3.11). The H_2 conversion showed a similar tendency with morphological variation rate compared to Figure 3.7, i.e. the H_2 conversion and

surface dynamics first increase with decreasing H_2 chemical potential and peaked at -2.67 eV (4 ml/min H_2). Correspondingly, the laser power showed the opposite tendency due to H_2 oxidation is an exothermic reaction, which means less laser power is required to main 800 °C. This observation is independent of the starting morphology of the surface. In addition during cycling a higher conversion was observed.

However, the maximum of the conversion appeared at different H_2 chemical potentials: In the first run, the H_2 conversion reached the maximum at H_2 -2.67 eV (4 ml/min H_2) but in the second run (increasing the H_2 mass flow) the H_2 conversion reached maximum at $\mu(H_2)$ = -2.65 eV. Thus, the highest activity requires more H_2 chemical potential compared to the first run which reached the maximum at -2.67 eV (4 ml/min H_2). This observation is different to Figure 3.7 without internal gas, which shows the maxima at -2.68 eV (5 ml/min H_2 and 5 ml/min O_2) for both runs.

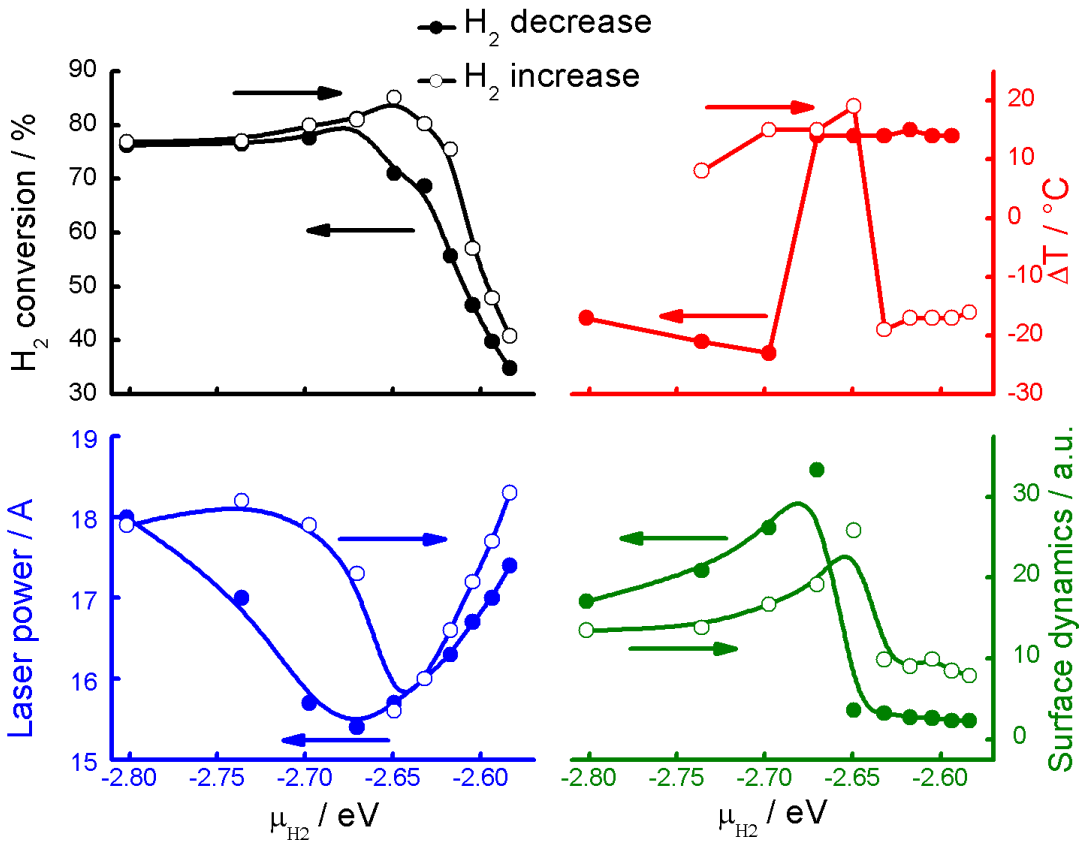

Figure 3.11 Hydrogen conversion, temperature variation*, laser current and surface morphological variations versus H_2 chemical potential change of two consecutive cycles, hydrogen concentration decreases (full circles) and increases (open circles). Temperature is*

constant at 800 °C and Ar is applied as inert gas to keep the total mass flow constant at 16 ml/min and pressure at around 100 Pa.

3.5 Discussion

3.5.1 Catalytic activity in a mixture of H_2 and O_2

Numerous publications have discussed the mechanism of water formation on platinum, and several conflicting models have been proposed.[30-31] Ertl and co-workers[32] observed this reaction with STM, combined with high-resolution electron energy loss (HREELS) spectra. Two distinct temperature-dependent mechanisms to H_2O formation were observed. At temperature < 180 K, the formed H_2O remains on the surface. The authors suggested an O disproportionation reaction,

$$H_2O_{(ads)} + O_{(ads)} \rightarrow 2OH_{(ads)} \quad (3\text{-}5)$$

Above the H_2O desorption temperature (> 180 K), when H_2O cannot remain on the surface, H_2O formed via the simple successive addition of adsorbed H(ads) to adsorbed O (O(ads))

$$O_{(ads)} + H_{(ads)} \rightarrow OH_{(ads)} \quad (3\text{-}6)$$

$$OH_{(ads)} + H_{(ads)} \rightarrow H_2O_{(ads)} \rightarrow H_2O_{(gas)} \quad (3\text{-}7)$$

Since our temperature is much higher than 180 K, H_2O cannot remain on the surface, so our study is within the high temperature regime (>180 K). In our experiment, without internal gas, O_2 was maintained at 5 ml/min, and H_2 was varied from 10 to 0 ml/min.

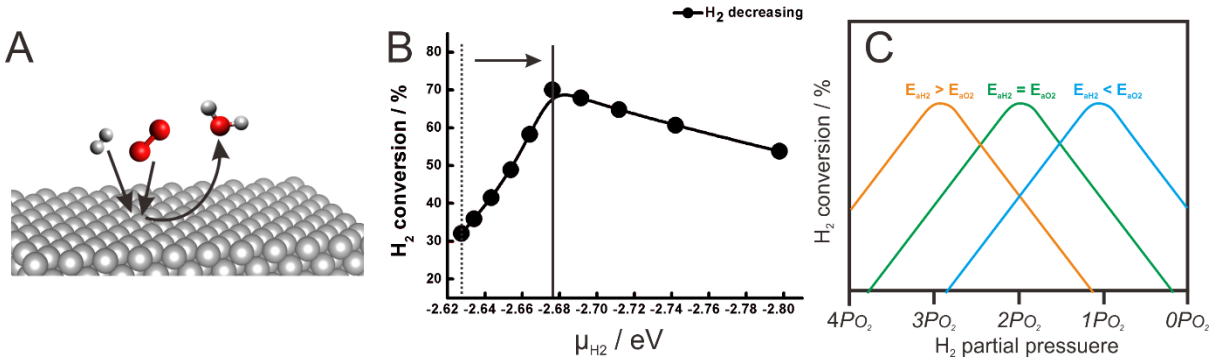

Figure 3.12 A) Mechanistic model to explain the dynamic process (gray and red balls indicate hydrogen and oxygen atoms, respectively); B) A plot of hydrogen conversion rate as a function of hydrogen chemical potential, as H_2 chemical potential decreased from -2.63 eV to -2.80 eV (flow rate decreases from 10 ml/min to 1 ml/min) at 800 °C, with a constant oxygen mass flow 5 ml/min. Black solid line shows the hydrogen maximum conversion is at 5 ml/min H_2 and the dashed line shows where one would expect the maximum conversion rate based on the stoichiometry of the chemical; C) shows how the maximum activity would change with H_2 partial pressure, depending on whether the activation barrier for H_2 adsorption is less than, equal to, or greater than the activation barrier for O_2 adsorption.

From stoichiometric considerations alone, the conversion would reach a maximum when H_2 concentration is twice that of O_2, in the present case, at 10 ml/min (the dashed line in Figure 3.12B). However, our experiment demonstrated that the reaction ratio was a maximum at an H_2 flow rate of 5 ml/min, (i.e. 50% H_2 ratio), as indicated by solid line in Figure 3.12B. The reason for the deviation from the stoichiometric ratio, is that on catalysts where the Langmuir-Hinshelwood (L-H) represents the reaction mechanism (as depicted in Figure 3.12A), the reaction rate depends on the relative populations of adsorbed surface species, which in turn depends on the relative rates of adsorption/desorption of the respective surface species. Consequently, the adsorbate with the larger adsorption energy (i.e. more strongly bound) will be in higher surface populations at a given gas phase chemical potential. Thus the rate maximum will be obtained when the more strongly bound element is present in the gas phase in a proportion that is lower than the stoichiometric proportion.

In the L-H concept, the reaction between adsorbates (H and O) is given by $R = kv_Hv_O$, provided that the reaction at the surface is the rate limiting step. A symmetric curve of H_2 conversion rate versus H_2 partial pressure is plotted in Figure 3.12C. A maximum at stoichiometric point, where H_2 partial pressure equals two times of O_2 partial pressure ($P_{H2} = 2P_{O2}$), is expected, if the adsorption energy of hydrogen and oxygen on platinum are equal $E_{H2} = E_{O2}$. When hydrogen partial pressure is higher than $2P_{O2}$ ($P_{H2} > 2P_{O2}$), the surface is predominantly covered by hydrogen, with the reaction rate being limited by the oxygen adsorbate concentration. Likewise, the platinum surface is mainly covered with oxygen in hydrogen lean conditions ($P_{H2} < 2P_{O2}$) with hydrogen coverage limiting the reaction. The curve can shift to higher hydrogen partial pressure side (red curve in Figure 3.12C) when $E_{H2} < E_{O2}$, which means the adsorption energy of hydrogen on the catalyst surface is smaller than oxygen.[33] Similarly, if $E_{H2} > E_{O2}$, then the red curve would sit on the lower hydrogen partial pressure side (blue curve in Figure 3.12C). According to previous literature reports, the adsorption energy of hydrogen on Pt (111) is 0.7 eV in the ranges $180 < T < 440$ K and $5 \times 10^{-6} < P < 5 \times 10^{-2}$ Pa, [34] which is much smaller than the oxygen adsorption energy on Pt 2.5 eV.[33, 35]

Based on the Sabatier principle[36]: the volcano-like behaviour of the H_2 consumption ratio may also indicate changes in the relative adsorption affinities of H_2 and O_2 indicating the exposure of different surfaces. Correspondingly, the molecular coverage-dependent sticking coefficient $S_{H2}(\theta)$ and $S_{O2}(\theta)$, θ is the total surface coverage $0 \leq \theta \leq 1$[33, 37-38], are depends on the activation energy for adsorption. Approximate values of the high temperature 900-1300 K sticking coefficients, $S_{H2}(\theta) = 0.04$ and $S_{O2}(\theta) = 0.02$, in the pressure range 0.27-27 Pa.[39] Our observation at 800 °C in a mixture of H_2 and O_2 (30 ~ 60 Pa) fits well with the literature, where the maximum of water production is at H_2 5 ml/min and O_2 5 ml/min, in Figure 3.12B. This means hydrogen and oxygen adsorbates on the platinum surface reach the optimum ratio for H_2O production, which should be most active ratio for the Pt-O and Pt-H bonds formation and cleavage. It can be further shown in Figure 3.4, at H_2 5 ml/min and O_2 5 ml/min (50% H_2), the morphology shows the fastest dynamics compared to other ratios, supporting Videos S3.3 - 3.13.

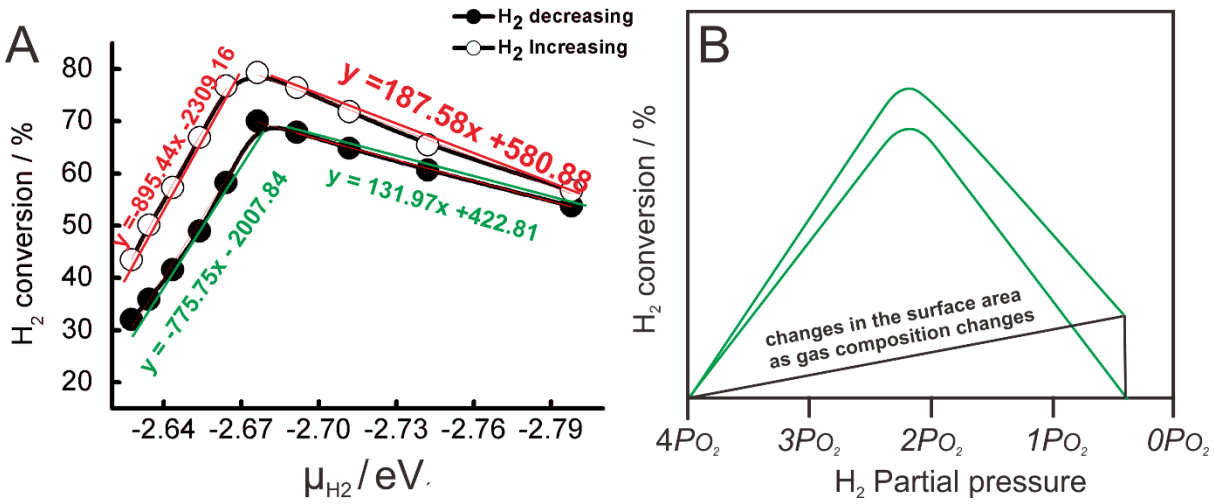

Figure 3.13 A) is the plot of H_2 conversion versus hydrogen concentration at 800 °C; B) the mechanism shows the H_2 conversion has been increased due to the surface roughening process.

What is easily overlooked when considering the symmetric volcano plots of Figure 3.13C is that the different adsorbates can stabilize different crystal faces. The transition from a state where one adsorbate is dominant to a state where a different adsorbate is dominant can give rise to significant surface re-structuring, and even changes in total surface area. We see this effect clearly with the ESEM images taken at H_2-rich versus O_2-rich conditions, in Figure 3.13A. The surface under the O_2-rich conditions is much rougher, and therefore consists of a larger total surface area than the relatively flat surface under H_2-rich conditions. Thus, while one moves from high-H_2 concentration to low-H_2 concentration, one is inducing an increase in surface area, which subsequently increases the total activity of the material, as depicted in Figure 3.13B. This plot shows the symmetric volcano plot expected if the surface area does not change while one changes chemical potential, and the asymmetric curve expected when the surface area increases as the chemical potential becomes more H_2-lean.

This effect is believed to be the reason for the asymmetry of the measured activity curve. By asymmetry we mean that the slope of the activity curve before the maximum is different from the slope of the curve after the activity maximum. Figure 3.13A shows the activity measurements during a decrease in H_2 concentration, where the surface area progressively increases (black dots) and the activity as the opposite direction as the H_2 concentration is progressively increased (black dots).

One can see that the asymmetric trend is reproduced in both cases, while the corresponding ESEM images also demonstrate the expected changes in surface roughness (i.e. smooth surface under H_2-rich conditions, and rough surface under H_2-poor conditions).

3.5.2 The effect of dilution - comparison of conversion and morphological changes

Figure 3.14 compares the H_2 conversion and morphology variation rate of both outlined scenarios. Without internal gas, the total pressure decreases from 60 Pa to 30 Pa when H_2 chemical potential decreased from -2.63 eV to -2.80 eV. During this decrease the H_2 conversion increases from 32% to 70% and reaches a maximum at a H_2 chemical potential at -2.68 eV (H_2 mass flow at 5 ml/min), indicated by the black line in Figure 3.14A. Furthermore, the normalized morphological variation rate, as shown by the black line in Figure 3.14B, increases slightly in the H_2 chemical potential range between -2.63 eV to -2.65 eV (H_2 decreased from 10 ml/min to 6 ml/min), which is followed by an immediate increase to 1.00 at a H_2 chemical potential at -2.68 eV (5 ml/min H_2). As can be clearly seen in Video S3.8, the whole surface heavily started to reconstruct at -2.68 eV (5 ml/min H_2). Subsequently, the H_2 conversion decays from 70% to 54% with a further decrease of the H_2 chemical potential. The activity decay is accompanied by 68% slower morphological variations.

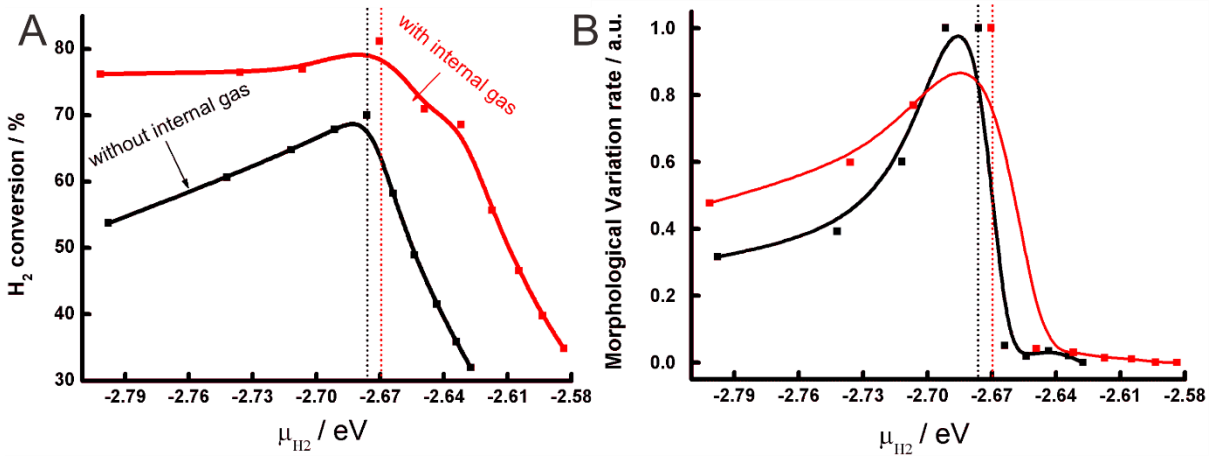

Figure 3.14 A) is the comparison of H_2 conversion with and without internal argon gas at 800 °C; B) shows the correlated morphological variation rate under both conditions.

In the second scenario the decrease of the H_2 mass flow was balanced with Ar and the system pressure was kept at 100 Pa. The H_2 conversion (red line in Figure 3.14A)

and morphological variation rate k (red line in Figure 3.14B) correlate well with each other and exhibit slightly different increasing and decreasing tendencies as without inert gas: The H_2 conversion first increases from 35% to 81% when the H_2 chemical is potential decreased from -2.58 eV to -2.67 eV (H_2 deceased from 10 ml/min to 4 ml/min), and levels off at to 76% at lower H_2 chemical potential of -2.80 eV (1 ml/min H_2), indicating almost no deactivation after the peak has reached.

Additionally, the differences can be observed in the H_2 conversion in parallel without and with internal gas (Figure 3.14A). Without internal gas The H_2 conversion reaches a maximum at 70% for a H_2 chemical potential of -2.68 eV (5 ml/min H_2), while, the conversion with internal gas reaches a maximum at 81% at the same H_2 chemical potential of -2.67 eV (4 ml/min), suggesting a catalyst that is slightly more active. A slight shift of the maximum can be also verified by the morphological variation rate (Figure 3.14B). With internal gas the morphological variation rate is only 0.04 at H_2 chemical potential -2.65 eV (5 ml/min H_2), almost no surface reconstruction can be observed (Video S3.29). An immediate jump to 1 is recognized after the H_2 chemical potential has reached -2.67 eV (4 ml/min), which is reflected in the Video S3.30, showing rapid reshaping of the catalyst.

Interestingly, we observed that with internal gas, the surface exhibits dynamics at a lower H_2 chemical potential (seen in Video S3.33). However, without inert gas the surface become almost static which is accompanied by a decay of the conversion to 54% (seen in Video S3.12).

Already in early works, the reaction order of oxygen and hydrogen in the hydrogen oxidation reaction over Pt catalysts has been discussed controversially, and it was concluded that they depend crucially on the reaction conditions.[30] The initial increase of the H_2 conversion with decreasing H_2 chemical potential indicates an inverse reaction order towards hydrogen and may be accompanied by H_2 surface poisoning. After falling below a H_2 chemical potential -2.67 eV (4 ml/min) the reaction is supposed to be almost zero order in terms of the H_2 chemical potential, which is indicated by the almost constant conversion for further the H_2 decrease. This reaction order change is accompanied by a sudden catalyst reshaping at a H_2 chemical potential -2.67 eV (4 ml/min).

However, this reshaping would not only involve surface, but also the sub-surface or even the bulk could play an important role. As an example, a FIB lamellae was cut and lift out from the reconstructed Pt surface after the reaction (Figure 3.15). It shows that the surface reshaping depth is around 370 nm. This already suggests that bulk contributions to the surface reconstructions are needed. Based on the the height of the reconstructed facet and the area of imaged region, we calculated the amount of Pt atoms that is needed to form theses reconstruction. It amounts to 6.6168 x 10^{17} atoms, while a surface monolayer in the field of view (0.5 x 0.5 cm^2) is only composed of 3.2675 x 10^{14}, 2.31 x 10^{13}, 3.7725 x 10^{14} atoms. These number of atoms correspond to a (100), (110) (111) terminated monolayer, respectively. These examples suggest that the observed reshaping of the crystal could have also occurred via diffusion along the surface. The exact driving force that is needed for reconstruction and to overcome the energy of cohesion of Pt, remains unclear.

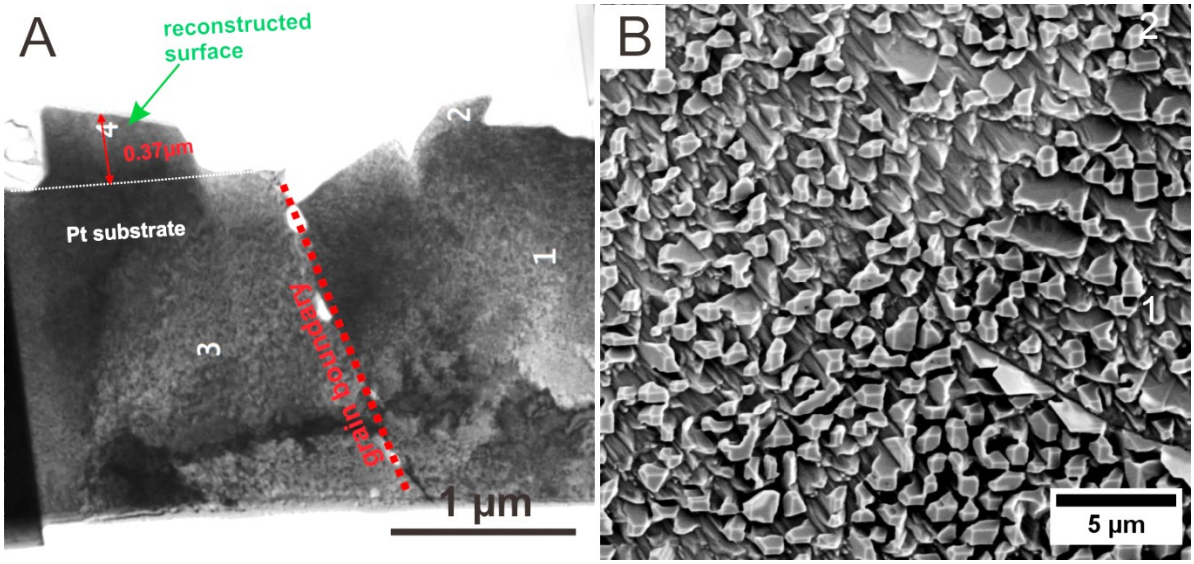

Figure 3.15 A thin lamella is cut and lift out from the reconstructed platinum surfaces.

However, from our data we can propose that, initially a balanced and equilibrated mixture of hydrogen and oxygen can be saturated in the bulk. During reduction of the H_2 gas phase concentration the hydrogen in the bulk is depleted and oxygen becomes the dominating species. Oxygen, however, is much larger then hydrogen and may thus induce higher strain into the Pt lattice. At a certain threshold value strain of this frustrated oxide system, i.e. Pt and oxygen may coexist in excited metastable energy states, may be relieved by a sudden reshaping mimicking a rough surface with different adsorption sites.

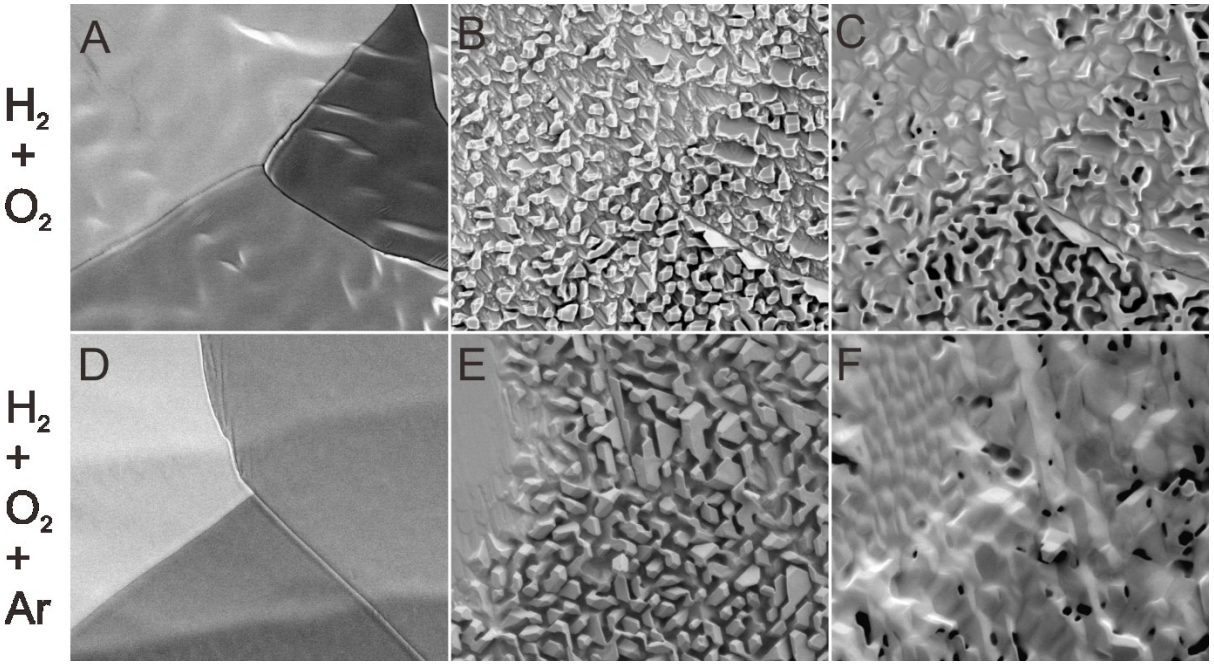

Figure 3.16 shows the morphological changes during the cycle from 10 ml/min H_2 to 1 ml/min then back to 10 ml/min H_2. A), B) and C) are morphological changes without internal gas; C), D) and E) are with argaon as the diluent gas.

For the situation without internal gas the initial situation of reaction may be similar as the conversion increases with decreasing H_2 concentration, seen in Figure 3.16 E and F. However, after the threshold value of the H_2 chemical potential of -2.68 eV (5 ml/min) the conversion decreases again. This suggests that the reshaped surface may be poisoned by oxygen for low H_2 chemical potentials. Similar to the scenario described above the turning point of conversion is initiated by reshaping of the catalyst, which in this case seems to be almost irreversible (Figure 3.16 A - C).

3.6 Conclusions

We use hydrogen oxidation as a model reaction to investigate the influence of surface morphological changes to its catalytic activity on a platinum catalyst. We have found that the surface morphological variation rate *k* can help to explain the catalytic activity under conditions with and without internal gas. When H_2 conversion rate reached a maximum at H_2 chemical potential -2.68 eV (5 ml/min H_2) for both runs without internal gas, the surface morphological variation rate also reached a maximum; with internal gas, the maximum peaked at around -2.68 eV for the first run and -2.65 eV in the second run with internal gas. Pretreatment to increase surface roughness can improve the catalytic activity, due to the surface area enlargement.

Around 7 hours self-sustained reaction can be reached by activation of platinum at 800 °C in H_2 and O_2. Furthermore, a possible mechanism was proposed to explain the highest catalytic activity at -2.68 eV (5 ml/min H_2 and O_2) and surface area increase induced the activity increase. Finally, the possibilities are proposed to explain the difference between with and without internal gas.

3.7 References

1. Katayama, Y.; Giordano, L.; Rao, R. R.; Hwang, J.; Muroyama, H.; Matsui, T.; Eguchi, K.; Shao-Horn, Y., Surface (Electro)chemistry of CO2 on Pt Surface: An in Situ Surface-Enhanced Infrared Absorption Spectroscopy Study. *J Phys Chem C* **2018,** *122* (23), 12341-12349.
2. Evtuguin, D. V.; Neto, C. P., Heteropolyanions catalysis for ecologically friendly bleaching technologies: Principles and applications. *Advances in Lignocellulosics Chemistry for Ecologically Friendly Pulping and Bleaching Technologies* **1998**, 589-592.
3. Butcher, D. R.; Salmeron, M. B.; Somorjai, G. A., STM studies of adsorbate-induced surface restructuring of Pt(100) in ethylene adsorption, hydrogenation, and poisoning by CO. *Abstr Pap Am Chem S* **2010,** *240*.
4. Fuchs, S.; Hahn, T., The oxidation of carbon monoxide by oxygen over polycrystalline platinum, palladium and rhodium from UHV to normal pressure. *Stud Surf Sci Catal* **1995,** *96*, 275-284.
5. Fuchs, S.; Hahn, T.; Lintz, H. G., The Oxidation of Carbon-Monoxide by Oxygen over Platinum, Palladium and Rhodium Catalysts from 10(-10) to 1-Bar. *Chem Eng Process* **1994,** *33* (5), 363-369.
6. Jung, N.; Chung, D. Y.; Ryu, J.; Yoo, S. J.; Sung, Y. E., Pt-based nanoarchitecture and catalyst design for fuel cell applications. *Nano Today* **2014,** *9* (4), 433-456.
7. Gland, J. L.; Korchak, V. N., Ammonia Oxidation on a Stepped Platinum Single-Crystal Surface. *J Catal* **1978,** *53* (1), 9-23.
8. Hendriksen, B. L. M.; Frenken, J. W. M., CO oxidation on Pt(110): Scanning tunneling microscopy inside a high-pressure flow reactor. *Physical Review Letters* **2002,** *89* (4).
9. Behm, R. J.; Thiel, P. A.; Norton, P. R.; Ertl, G., The Interaction of Co and Pt(100) .1. Mechanism of Adsorption and Pt Phase-Transition. *J Chem Phys* **1983,** *78* (12), 7437-7447.
10. Wicke, E.; Onken, H. U., Periodicity and Chaos in a Catalytic Packed-Bed Reactor for Co Oxidation. *Chem Eng Sci* **1988,** *43* (8), 2289-2294.
11. Philippou, G.; Luss, D., Temperature Patterns on a Catalytic Ribbon Heated by a Constant Voltage. *Chem Eng Sci* **1993,** *48* (12), 2313-2323.

12. Harris, P. J. F., Sulfur-Induced Faceting of Platinum Catalyst Particles. *Nature* **1986,** *323* (6091), 792-794.

13. Kraehnert, R.; Baerns, M., Morphology changes of Pt-foil catalyst induced by temperature-controlled ammonia oxidation near atmospheric pressure. *Appl Catal a-Gen* **2007,** *327* (1), 73-81.

14. Nilsen, O.; Kjekshus, A.; Fjellvag, H., Reconstruction and loss of platinum catalyst during oxidation of ammonia. *Appl Catal a-Gen* **2001,** *207* (1-2), 43-54.

15. Flytzani-Stephanopoulos, M.; Wong, S.; Schmidt, L. D., Surface Morphology of Platinum Catalysts. *J Catal* **1977,** *49* (1), 51-82.

16. Stepanova, L. N.; Belskaya, O. B.; Salanov, A. N.; Serkova, A. N.; Likholobov, V. A., SEM study of the surface morphology and chemical composition of the MgAl- and MgGa-layered hydroxides in different steps of platinum catalysts Pt/Mg(Al, Ga)O-x synthesis. *Appl Clay Sci* **2018,** *157*, 267-273.

17. Mccabe, R. W.; Pignet, T.; Schmidt, L. D., Catalytic Etching of Platinum in Nh3 Oxidation. *J Catal* **1974,** *32* (1), 114-126.

18. Schlogl, R., Heterogeneous Catalysis. *Angew Chem Int Edit* **2015,** *54* (11), 3465-3520.

19. Knop‐Gericke, A.; Kleimenov, E.; Hävecker, M.; Blume, R.; Teschner, D.; Zafeiratos, S.; Schlögl, R.; Bukhtiyarov, V. I.; Kaichev, V. V.; Prosvirin, I. P.; Nizovskii, A. I.; Bluhm, H.; Barinov, A.; Dudin, P.; Kiskinova, M., Chapter 4 X‐Ray Photoelectron Spectroscopy for Investigation of Heterogeneous Catalytic Processes. In *Advances in Catalysis*, Academic Press: 2009; Vol. 52, pp 213-272.

20. Hannevold, L.; Nilsen, O.; Kjekshus, A.; Fjellvag, H., Reconstruction of platinum-rhodium catalysts during oxidation of ammonia. *Appl Catal a-Gen* **2005,** *284* (1-2), 163-176.

21. Lyubovskii, M. R.; Barelko, V. V., Formation of the Structure, Which Look Like Metal Wool, on the Surface of the Platinum Catalyst in Ammonia Oxidation Reaction. *Dokl Akad Nauk+* **1993,** *333* (1), 60-62.

22. Lyubovsky, M. R.; Barelko, V. V., Formation of Metal Wool Structures and Dynamics of Catalytic Etching of Platinum Surfaces during Ammonia Oxidation. *J Catal* **1994,** *149* (1), 23-35.

23. Basbus, J. F.; Prado, F. D.; Caneiro, A.; Mogni, L. V., A comparative study of high temperature properties of cobalt-free perovskites. *Journal of Electroceramics* **2014,** *32* (4), 311-318.

24. Dawson, P. T.; Peng, Y. K., Adsorption, Desorption, and Exchange-Reactions of Oxygen, Hydrogen, and Water on Platinum Surfaces .4. Field-Emission Studies on the Adsorption of Water, Hydrogen and the Reaction between Hydrogen and Adsorbed Oxygen. *Surf Sci* **1980,** *92* (1), 1-13.

25. Parkinson, C. R.; Walker, M.; McConville, C. F., Reaction of atomic oxygen with a Pt(111) surface: chemical and structural determination using XPS, CAICISS and LEED. *Surf Sci* **2003,** *545* (1-2), 19-33.

26. Gunther, S.; Scheibe, A.; Bluhm, H.; Haevecker, M.; Kleimenov, E.; Knop-Gericke, A.; Schlogl, R.; Imbihl, R., In situ X-ray photoelectron spectroscopy of catalytic ammonia oxidation over a Pt(533) surface. *J Phys Chem C* **2008,** *112* (39), 15382-15393.

27. Wang, J. G.; Li, W. X.; Borg, M.; Gustafson, J.; Mikkelsen, A.; Pedersen, T. M.; Lundgren, E.; Weissenrieder, J.; Klikovits, J.; Schmid, M.; Hammer, B.; Andersen, J. N., One-dimensional PtO2 at Pt steps: Formation and reaction with CO. *Physical Review Letters* **2005,** *95* (25).

28. Held, G.; Jones, L. B.; Seddon, E. A.; King, D. A., Effect of oxygen adsorption on the chiral Pt{531} surface. *J Phys Chem B* **2005,** *109* (13), 6159-6163.

29. Yue, J.; Du, Z.; Shao, M. H., Mechanisms of Enhanced Electrocatalytic Activity for Oxygen Reduction Reaction on High-Index Platinum n(111)-(111) Surfaces. *J Phys Chem Lett* **2015,** *6* (17), 3346-3351.

30. Roberts, M. W., The Chemical Physics of Solid-Surfaces and Heterogeneous Catalysis, Vol 4, Fundamental-Studies of Heterogeneous Catalysis - King,Da, Woodruff,Dp. *J Chem Soc Farad T 1* **1983,** *79*, 2262-2263.

31. Thiel, P. A.; Madey, T. E., The Interaction of Water with Solid-Surfaces - Fundamental-Aspects. *Surf Sci Rep* **1987,** *7* (6-8), 211-385.

32. Volkening, S.; Bedurftig, K.; Jacobi, K.; Wintterlin, J.; Ertl, G., Dual-path mechanism for catalytic oxidation of hydrogen on platinum surfaces. *Phys Rev Lett* **1999,** *83* (13), 2672-2675.

33. Hellsing, B.; Kasemo, B.; Zhdanov, V. P., Kinetics of the Hydrogen Oxygen Reaction on Platinum. *J Catal* **1991,** *132* (1), 210-228.

34. Norton, P. R.; Davies, J. A.; Jackman, T. E., Absolute Coverage and Isosteric Heat of Adsorption of Deuterium on Pt(111) Studied by Nuclear Microanalysis. *Surf Sci* **1982,** *121* (1), 103-110.

35. Luth, H., Low-Energy Electronic and Vibronic Excitations of Semiconductor Surfaces. *Surf Sci* **1983,** *126* (1-3), 126-146.

36. Medford, A. J.; Vojvodic, A.; Hummelshoj, J. S.; Voss, J.; Abild-Pedersen, F.; Studt, F.; Bligaard, T.; Nilsson, A.; Norskov, J. K., From the Sabatier principle to a predictive theory of transition-metal heterogeneous catalysis. *J Catal* **2015,** *328*, 36-42.

37. Lukyanycheva, V. I.; Fokina, L. A.; Shumilova, N. A., The Effect of Chemisorption Processes on the Kinetics of Molecular-Oxygen Reduction and Other Reactions at Platinum - the Effect of Preoxidation Potential on the Rate and on Coverage of the Reduced Platinum Surface by Adsorbed Hydrogen and Water-Molecules in Acidic Solution. *Sov Electrochem+* **1979,** *15* (11), 1394-1398.

38. Kharkovskaia, E. N.; Boreskov, G. K.; Slinko, M. G., The Kinetics of the Reaction between Hydrogen and Oxygen on Platinum. *Dokl Akad Nauk Sssr+* **1959,** *127* (1), 145-148.

39. Ljungstrom, S.; Kasemo, B.; Rosen, A.; Wahnstrom, T.; Fridell, E., An Experimental-Study of the Kinetics of Oh and H2o Formation on Pt in the H2+O2 Reaction. *Surf Sci* **1989,** *216* (1-2), 63-92.

3.8 Supplementary information

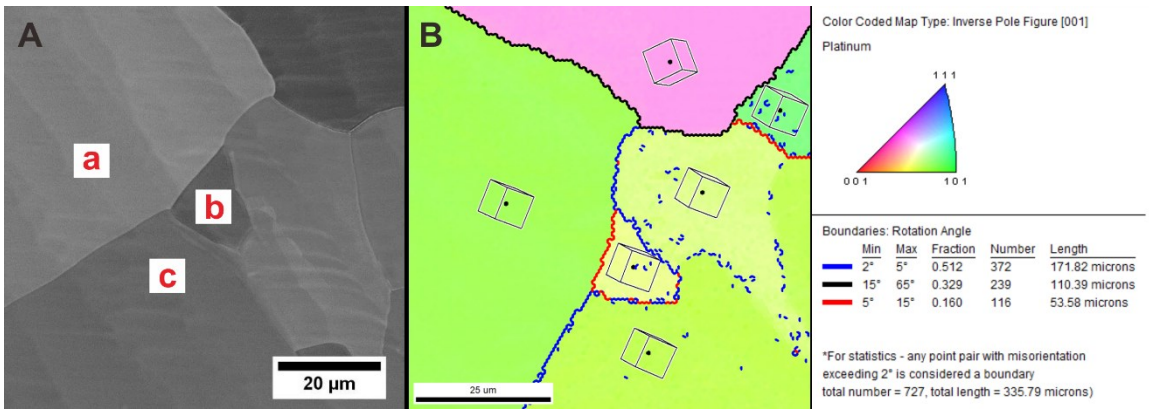

Figure S 3.1 After reaction, platinum foil was reduced at 10 ml/min H_2 at 800 °C for 5 hours till the surface get flat, SEM images shown in A); B) is the electron backscattering diffraction (EBSD) image which shows grain a, b and c are 6~7°, 5° and 4° misorientation from <210> separately.

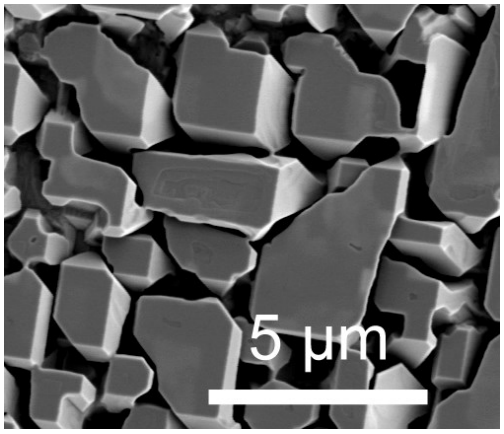

Figure S3.2 A high-resolution SEM image shows the reconstructed platinum surface at 1 ml/min H_2 and 5 ml/min O_2 at 800 °C. Square, rectangular and cropped rectangular shapes are coexist on the surface.

4 *In situ* SEM study of self-sustained oscillations induced by hydrogen oxidation over Ni catalysts

4.1 Abstract

Surface structures of catalysts are important in heterogeneous catalysis as they can greatly influence the catalytic activity. In addition, the exposure of such functional materials to different gaseous environments causes the formation of new surface structures. Here we report on the direct observation of surface changes and dynamics of nickel catalysts under reaction conditions by environmental scanning electron microscopy (ESEM). Chemical changes of the gas phase are monitored on-line by a quadrupole mass analyser (QMS). Oscillations with varying frequencies over a nickel foam have been detected during the catalytic oxidation of hydrogen. These oscillations depend on the ratios of the reactants and the temperatures of the reaction. For each oxygen content, the surface exhibits different and fluctuating morphologies, which could be correlated to the oscillation of on-line measured mass traces of the reactants and the product. These oscillations exhibit different frequencies as well as amplitudes and depend on the applied reaction parameters.

4.2 Introduction

Heterogeneous catalysts represent systems far from thermodynamic equilibrium. They feature a group of phenomena which are denoted as “dissipative structures” and include rate oscillations, spatiotemporal patterns and chaos.[1-2] The formation of these phenomena is often attributed to the interplay of rapid chemical reaction steps and relatively slow complementary processes such as adsorbate-induced surface reconstructions or oxide formation.[3]

In heterogeneous catalysis this phenomenon was first reported for CO oxidation over Pt metal catalysts.[4-5] Since then, the investigations of oscillations have become a very active research field which now includes NO reduction,[6-7] CO oxidation,[8] NH_3 oxidation[9] and hydrogen oxidation.[10] Despite constant external conditions, such as gas pressure, flow rate and temperature, product formation and reactants

consumption vary periodically in these reactions. Apart from the found oscillations of the reaction rates, many types of spatiotemporal patterns have also been observed.

The first detailed investigation of surface oscillatory kinetics was done by Ertl et al.[11] The authors showed that oscillations in CO oxidation on Pt (001) are connected to adsorbate-induced surface reconstructions. Ertl and co-workers also demonstrated the presence of spatial surface patterns in the same reaction by using scanning low-energy electron diffraction (LEED).[12-13] Based on these ground-breaking works, a plethora of related studies followed.[1, 14] For instance, a dynamic platinum surface was observed by *in situ* transmission electron microscopy (TEM) which was coupled to a mass spectrometer. This can be expressed by a reversible surface faceting and could be correlated to CO_2 oscillation in the catalytic CO oxidation.[15] In addition, for palladium as a CO oxidation catalyst, *in situ* X-ray diffraction (XRD) measurements indicated that the oscillation of the oxidic state is coupled to a fluctuating CO_2 formation rate which was detected by on-line mass spectrometry.[16] Thus, the combination of different *in situ* techniques and mass spectrometry can be considered as a valuable tool to unravel real time surface information that is coupled to changes of the reaction rates.

These so-called self-sustained oscillations can be observed for different heterogeneous catalytic reactions.[1, 17-18] Chaotic, sinusoidal or harmonic oscillations can be formed depending on the different feedback mechanism. Furthermore, relaxation-type oscillations, which can be described as a fast transformation between low-active and high-active states lead to a continuous decrease and increase of the reaction rate, respectively. Relaxation-type oscillations have been, for instance, observed in the investigation of propane oxidation over Ni surfaces in a mbar pressure regime.[19-23] Applying near-ambient-pressure X-ray photoelectron Spectron (NAP-XPS) combined with a mass spectrometer (MS) and gas chromatography (GC) a reversible transformation of the metallic Ni surface to NiO has been documented. These electronic surface changes are accompanied by alterations of the catalytic activity. To fully understand these morphological fluctuations spatial resolution is mandatory.

Here we will use a catalytic model reaction, i.e. the oxidation of hydrogen, to provide more information about the surface dynamics under reaction conditions of Ni foams.

Dynamics of the surface morphology will be recorded by *in situ* SEM imaging which can be directly correlated to differences in the gas phase composition. Therefore, a QMS device was attached at the gas outlet. Temperature variations are tracked by adding thermal couples into the Ni foam. Thus, morphologies, image intensities and temperatures of the catalyst can be gathered simultaneously as well as *in situ* and can be correlated to the H_2 oxidation reaction rate. The experiments allow for a direct measure of the surface dynamics of a catalyst during periodic changes of the reaction rate.

4.3 Experimental section

H_2 oxidation reactions were performed on Nickel foam substrates, purchased from Recemat BV Ltd. The Ni foam was cut to 1 mm thick disc with a diameter of 4 mm. *In situ* experiments were performed inside the chamber of a commercial environmental scanning electron microscope (FEI Quantum 200), which is equipped with a customized laser heating stage and a mass spectrometer (Pfeifer Omnistar) for chamber atmosphere analysis. The temperature is measured using K-type thermocouples that are inserted into the nickel foam. The Ni morphological evolutions under reaction conditions were imaged by Large-Field-Detector (LFD) with an acceleration voltage of 7.5 kV. SEM images were recorded at different scan speeds, ranging from 8.5 to 35.4 seconds per frame. The H_2 and O_2 gasses were introduced into the ESEM chamber from a modified gas line. Prior to measurements, the Ni foam were annealed at 700 °C in H_2 flow of 10 ml/min at chamber pressure of 0.2 mbar for 60 mins.

For the H_2 oxidation experiments, the O_2 feed was increased in steps of 0.25 ml/min as indicated in Figure 4.2, while keeping the H_2 flow fixed at 10 ml/min. The chamber pressure during the experiments ranged from 0.2 to 0.5 mbar. No electron-beam-induced contamination was observed at high temperatures.

Quantitative analysis to extract brightness intensities from *in situ* SEM images was performed using Image J software. The total brightness intensities were acquired from integration on the region of interest in a SEM image with the Time series analyser Plugin.

The time delay caused by the gas diffusion from the chamber to the mass spectrometer was calibrated using defined pulses of H_2 and O_2 and measure the

time between observing changes in the images contrast cause by a change of the imaging gas properties till the added gas was detected by the MS.

4.4 Results

4.4.1 Sample pre-treatment

The nickel foam is mounted on the sample holder manufactured from silicon carbide (Figure 4.1A). All Ni samples were annealed at 700 °C in 10 ml/min of H_2 at a chamber pressure of 0.2 mbar for 1 hour to remove contaminants and surface oxide layers. Figure 4.1B shows the surface morphology before the reduction in hydrogen atmosphere. Here, the surface appears rough indicating the presence of some contaminants and nickel oxides. After annealing in hydrogen atmosphere, the nickel surface smoothens and individual grains can be determined (Figure 4.1C).

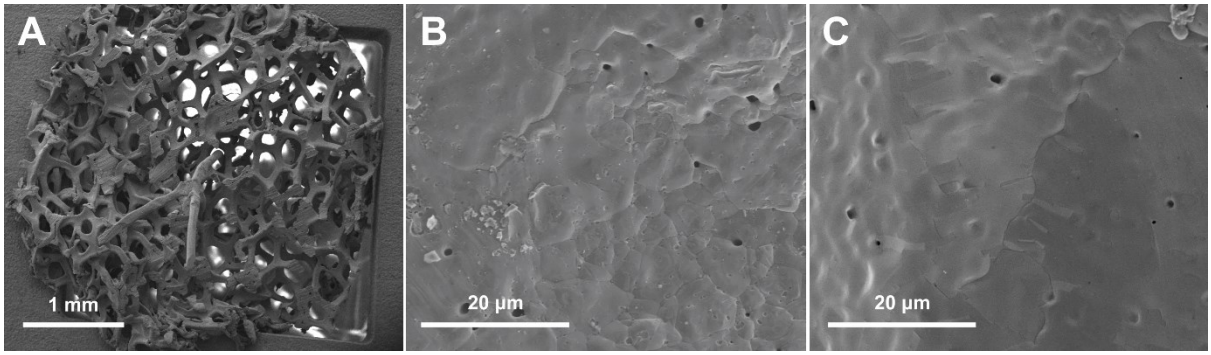

Figure 4.1 ESEM images of Ni substrates used in the study of catalytic H_2 oxidation: A) Ni foam mounted on the ESEM sample holder; B) surface of the Ni foam before hydrogen treatment; C) surface smoothening after hydrogen annealing at 700 °C for 1 hour.

4.4.2 Catalytic reactions at constant laser power output

During the hydrogen oxidation experiments, the backside of the nickel sample was heated by a laser beam. The output current of the laser was kept constant at 17.0 A. The hydrogen mass flow was fixed at 10 ml/min, while the oxygen content was increased stepwise from 0 ml/min to 2.65 ml/min in steps of 0.25 ml/min, which led to an increase of the pressure from 0.2 to 0.5 mbar (Figure 4.2).

Figure 4.2A represents the H_2 (blue line), O_2 (red line) and H_2O (black line) ion currents with increasing oxygen content. At low O_2 flows (0.5 ml/min to 1.0 ml/min) no oscillations have been detected. At an oxygen flow of 1.25 ml/min the mass traces that correspond to H_2 and O_2 and the product H_2O start to oscillate. It shall be

noted that the reactants O_2 and H_2 oscillate in-phase, while H_2O exhibits an anti-phase oscillation behaviour compared to the ion currents of the reactants. Here, the minimum of the H_2 and O_2 traces parallels the maximum of water formation and vice versa.

A more quantitative expression of Figure 4.2A is given in Figure 4.2B. Here, the amplitude and frequency of H_2O oscillations with increasing O_2 mass flow are analysed by fast Fourier transform (green line). For comparison the black line with solid square and hollow circles (Figure 4.2B) represents the measured maximum and minimum of the H_2O ion currents at different oxygen contents. With increasing O_2 flows from 1.25 ml/min to 2.25 ml/min the H_2O maximum and minimum increases (black line in Figure 4.2B). In this regime the amplitude of H_2O oscillation is proportional to the O_2 concentration. At a higher oxygen content (2.25 ml/min to 2.65 ml/min) the maximum of hydrogen production levels off, while the corresponding minimum decreases (black line Figure 4.2B). The oscillation frequency also changed with the O_2 concentration as depicted by the Fourier analysis (green line in Figure 4.2B). The frequency increased from 0.065 cycles/min at a O_2 set point of 1.25 ml/min to 0.137 cycles/min at an O_2 flow of 2.0 ml/min. Subsequently, the frequency starts to decay to 0.105 cycles/min at higher flows of 2.65 ml/min. The change of the frequency can further be corroborated by Figure 4.2A (H_2O black line) in which the oscillation densifies from increasing the O_2 flow from 1.25 ml/min to 2.0 ml/min and expands for higher flows.

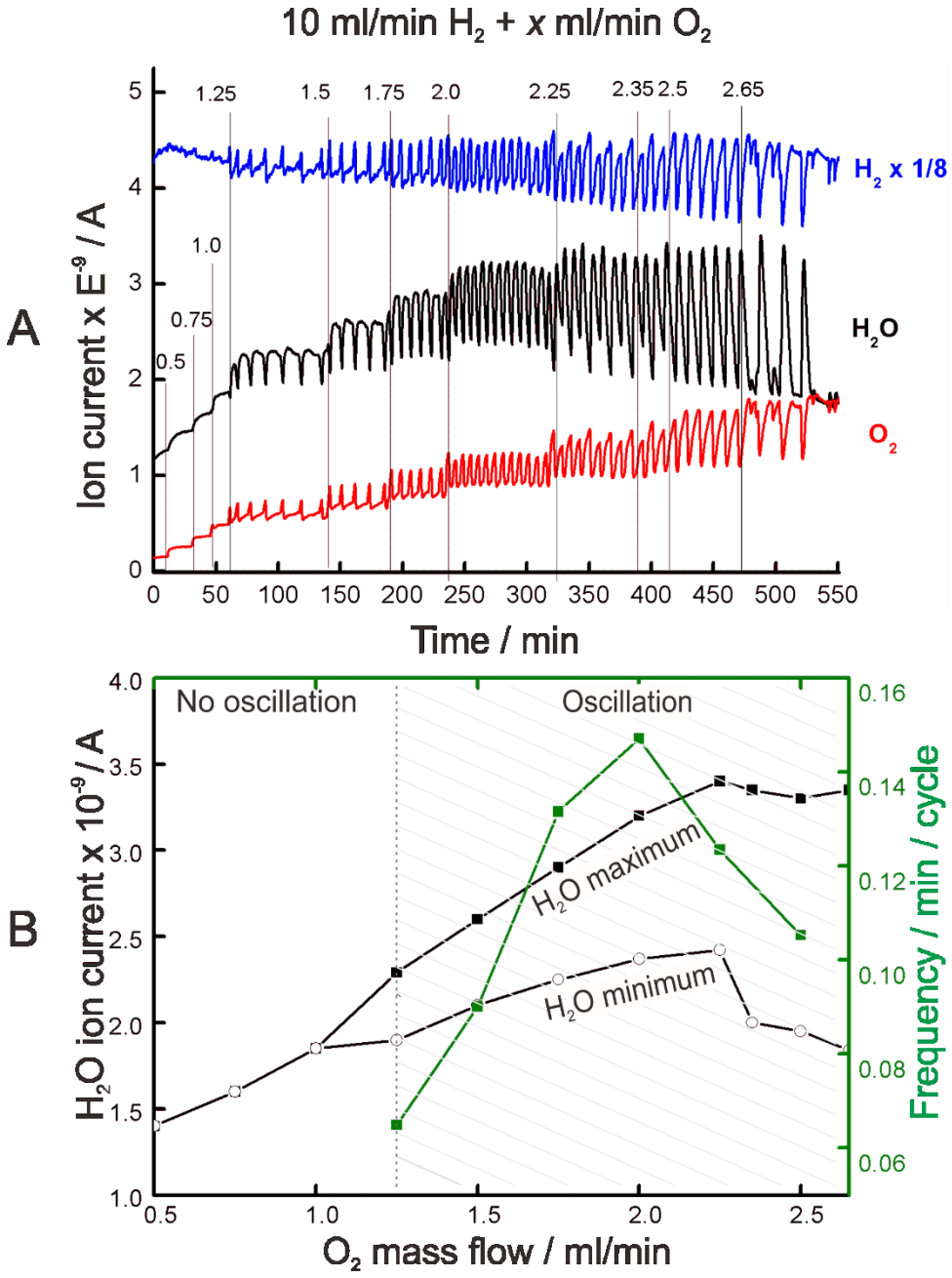

Figure 4.2 A) Product traces of the H_2 oxidation reaction over a Ni foam at various O_2 concentrations. The H_2/O_2 ratio ranges from 10/0.5 to 10/2.65. The corresponding values are written on the top in ml/min. The O_2 concentration in the reaction mixture varies from 4.76 to 20.95%. The MS signal of H_2 is vertically adjusted by a factor shown in the legend. B) semi-quantitative analysis of A): The dashed line separates the oscillation regime. The black curve with solid squares and hollow circles displays the H_2O maximum and minimum at different oxygen mass flows. The green curve demonstrates the variations of the H_2O frequency for different oxygen contents. The laser output current and the H_2 mass flow were kept constant at 17.0A and 10 ml/min, respectively.

As we will show the mass traces of H_2, O_2 and H_2O act as a feedback loop, for synchronized Ni surface dynamics. Details of the gas phase variation and surface evolution will be discussed in the sections 4.2.2.1 to 4.2.2.3. For this discussion three different oxygen mass flows (1.25 ml/min/ 11%, 1.75 ml/min/ 15% and 2.5 ml/min/ 21%) were selected which represent oxygen-lean, oxygen-medium and oxygen-rich conditions. For each O_2 ratio two entire oscillation cycles are highlighted.

The discussion of each ratio will include O_2 and H_2O oscillations. As H_2 and O_2 mass traces showed the same oscillation tendency (compare Figure 4.2A; blue and red line) the following discussion will concentrate on the O_2 ion current. In addition, the 1st derivative of the H_2O signal, which corresponds to the H_2O production rate, will also be presented. Furthermore, as a response to the changes of the gas phase, the nickel surface shows morphological dynamics, which have been recorded by *in situ* SEM. From each of these images the intensity values are extracted and presented. Furthermore, representative SEM snapshots of the Ni surface which correspond to high and low water production are shown. Finally, the temperature variations can give feedback of the H_2O production. The temperature fluctuations are attributed to the high exothermicity of the H_2 oxidation reaction (equation 4-1): the surface. The authors suggested an O disproportionation reaction,

$$H_2\,(g) + 1/2O_2\,(g) \rightarrow H_2O\,(l) \quad \Delta H = -571.7\ kJ/mol \qquad (4\text{-}1)$$

Since the laser output current was maintained constant at 17.0A during the increase of the oxygen content the observed temperature fluctuations can be attributed to the energy released or consumed by the production of water. Thus, the temperature can be an additional measure to conclude on high-active and low-active states.

4.4.2.1 Oxygen mass flow at 1.25 ml/min

Figure 4.3 shows an excerpt of the MS signals presented in Figure 4.2, the corresponding temperature pattern and the evolution of the SEM image intensities recorded at different times at a constant H_2:O_2 ratio of 10:1.25. The ion currents of O_2 (red line) and H_2O (black line) oscillate in anti-phase. In the same graph the 1st derivative of the H_2O signal is highlighted (blue line), which corresponds to the H_2O production rate and coincides well with the temperature oscillation waveform presented in Figure 4.3 (pink line). The coincidence of the oscillating waveforms between the H_2O production rate (Figure 4.3, blue line) and temperature (Figure 4.3, pink line) reflects well the heat of the H_2 oxidation reaction. A sharp decrease and increase in temperature (pink line) mark the ascent and descent of the H_2O

production (blue line). Furthermore, the nickel surface is also dynamic. The surface morphological changes have been recorded in real-time by *in situ* SEM imaging during the reactions and are characterized by periodic intensity changes. These intensities values were extracted from the *in situ* SEM images (videos S4.1) and are plotted in Figure 4.3 (green line).

Periodic intensity changes of the morphology of the Ni catalyst between smooth to rough surfaces were observed during the oscillation (green line in Figure 4.3 & Video S4.1) that are characterized by different intensities. For further specification snapshots of the nickel surface morphology that corresponds to different points (dashed lines A to D) of the H_2O production (black line) are presented in Figure 4.4. As can be seen in the corresponding intensity plot of Figure 4.3 (green line) and from the SEM images in Figure 4.4 the nickel surface state responds to the situation of high and low water production, which defines high- and low-active states. The SEM image recorded at 85.768s shows a situation of the catalyst in its high-active state featuring relative smooth surfaces and dark contrast (Figure 4.4A). This corresponds to a maximum in the H_2O production rate (Figure 4.3, black line). At the end of the high-active state a flickering of the intensity values which is expressed by the appearance and disappearance of bright nanoparticles on the Ni surface can be observed in Video S4.1 from 86.620 s to 89.744s. This observation corresponds to the onset of the decay of the H_2O production rate (Figure 4.3, black line) and an increase of the SEM intensity (Figure 4.3, green line). This flickering represents a dynamic competition between the oxidation and reduction of the Ni surface. The competition ends with more and more bright particles at 89.744 s (Figure 4.4B). Subsequently, the surface starts to become rough which is accompanied by the appearance of some bright particles on the surface that continue to grow and cover the entire surface (Figure 4.4C), while at the same time (90.596 s) the H_2O production rate (Figure 4.3, black line) reaches a minimum. Consequently, the surface has reached its low-active state which is manifested by the maximum of the SEM intensity (Figure 4.3, green line). During the prevailing time of the catalytic reaction, the bright particles disappear and the surface returns to its initial smooth and dark character (Figure 4.4D) after a reaction time of 93.436 s. Details are available in the supplementary Video S4.1.

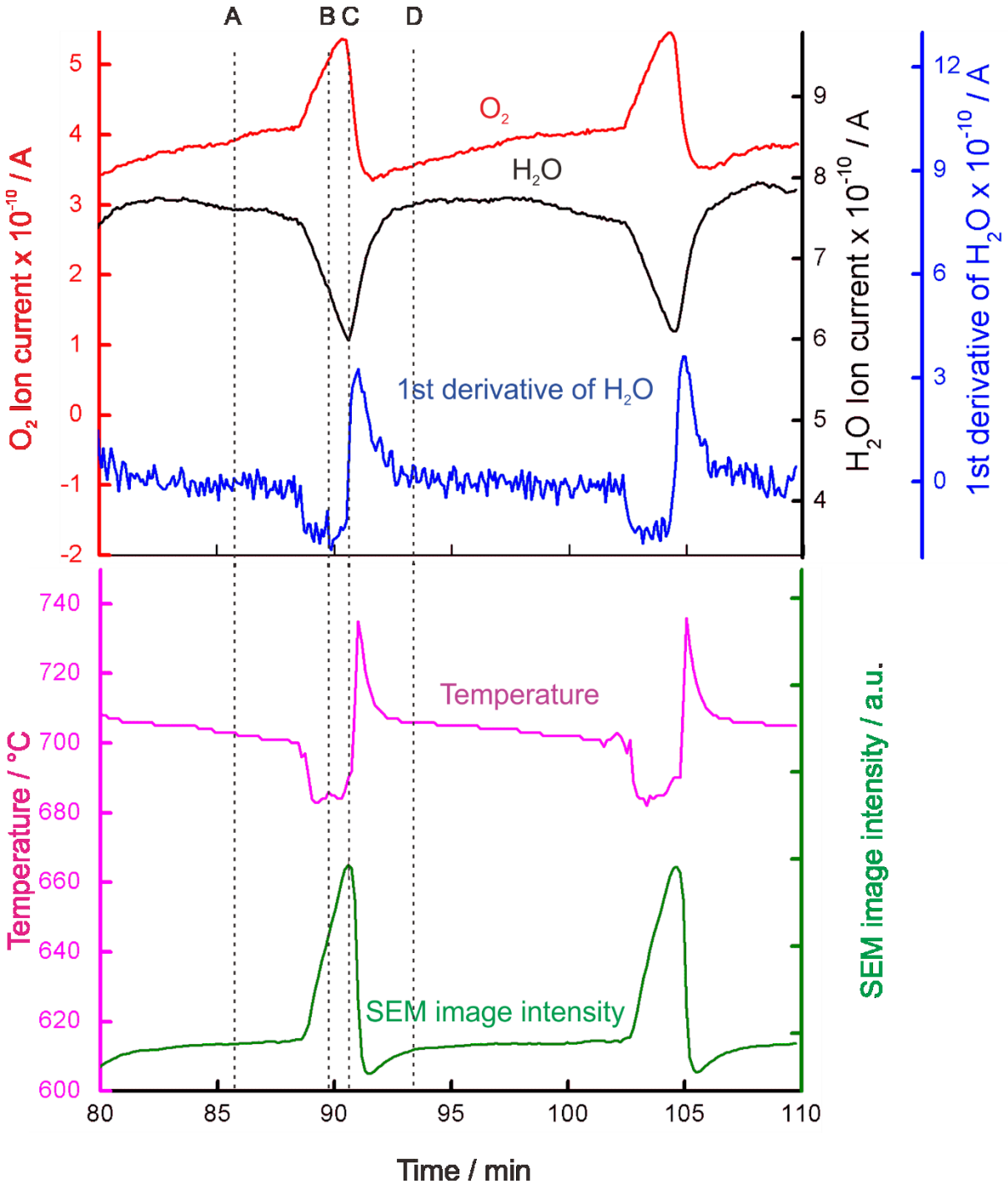

Figure 4.3 MS signals collected during hydrogen oxidation reactions over Ni catalyst for H_2:O_2 =10:1.25. O_2 and H_2O ion current oscillations are plotted with time (red and black line). The first derivative of H_2O MS signal is displayed by a blue line. Temperature oscillations (pink line) and brightness intensities from the in situ SEM images (green line) are given in the bottom graph. Dashed lines A, B, C and D indicate reaction times of SEM snapshots presented in Figure 4.4.

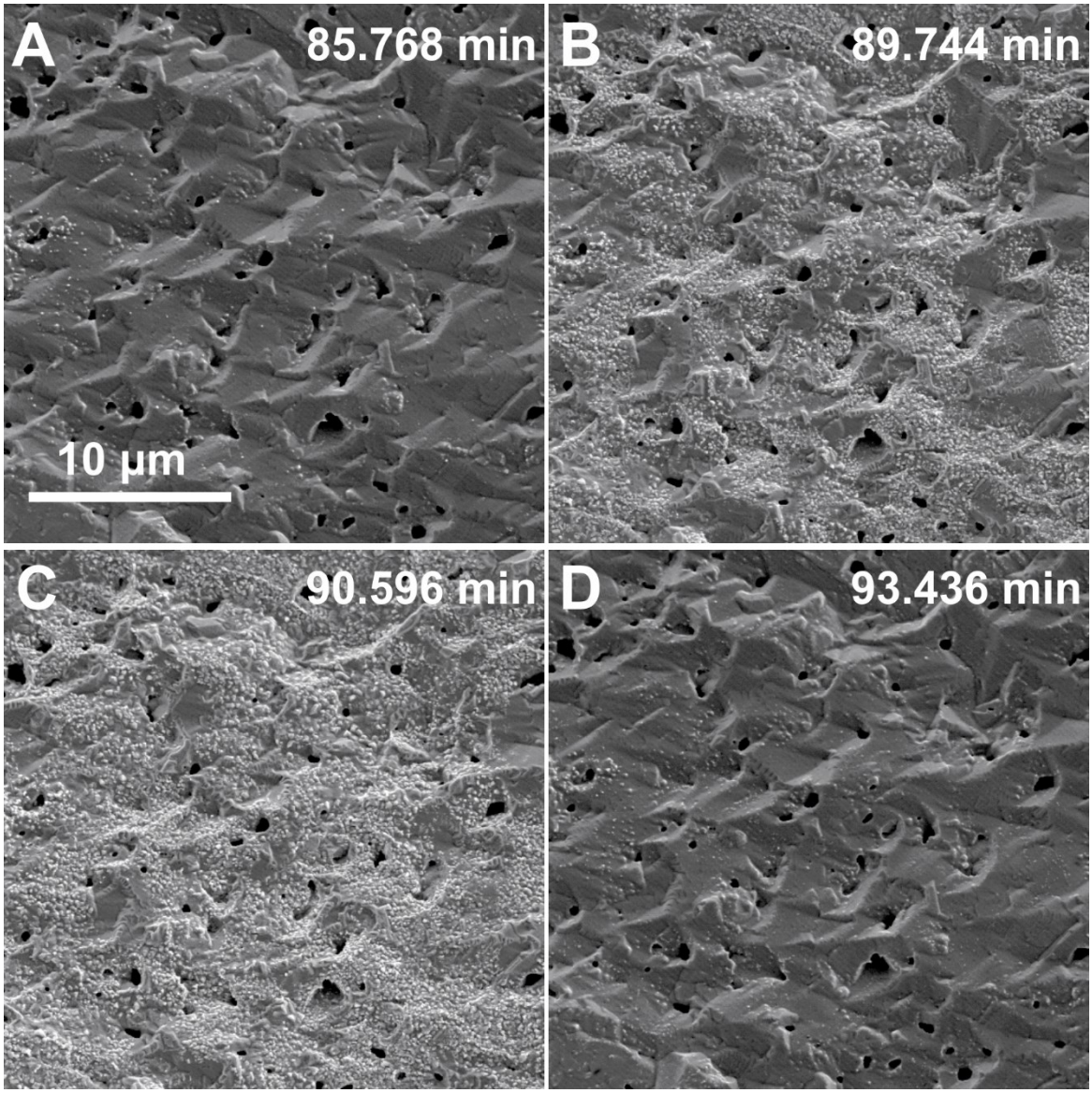

Figure 4.4 SEM images of the evolution of the nickel surface at different reaction times (H_2:O_2 =10:1.25). The labeling corresponds to times highlighted by A, B, C, and D in Figure 4.3. The complete surface dynamics are presented in Video S4.1.

4.4.2.2 Oxygen mass flow at 1.75 ml/min

Figure 4.5 presents analytical results obtained with an increased O_2 content of H_2:O_2 = 10:1.75. Again, the H_2O signal (black line) oscillates in anti-phase with the O_2 waveforms (red line) and the SEM intensity (green line). In addition, the progression of the 1st derivative of the H_2O signal (blue curve) parallels the temperature graph (pink line). This behaviour is similar to the situation at H_2:O_2 = 10:1.25 which was discussed in section 4.2.2.1. The following discussion will mainly focus on new features which are observed when the oxygen flow is increased from 1.25 ml/min to

1.75 ml/min at reaction times between 195.818 s (marked by A) and 202.776 s (marked by D).

Furthermore, SEM image sequences of the nickel surfaces recorded under these conditions indicate a morphological behaviour which correlates to the observed gas phase changes (Figure 4.6). Similar to the observations presented in Figure 4.4, the initial nickel surface is relatively dark and smooth (Figure 4.6A). This correlates to a H_2O production rate (Figure 4.5, black line) indicating a high-active state at 195.818 s. Subsequently, bright particles (Figure 4.6B) occur at the surface which lead to an increase of the image intensity (Figure 4.5, green line). These morphological features occur at the onset of the decay of the H_2O production (Figure 4.5, black line) at 198.374 s. As opposed to the similar situation presented in Figure 4.4B for an oxygen flow of 1.25 ml/min, additional triangular structures arise that are around 1-2 µm in size and can coexist with the bright particles (Figure 4.6B). The triangular structures exhibit smooth surfaces and are characterized by a darker contrast. The intensity of the SEM images increases and the triangular structures grow (Figure 4.6C) until a reaction time of 199.794 s (Figure 4.5, green line). This maximum in the SEM image intensity corresponds to the minimum of the water production rate (Figure 4.5, black line) indicating the advent of a low-active state. These structures disappear and the surface morphology returns to its initial darker and smoother appearance at a reaction time of 202.776 s (Figure 4.6D). This leads to a decrease of the SEM intensity (Figure 4.5, green line) and to a maximum in the H_2O production (Figure 4.5, black line) suggesting the reversible kinetic transformation of the catalyst surface into its high-active state.

Similar to the situation presented in Video S4.1, for this H_2:O_2 ratio flickering was also observed at the high-active/ low-active state transition (Video S4.2). This flickering of the Ni surface is reflected in the intensity fluctuation (Figure 4.5, green line, dotted circle). At this transition state, the Ni substrate exhibits surface turbulences in which the bright nanoparticles competitively and chaotically appear and disappear (Video S4.2). However, the flickering could neither be observed in the O_2 (Figure 4.5, red line) and H_2O (Figure 4.5, black line) ion currents nor in the sample temperature (Figure 4.5, pink line). Further details about the surface dynamics are available in Video S4.2.

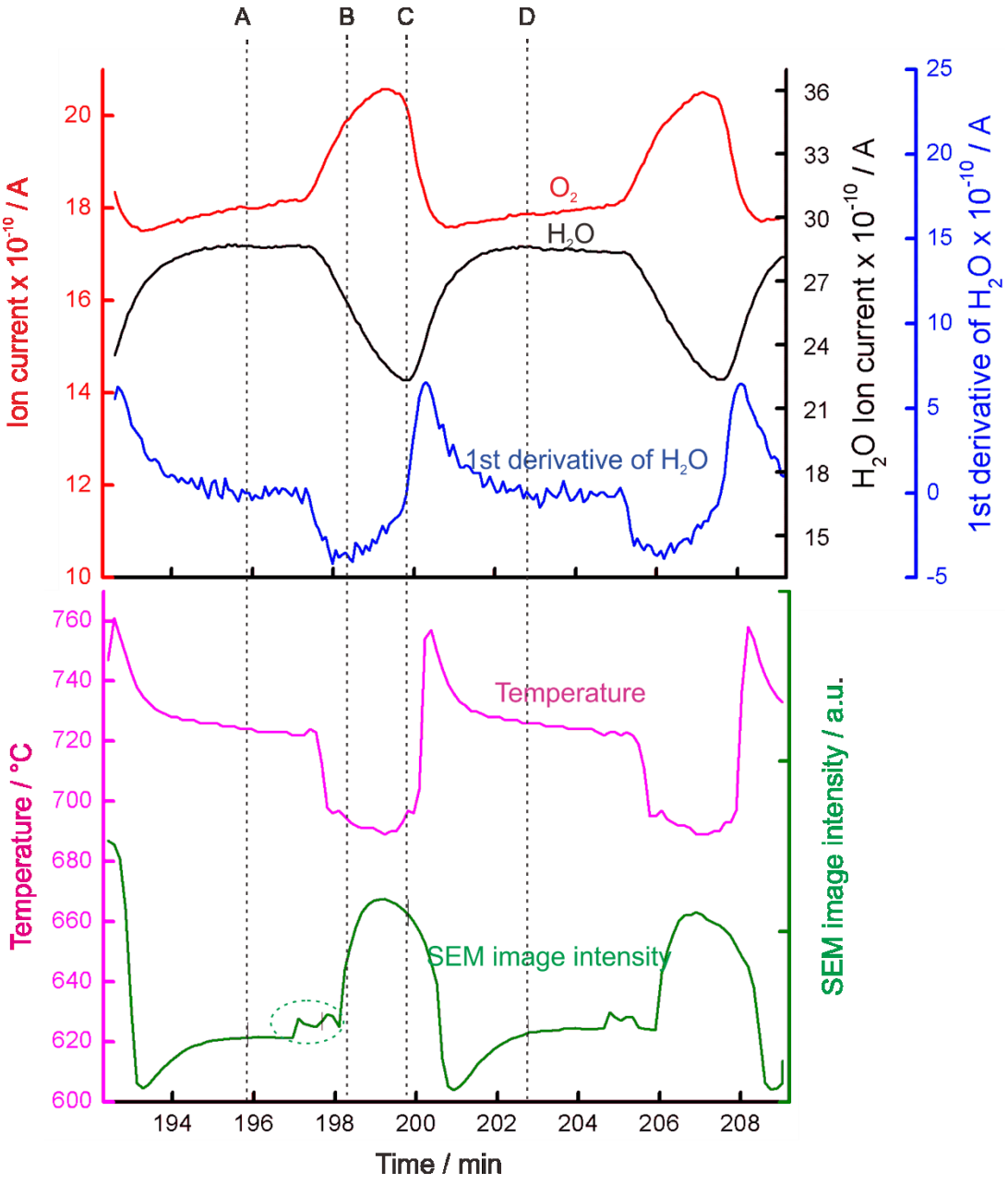

Figure 4.5 MS signals collected during hydrogen oxidation reactions over Ni catalyst for H_2:O_2 = 10:1.75. O_2 and H_2O ion current oscillations are plotted with time (red and black line, respectively). The first derivative of H_2O MS signal is displayed by a blue line. Temperature oscillations (pink line) and brightness intensities from the in situ SEM images (green line) are given in the bottom graph. Dashed lines A, B, C and D indicate reaction times of SEM snapshots presented in Figure 4.6.

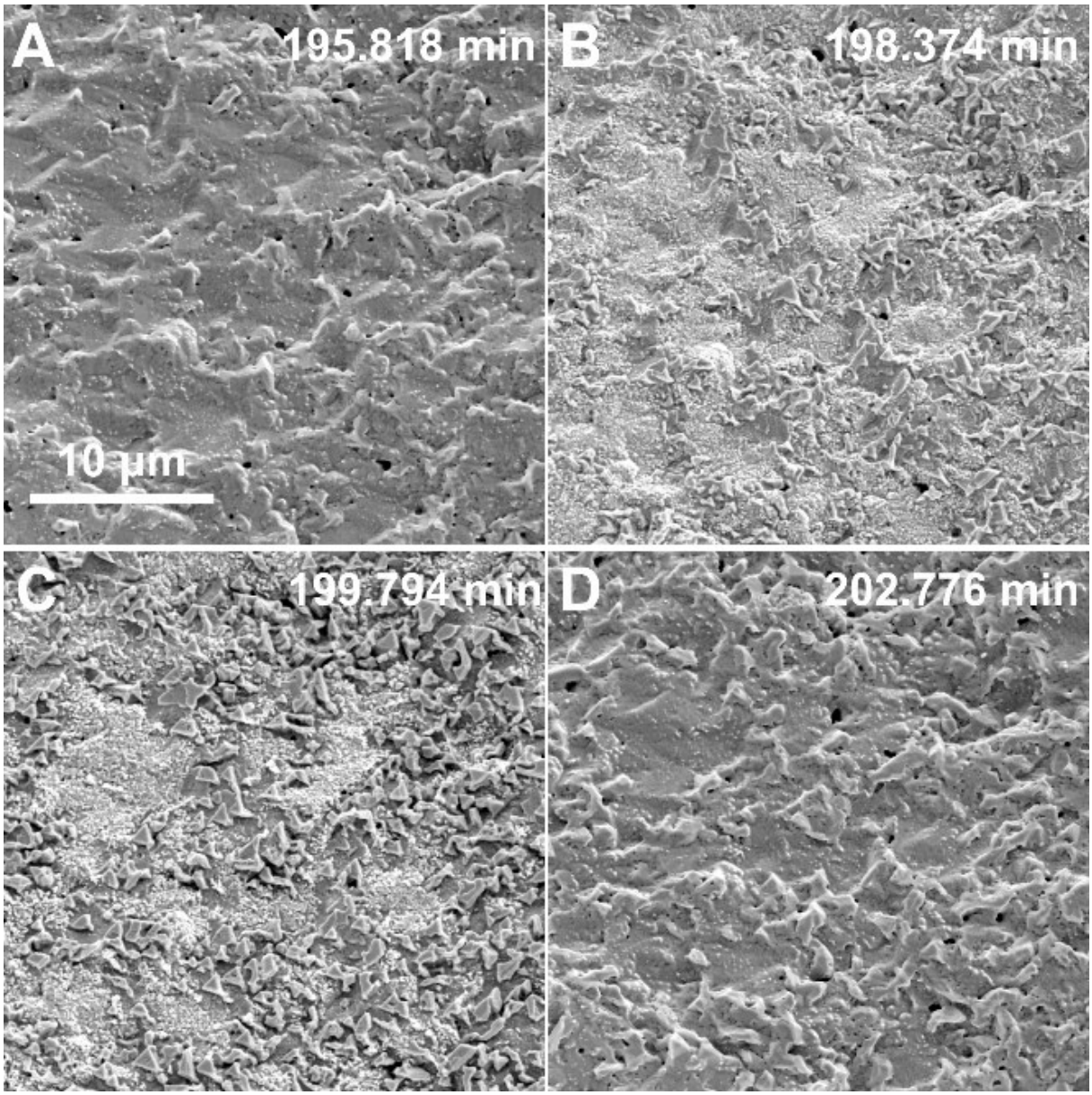

Figure 4.6 SEM images of the evolution of the nickel surface at different reaction times (H_2:O_2 = 10:1.75). The labeling corresponds to times highlighted by A, B, C, and D in Figure 4.5. The complete surface dynamics are presented in Video S4.2.

4.4.2.3 Oxygen mass flow at 2.5 ml/min

After further increasing the oxygen content, the tendencies of the gas phases oscillations differ from the previous observation. Figure 4.7 presents oscillation profiles at a reaction mixture of H_2:O_2 = 10:2.5. The O_2 (red line), H_2O (black line) and temperature (pink line) profiles demonstrate a sharp transition between high activity and low activity state, with a reaction maximum at 441.620 s (dashed line A)

and minimum at 449.288 s (dashed line C). As opposed to previous temperature profiles, the temperature curve (Figure 4.7, pink line) shows a linear decay and follows the H_2O production rate (Figure 7, black line) rather than the 1st derivative of water production (Figure 4.7, blue line). The absence of plateaus in the kinetic oscillations indicates a certain chemical instability of the catalyst under high O_2 flow 2.5 ml/min. Due to the positive entropic term of the Gibbs-Helmholtz equation Ni catalyst are prone to oxidation at high temperatures at higher O_2 frugalities (compare Ellingham diagram)[25].

As a feedback to the observed gas phase oscillations (Figure 4.7), SEM images of the Ni catalyst surface display periodic dynamics (Figure 4.8 and Video S4.3). The nickel surface shows dark contrast (Figure 4.8A) that corresponds to a maximum of the H_2O production (Figure 4.7, black line) at 441.620 s. The subsequent decay of the H_2O production (Figure 4.7, black line) is accompanied by the consecutive occurrence of flickering and the emergence of dynamical changes of faceted particles (Video S4.3). A snapshot of this situation is presented in Figure 4.8B and shows the transition of the high-active to the low-active Ni surface morphology (see H_2O production (Figure 4.7, black line) at 445.170 s). The oxidation of the surface increases the surface intensity (Figure 4.7, green line) and the H_2O production (Figure 4.7, black line) decreases. Figure 4.8C shows the surface morphology at the low-active state. At 449.288 s, The H_2O production (Figure 4.7, black line) reaches a maximum which occurs with a sharp peak (Figure 4.7, dotted line D) in the image intensity (Figure 4.7, green line). Here the surface is reduced as represented by the dark contrast of the SEM image shown in Figure 4.8D, while H_2O production reached maximum at 451.702 s (dashed line D).

Gas phase oscillations and surface dynamics are closely related with each other during the hydrogen oxidation reactions. In general, high-active surfaces appear dark and corresponds to, low O_2 ion currents, a high H_2O production rate and a high temperature. In contrast, low-active surfaces are bright, and the gas phase exhibit a high O_2 ion current, low H_2O production rate and the temperature is low.

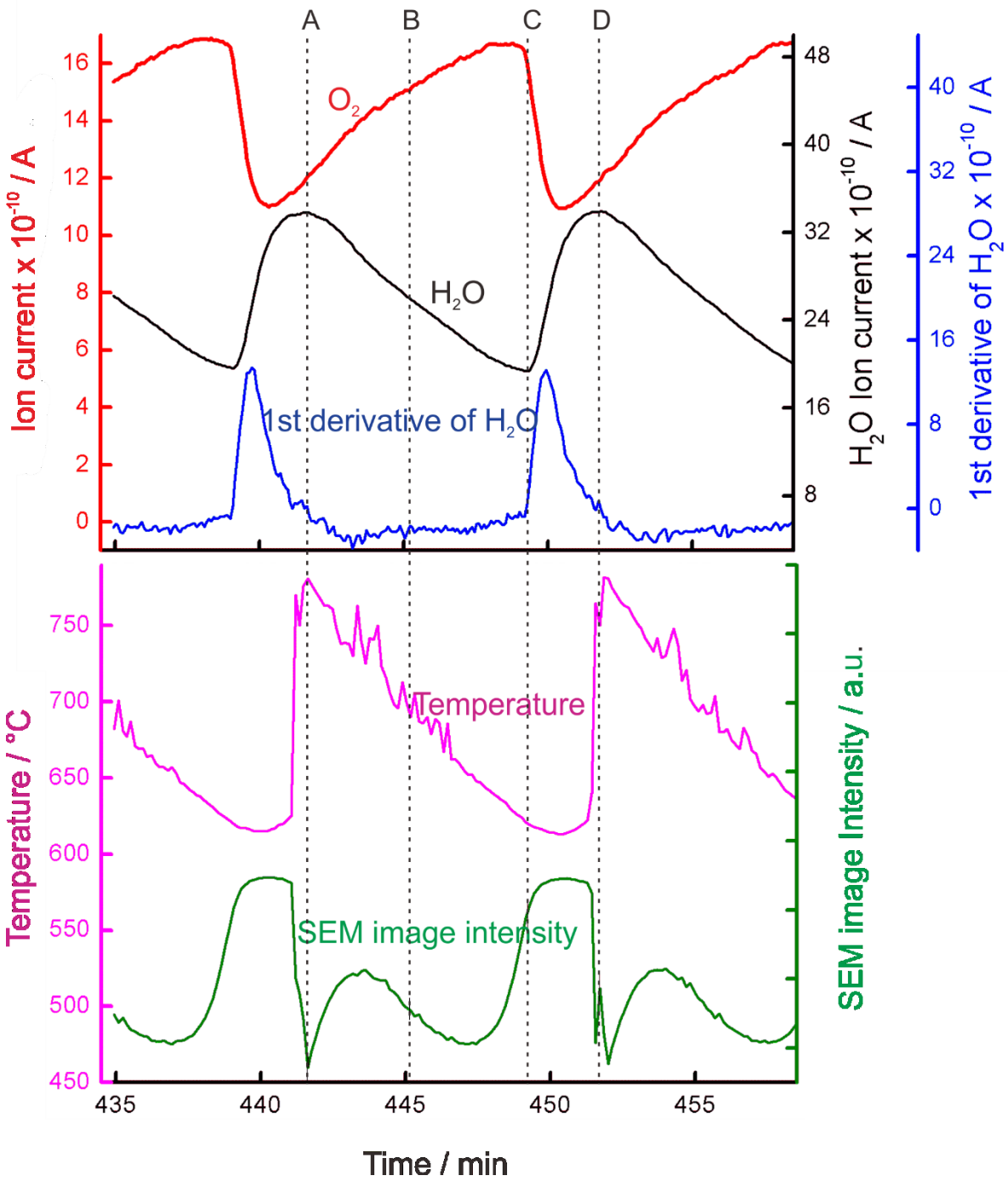

Figure 4.7 MS signals collected during hydrogen oxidation reactions over Ni catalyst for H_2:O_2 = 10:2.5. O_2 and H_2O ion current oscillations are plotted with time (red and black line, respectively). The first derivative of H_2O MS signal is displayed by a blue line. Temperature oscillations (pink line) and brightness intensities from the in situ SEM images (green line) are given in the bottom graph. Dashed lines A, B, C and D indicate reaction times of SEM snapshots presented in Figure 4.8.

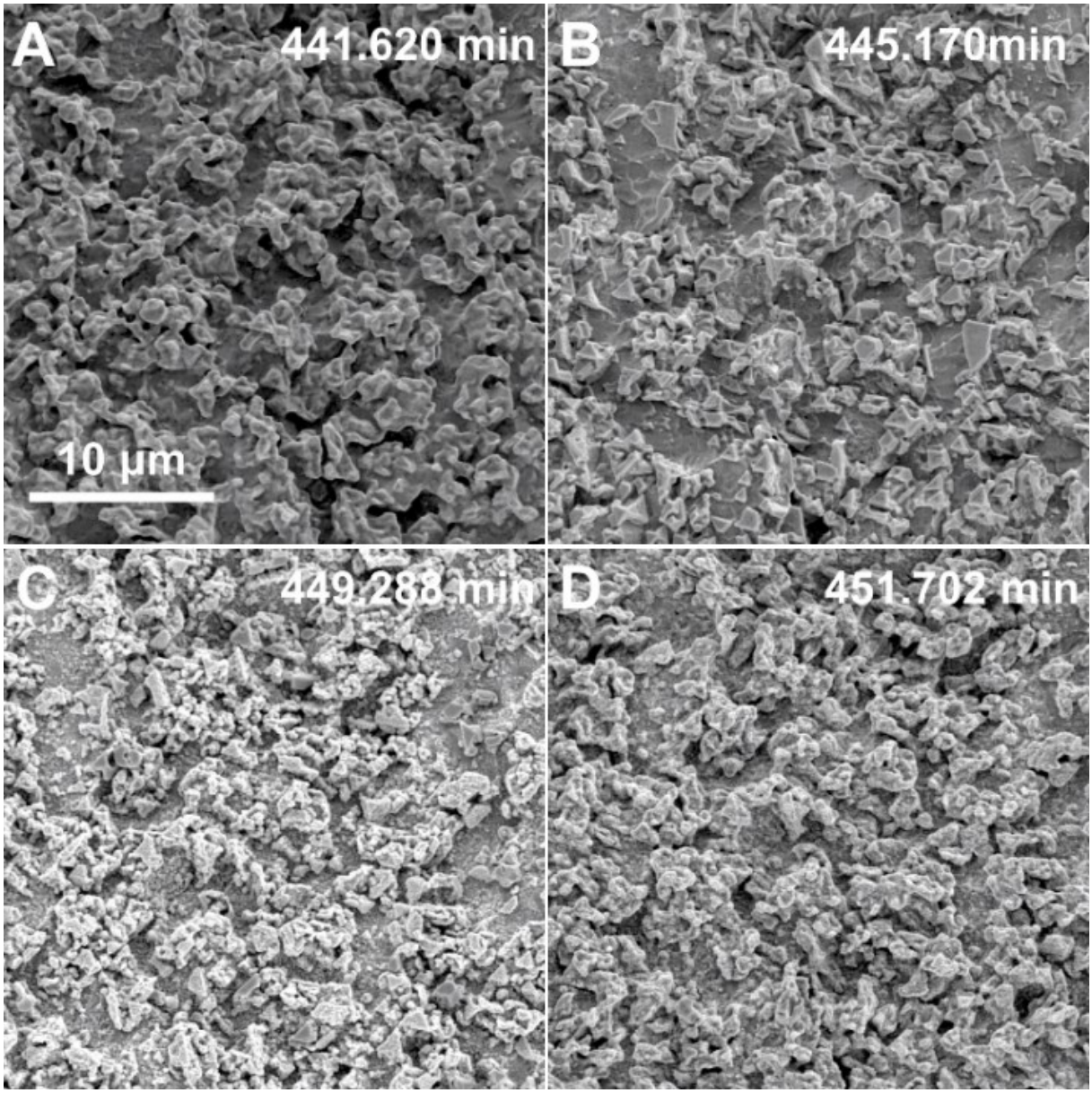

Figure 4.8 SEM images of the evolution of the nickel surface at different reaction times (H_2:O_2 = 10:2.5). The labeling corresponds to times highlighted by A, B, C, and D in Figure 4.7. The complete surface dynamics are presented in Video S4.3.

4.4.3 Comparison of nickel morphologies at different H_2 and O_2 ratios

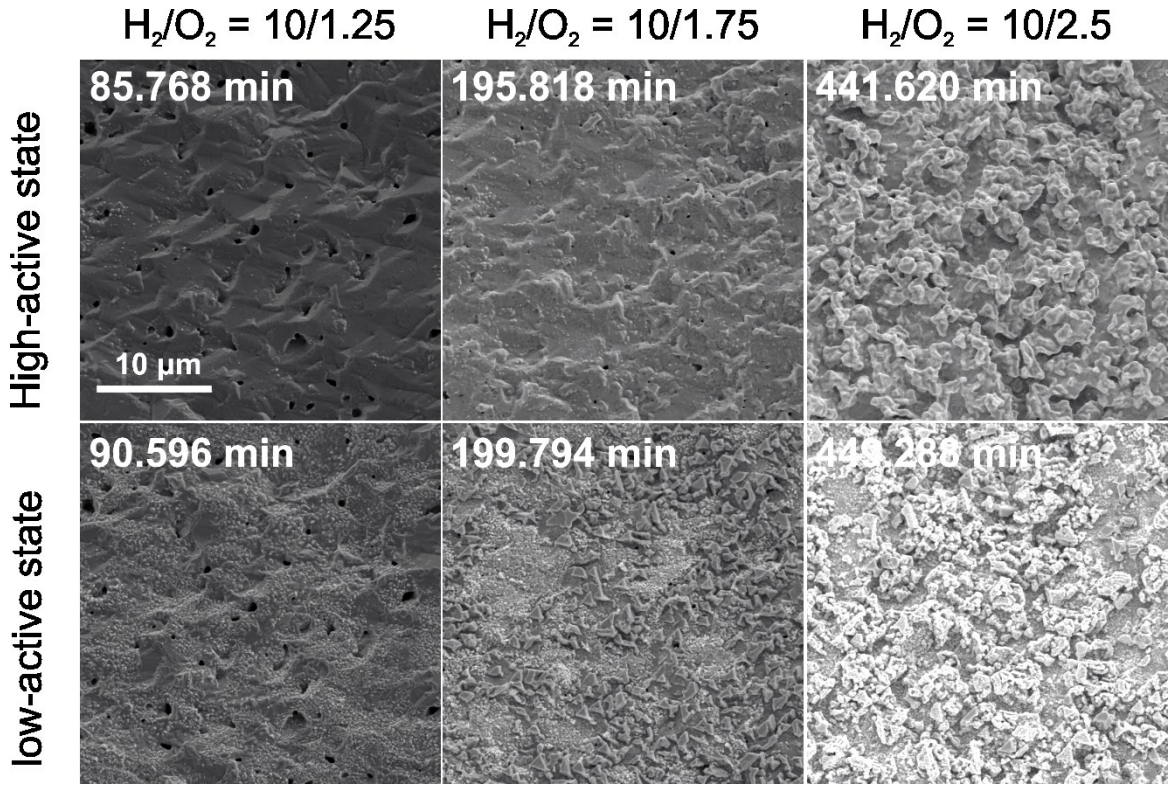

Figure 4.9 in situ SEM images comparison for high and low-active states at different H_2/O_2 flow ratios H_2/O_2 of 10/1.25 (11%), 10/1.75 (14.9%) and 10/2.5 (20%).

Figure 4.9 summarizes the influence of the O_2 content on the morphology of the Ni surface during the H_2 oxidation reactions. In this study SEM images of a high-active surface are characterized by a darker contrast (top row) compared to the brighter low-active state (bottom row). This finding is independent of the gas ratio. It is apparent that at high-active states the nickel surface evolves from smooth static metallic surfaces at a H_2/O_2 ratio of 10/1.25 to rough surfaces at a H_2/O_2 ratio of 10/2.5. The low-active Ni catalyst exhibits rough surfaces with bright particles at a H_2/O_2 ratio of 10/1.25. They transform into surfaces where bright particles and triangular structures can coexist at a H_2/O_2 ratio of 10/1.75 and into heavily oxidized surfaces at a H_2/O_2 ratio of 10/2.5. In summary, with the increasing O_2 content from 11% to 20% (O_2 from 1.25 to 2.5 ml/min), the Ni surface became rough and developed more morphological features.

4.4.4 The effect of temperature on the kinetic oscillations

For further insights on the kinetic oscillation of the hydrogen oxidation reaction, experiments were performed at different temperatures with a fixed and medium H_2/O_2 ratio of 10/1.75 (14.9% of O_2 in H_2). Figure 4.10A presents the corresponding temperature dependent gas phase variations, including H_2 (blue line), O_2 (red line) and H_2O (black line) ion currents over Ni catalyst. The temperature was stepwise increased from 350 °C to 800 °C. As can be seen from Figure 4.10A kinetic oscillations were spotted in the temperature regime between 550 °C to 800 °C. No oscillations were detected below 550 °C and above 850 °C. The ion currents of H_2 (blue line) and O_2 (red line) proceed in-phase, while the H_2O production rate (red line) oscillates anti-phase. Overall the reaction rate increases with temperature as indicated by the increase of the H_2O ion current and simultaneous decrease of the H_2 and O_2 mass traces. Figure 4.10B shows the H_2O oscillation frequencies of Figure 4.10A between 550 °C and 750 °C. With increasing temperatures the frequencies of the H_2O oscillation increases, whereas the amplitude of oscillations decrease from 9.98 x 10^{-9} cycles/min at 550 °C to 1.41 x 10^{-9} cycles/min at 750 °C. The positive relationship between the oscillation frequency and the temperature suggests that the nickel catalyst spends more time in its high-active and metallic state at higher temperature. The increase in frequency with higher temperatures is in agreement with the report of Zhang et al[26] on the partial oxidation of methane over Ni catalyst.

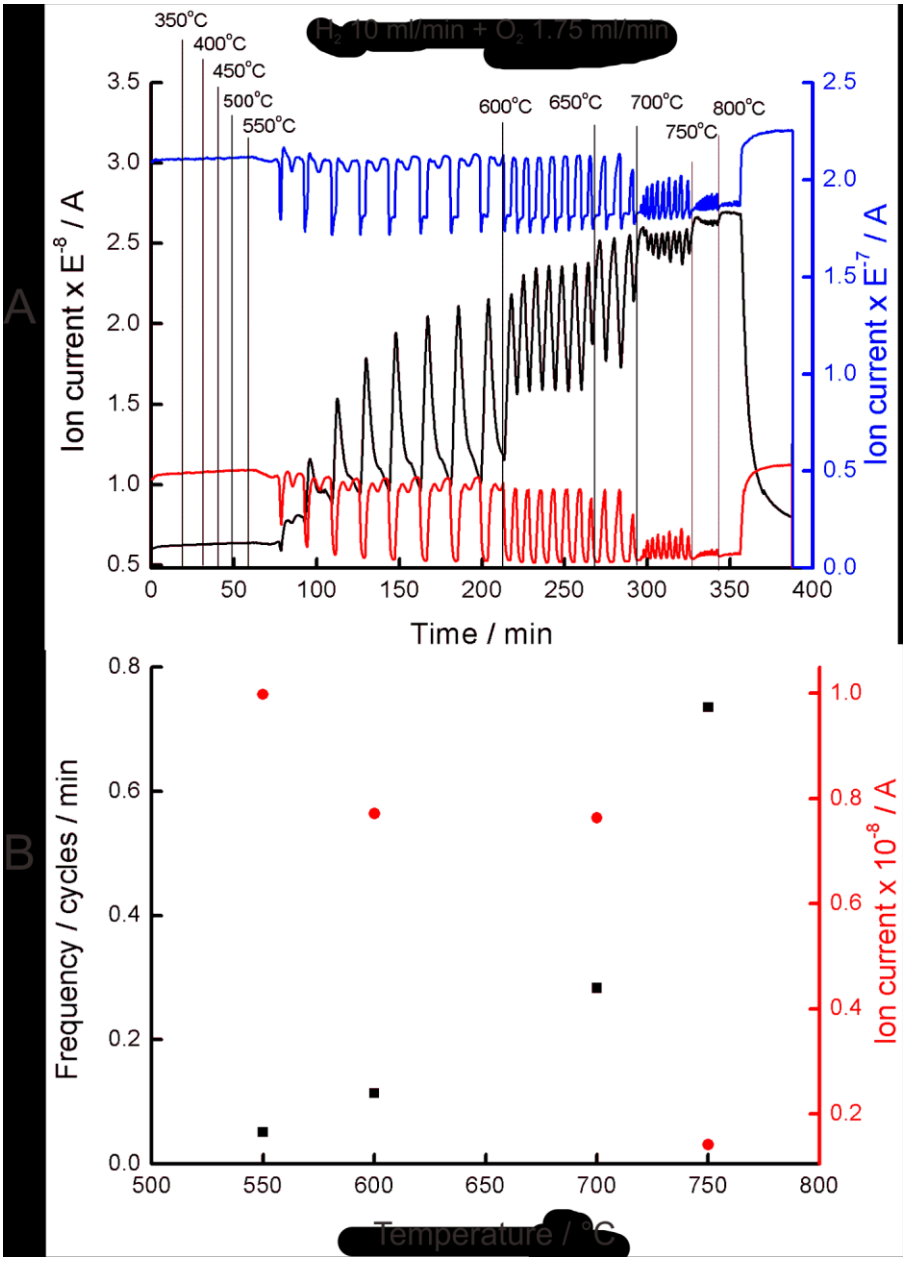

Figure 4.10 A) Oscillations of the H_2 (blue), H_2O (black) and O_2 (red) ion currents versus time over Ni foam at a fixed H_2/O_2 ratio of 10/1.75 (14.9% of O_2 in H_2) at different temperatures. B) Relationship between the frequencies of H_2O oscillation and temperature from 550 °C to 750 °C.

4.5 Discussion

4.5.1 Relationship between nickel oxidation state and catalytic activity

The complementary techniques of *in situ* SEM imaging and MS which were used in the current work demonstrate a correlation between the morphology of nickel catalysts, chemical state and catalytic activity. At 700 °C and a low O_2 content

(reaction mixture up to H_2:O_2 = 10:1) no oscillations were observed. The Ni surface exhibits only smooth metallic surfaces with minimum dynamics throughout the reaction as can be seen in Figure 4.2. When the O_2 feed was increased, oscillations are observed and the nickel catalyst exhibit dynamic behaviour. The high-active state of the Ni catalyst features a smooth and dark surface morphology, while the low-active state is characterized by rough and bright intensity with oxides covering the Ni surface. The temperature oscillates with the transformations of the surface states. As the external heating from the laser output current was kept constant, the oscillation arises from self-sustained hydrogen oxidation reactions. The oscillatory heating depends on the reaction rate and H_2O production rate. Therefore, temperature oscillations are an important indicator to unravel the active state of a catalyst.

4.5.2 On the H_2 oxidation mechanism over Ni catalysts

Gas phase and temperature oscillations have been observed during the hydrogen oxidation and light alkanes oxidation over Ni substrates.[27-30] Lobban and Luss proposed that the oscillatory behaviour could be caused by successive oxidation and reduction of the nickel surface. Their study was based on temperature oscillations. They concluded that the activity of the oxidized surface is lower than the reduced nickel surface. Thus, oxidation reduces the reaction rate and leads to a decrease of the temperature, while reduction increases the reaction rate which could be attributed to enhanced temperatures.[28] In addition, Kaichev et al. proved a similar oxidation-reduction mechanism in the propane oxidation reaction by using *in situ* XPS analysis which was conducted in a similar pressure range as the current study (~0.5 mbar).[27] Their study reveals that the oscillations originate from a reversible change of the Ni oxidation state of the surface of a Ni foil catalyst. They showed that during the low-active state the Ni surface was completely covered by a thick layer of NiO, which was fully reduced to metallic Ni in its high-active state.

The result from our *in situ* SEM experiments supports an oxidation-reduction mechanism for the H_2 oxidation reaction over Ni catalyst which is manifested by the occurrence of self-sustaining oscillation. During the reaction the high-active state of the surface is dark and smooth in contrast to the low-active state. This situation is independent of the gas phase. The dark and smooth surface could be attributed to

reduced surface species and the bright and rough surfaces should be ascribed to oxidized analogues. This can be explained by better electron conductivity of metallic nickel than nickel oxides, in which secondary electrons could be accumulated on the nickel oxide surfaces and contribute to the high brightness.

The exact driving force for the reversible oxidation-reduction of the Ni catalyst remains still unclear, but defects which form during this process, such as the formation of non-stoichiometric NiO_{1-x} could play a significant role. The oxidation of Ni and NiO and its backward reaction involve volume expansion and shrinking, respectively. Thus, defects can be easily formed during this process.[31] Besides, the growth of nickel oxides under partially reducing conditions (H_2 concentrations are 89%, 85.1% and 80%), a large number of defects can be expected during Ni oxidation. This defective NiO may have a minimum reduction barrier and, hence, a fast jump from low-active states to high-active states can be realized.

At elevated temperatures diminishing oscillation (lower amplitudes and higher frequencies) are observed as presented in Figure 4.10. These observations suggest that the Ni catalyst can be thermally pushed into the high-active state. This may lead to stable and smooth metallic surfaces throughout the reaction at elevated temperatures as adsorption and oxidation affinities change. According to the Ellingham diagram,[32] the NiO Gibbs free energy change (ΔG) has due to the positive entropic term a positive slop with increasing temperatures. This suggests that the probability to form NiO species at higher temperatures will be decreased for the given oxygen fugacity. Consequently, the formation of metallic nickel surfaces is enhanced when the temperature is increased from 550 °C to 800 °C. Therefore, metallic nickel surfaces can be stabilized at higher temperature which exhibit a high-activity during the hydrogen oxidation reaction.[33-34]

4.6 Conclusions

The current work provides visible surface morphological dynamics over nickel catalyst in the hydrogen oxidation reaction by applying *in situ* SEM. Simultaneously, gas phase oscillations are monitored by online mass spectrometry. The results show synchronized oscillations of nickel surfaces during hydrogen oxidation reaction and that this surface dynamics are closely related to the catalyst activities. During the high-active state the Ni catalyst exhibits dark and smooth surfaces which correspond

to the reduced state. As opposed the low-active state of Ni catalyst becomes bright and rough due to the growth of Ni oxide nanoparticles. The oscillation of the H_2 oxidation can be explained in terms of periodic oxidation and reduction of the bulk Ni catalyst. This study can provide useful information for further catalyst modelling and investigation. Furthermore our results show that a catalyst surface under reactions is as a dynamic unit which has to be considered in prospective modelling. In addition, the interaction between the gas phase and catalyst surface changes have to be taken into account. Finally, the temperature also changes with the observed self-sustained oscillations due to the released energy.

4.7 References

1. Imbihl, R.; Ertl, G., Oscillatory Kinetics in Heterogeneous Catalysis. *Chem Rev* **1995,** *95* (3), 697-733.

2. Othmer, H. G., Self-organization in Nonequilibrium Systems. *SIAM Review* **1982,** *24* (4), 483-485.

3. Zhdanov, V. P., Monte Carlo simulations of oscillations, chaos and pattern formation in heterogeneous catalytic reactions. *Surf Sci Rep* **2002,** *45* (7-8), 233-326.

4. Beusch, H.; Wicke, E.; Fieguth, P., Thermally and Kinetically Produced Instabilities in Reaction Behavior of Individual Catalyst Grains. *Chem-Ing-Tech* **1972,** *44* (7), 445-&.

5. Hugo, P., Stabilitiit und Zeitverhalten von DurchflubKreislauf-Reaktoren. *J Phys Chem B* **1970,** *74*, 121.

6. Imbihl, R., Nonlinear dynamics on catalytic surfaces. *Catal Today* **2005,** *105* (2), 206-222.

7. Chau, T. D.; de Bocarme, T. V.; Kruse, N., Kinetic instabilities in the NO/H-2 reaction on platinum. *Surface and Interface Analysis* **2004,** *36* (5-6), 528-532.

8. Imbihl, R., Nonlinear dynamics on catalytic surfaces: The contribution of surface science. *Surf Sci* **2009,** *603* (10-12), 1671-1679.

9. Flytzani-Stephanopoulos, M.; Schmidt, L. D.; Caretta, R., Steady-State and Transient Oscillations in Nh3 Oxidation on Pt. *J Catal* **1980,** *64* (2), 346-355.

10. Rajagopalan, K.; Luss, D., Influence of Inerts on Kinetic Oscillations during the Isothermal Oxidation of Hydrogen on Platinum Wires. *J Catal* **1980,** *61* (1), 289-290.

11. Ertl, G.; Norton, P. R.; Rustig, J., Kinetic Oscillations in the Platinum-Catalyzed Oxidation of Co. *Physical Review Letters* **1982,** *49* (2), 177-180.

12. Imbihl, R.; Cox, M. P.; Ertl, G., Kinetic Oscillations in the Catalytic Co Oxidation on Pt(100) - Theory. *J Chem Phys* **1985,** *83* (4), 1578-1587.

13. Cox, M. P.; Ertl, G.; Imbihl, R., Spatial Self-Organization of Surface-Structure during an Oscillating Catalytic Reaction. *Physical Review Letters* **1985,** *54* (15), 1725-1728.

14. Tsai, P. K.; Maple, M. B., Oscillatory oxidation of H2 over a Pt catalyst. *J Catal* **1986,** *101* (1), 142-152.

15. Vendelbo, S. B.; Elkjaer, C. F.; Falsig, H.; Puspitasari, I.; Dona, P.; Mele, L.; Morana, B.; Nelissen, B. J.; van Rijn, R.; Creemer, J. F.; Kooyman, P. J.; Helveg, S., Visualization of oscillatory behaviour of Pt nanoparticles catalysing CO oxidation. *Nat Mater* **2014,** *13* (9), 884-890.

16. Hendriksen, B. L. M.; Ackermann, M. D.; van Rijn, R.; Stoltz, D.; Popa, I.; Balmes, O.; Resta, A.; Wermeille, D.; Felici, R.; Ferrer, S.; Frenken, J. W. M., The role of steps in surface catalysis and reaction oscillations. *Nat Chem* **2010,** *2* (9), 730-734.

17. Ertl, G., Oscillatory Catalytic Reactions at Single-Crystal Surfaces. In *Advances in Catalysis*, Eley, D. D.; Pines, H.; Weisz, P. B., Eds. Academic Press: 1990; Vol. 37, pp 213-277.

18. Slinko, M. M., Oscillating reactions in heterogeneous catalysis: What new information can be obtained about reaction mechanisms? *Catal Today* **2010,** *154* (1), 38-45.

19. Gladky, A. Y.; Kaichev, V. V.; Ermolaev, V. K.; Bukhtiyarov, V. I.; Parmon, V. N., Propane oxidation on nickel in a self-oscillation mode. *Kinet Catal+* **2005,** *46* (2), 251-259.

20. Kaichev, V. V.; Gladky, A. Y.; Prosvirin, I. P.; Saraev, A. A.; Hävecker, M.; Knop-Gericke, A.; Schlögl, R.; Bukhtiyarov, V. I., In situ XPS study of self-sustained oscillations in catalytic oxidation of propane over nickel. *Surf Sci* **2013,** *609*, 113-118.

21. Kaichev, V. V.; Teschner, D.; Saraev, A. A.; Kosolobov, S. S.; Gladky, A. Y.; Prosvirin, I. P.; Rudina, N. A.; Ayupov, A. B.; Blume, R.; Hävecker, M.; Knop-Gericke, A.; Schlögl, R.; Latyshev, A. V.; Bukhtiyarov, V. I., Evolution of self-sustained kinetic oscillations in the catalytic oxidation of propane over a nickel foil. *J Catal* **2016,** *334*, 23-33.

22. Bychkov, V. Y.; Tyulenin, Y. P.; Slinko, M. M.; Korchak, V. N., Autonomous and forced oscillations during methane oxidation over cobalt catalysts. *Appl Catal a-Gen* **2007,** *321* (2), 180-189.

23. Howe, J. Y.; Allard, L. F.; Bigelow, W. C.; Demers, H.; Overbury, S. H., Understanding catalyst behavior during in situ heating through simultaneous secondary and transmitted electron imaging. *Nanoscale Res Lett* **2014,** *9*.

24. Bockris, J. O.; Dandapani, B.; Cocke, D.; Ghoroghchian, J., On the Splitting of Water. *Int J Hydrogen Energ* **1985,** *10* (3), 179-201.

25. Shanahan, C. E. A., Ellingham Diagram. *Chem Brit* **1983,** *19* (5), 387-387.

26. Zhang, Q. F.; Li, Y. K.; Chai, R. J.; Zhao, G. F.; Liu, Y.; Lu, Y., Low-temperature active, oscillation-free PdNi(alloy)/Ni-foam catalyst with enhanced heat transfer for coalbed methane deoxygenation via catalytic combustion. *Appl Catal B-Environ* **2016,** *187*, 238-248.

27. Kaichev, V. V.; Gladky, A. Y.; Prosvirin, I. P.; Saraev, A. A.; Havecker, M.; Knop-Gericke, A.; Schlogl, R.; Bukhtiyarov, V. I., In situ XPS study of self-sustained oscillations in catalytic oxidation of propane over nickel. *Surf Sci* **2013,** *609*, 113-118.

28. Kurtanjek, Z.; Sheintuch, M.; Luss, D., Reaction-Rate Oscillations during the Oxidation of Hydrogen on Nickel. *Ber Bunsen Phys Chem* **1980,** *84* (4), 374-377.

29. Lobban, L.; Luss, D., Spatial Temperature Oscillations during Hydrogen Oxidation on a Nickel Foil. *J Phys Chem-Us* **1989,** *93* (17), 6530-6533.

30. Kurtanjek, Z.; Sheintuch, M.; Luss, D., Surface-State and Kinetic Oscillations in the Oxidation of Hydrogen on Nickel. *J Catal* **1980,** *66* (1), 11-27.

31. Jeangros, Q.; Hansen, T. W.; Wagner, J. B.; Dunin-Borkowski, R. E.; Hebert, C.; Van Herle, J.; Hessler-Wyser, A., Oxidation mechanism of nickel particles studied in an environmental transmission electron microscope. *Acta Mater* **2014,** *67*, 362-372.

32. Transactions and Communications. *Journal of the Society of Chemical Industry* **1944,** *63* (5), 125-160.

33. Robino, C. V., Representation of mixed reactive gases on free energy (Ellingham-Richardson) diagrams. *Metall Mater Trans B* **1996,** *27* (1), 65-69.

34. Han, L. L.; Meng, Q. P.; Wang, D. L.; Zhu, Y. M.; Wang, J.; Du, X. W.; Stach, E. A.; Xin, H. L., Interrogation of bimetallic particle oxidation in three dimensions at the nanoscale. *Nat Commun* **2016,** *7*.

5 Summary and final conclusions

It has been proposed that many reactions under fixed conditions, exhibit dynamic behaviour. These dynamics are often attributed to dynamic changes in the catalyst surface chemistry. Here a direct visualization of changes to the surface shape, structure and chemical state have been observed using a modified environmental scanning electron microscope and characterized by *in situ* X-ray photoelectron spectroscopy and near edge X-ray adsorption fine structure. Real time observation of morphological redox dynamics of copper, platinum and nickel in mixture of reductant and oxidant–Hydrogen and oxygen–were used as a prototype to study the surface dynamics for further understanding of fundamental concepts in heterogeneous catalysis. The interaction between hydrogen and oxygen and the solid surface result in changes in surface reconstruction and oxide formation with time. Correspondingly, dynamic changes in surface chemistry dynamically alter the interaction between the surface and reactants, which is reflected by the change of adsorption rate and reactivity of reactants. These reactivity changes were detected by quadrupole mass spectrometer (QMS). Surface sensitive characterization methods, such as *in situ* XPS and NEXAFS, were utilized to identify the chemical composition of the phases present under the relevant conditions.

Copper surfaces exhibited periodic phase transitions between copper of various surface terminations and copper oxide in hydrogen rich conditions (4% oxygen in mixture of hydrogen and oxygen) at 700 °C. Three different morphologies, a faceted surface, a smooth oxygen terminated surface and Cu_2O islands co-exist on the surface and transform interchangeably and reversibly with time.

Platinum exhibited a flat surface, without surface reconstruction on the micron scale, in pure hydrogen or oxygen at high temperatures. However, the structure reconstructed immediately and showed dynamic behaviour in a mixture of hydrogen and oxygen with the formation various kinds of three dimensional structures. The surface converted from a flat surface to a rough surface as hydrogen-to-oxygen ratio decreased from 2:1 to 0:1. The surface morphological change rate reached its maximum at hydrogen-to-oxygen ratio of 1:1 at 800 °C, and was correlated with a maximum in catalytic conversion rate. Surface morphological change rate was, in

general, found to correlate positively with catalytic conversion rate, demonstrating a link between morphological dynamics and catalytic activity.

The nickel surface exhibited synchronized oscillations between a metallic and oxide state. The oscillations could be controlled by temperature and gas concentration. The surface brightness was used as an indicator of the surface structure, and has been observed to oscillate between bright particles and a relative flat dark surface in oxygen-lean conditions (1.25 ml/min O_2, at constant 10 ml/min H_2). The bright particles converted to bright triangular shapes and oscillated with a dark flat surface as oxygen increased to 1.75 ml/min. The dark surface is attribute to the metallic state of the surface, while the bright particles were attributed to nickel oxides, due to the secondary electron charging effect. The brightness intensity varied with time, and the reactant consumption rate, product production rate and temperature exhibited a corresponding oscillation shape. Hydrogen and oxygen concentration exhibited anti-phase oscillation with surface brightness intensity, while temperature and product production rate exhibited in-phase oscillations.

In conclusion, ESEM investigations of adsorbates interacting with metal surfaces have demonstrated several new perspectives on the role of surface dynamics in reactive atmospheres. New insights related to surface dynamics has been obtained from a model system (hydrogen and oxygen) interacting with copper, platinum and nickel, which are extensively used as catalysts in industry. From the direct visualization of surface dynamics, it can be concluded that for reactive adsorbates interacting with metal surfaces, the traditional static surface structural model of catalytic surfaces must in some cases incorporate a dynamic restructuring to account for all catalytic processes occurring under the given reactive conditions. In particular, surface atoms change their original equilibrium position in response to the changing chemical environment, imposed by interactions between the multiple gas phase components and the catalyst surface. The adsorbates act as a dynamic medium, where the competing actions of reductant and oxidant on altering the catalyst's surface chemistry act as a feedback mechanism, resulting in the coexistence of multiple surface phases. As each phase exhibits its own bonding properties with the gas phase reactants, the catalytic activity can be greatly influenced by the ensemble of surface phases. Finally, it has shown that environmental scanning electron microscope is a valuable *in situ* method for studying

catalyst surface dynamics in real conditions, yet further developments in space and time resolution, as well as chemical state identification, will greatly enhance the insights available of such methods in the future.

6 List of figures

7 List of tables

8 List of supporting figures

9 List of supporting tables

10 List of equations

11 List of abbreviations

AFM	Atomic force microscopy
BSE	Backscattered electrons
EBSD	Electron backscattering diffraction
EDS/EDX	Energy dispersive X-ray spectroscopy
EELS	Electron energy-loss spectroscopy
ESEM	Environmental scanning electron microscopy
ETEM	Environmental transmission electron microscopy
fcc	Face centred cubic
FEG	Field Emission Gun
FFT	Fast Fourier transform
FIB	Focus ion beam
GSED	Gaseous secondary electron detector
HAADF	High angle annular dark-field
HREELS	High resolution transmission electron microscopy
HZB	Helmholz-Zentrum Berlin
LEED	Scanning low-energy electron diffraction
LFD	Large-Field-Detector
L-H	Langmuir-Hinshelwood
MS	Mass spectrometer
NAP-XPS	Near-ambient pressure X-ray photoemission spectroscopy
NEXAFS	Near-ambient X-ray absorption fine structure
PEEM	Photoemission electron microscope

PLA	Pressure-limiting apertures
QMS	Quadrupole mass spectrometer
ROI	Region of interest
SE	Secondary electrons
ESPEM	Environmental scanning photoemission microscopy
STEM	Scanning transmission microscopy
STM	Scanning transmission microscopy
SXRD	Surface X-ray diffraction
UHV	Ultra-high vacuum
UV	Ultraviolet
XPS	X-ray photoelectron Spectron
XRD	X-ray diffraction